ELECTRONIC PROPERTIES OF ANATASE TiO_2 AND IRON (III) DOPED TiO_2 NANOPARTICLES

TUOCHEN GONG

A THESIS SUBMITTED TO THE FACULTY OF GRADUATE STUDIES IN PARTIAL FULFILLMENT OF THE REQUIREMENTS FOR THE DEGREE OF MASTER OF SCIENCE

GRADUATE PROGRAM IN PHYSICS AND ASTRONOMY

YORK UNIVERSITY

TORONTO, ONTARIO

DECEMBER 2021

Abstract

Since its discovery by Fujishima and Honda in 1972, titanium dioxide (TiO_2) has been studied extensively due to its ability to split water and decompose dyes as a photocatalyst.

Among all phases, TiO_2 in the anatase phase displayed the highest photocatalytic rates for dye decompositions. Iron is selected as a dopant to maximize the efficiency under solar light.

In this study, we use structural, morphological, chemical methods to study nanoparticles prepared using the sol-gel method, to confirm their phases, crystallite sizes, appearance, and detailed chemical compositions. To understand the effect of iron doping on photocatalysis, band gaps and valence band structures are obtained using state-of-the -art spectroscopy techniques. Models of electronic band structures of anatase TiO_2 with various iron doping percentages are proposed, and effects of iron dopants on photodegradation are discussed using experimental results. Our study will benefit water purification industries, especially for on-site water treatments.

Acknowledgement

First of all, I would express my deepest gratitude to my supervisor, Professor Sylvie Morin, for her guidance, encouragements, and supports from all aspect. Thank you for offering me the great opportunity to do research with you, and I really enjoyed working with all the group members. You provided me more than academic research, and the professional critical thinking skill you illustrated to me will be beneficial for my future career.

I would also thank Professor Ozzy Mermut and Professor René Fournier for being my supervisory committee, as well as Professor Tao (Toby) Zeng and Professor Christopher Caputo for being the internal and external examiners. Your suggestions and supports guided me to think comprehensively on our project, and your insight into details improved the outcome of our study in ways that I haven't thought of.

Due to the special occasion of COVID-19, our lab hours were quite limited. This makes the time I spent with the Morin group even more precious. I would never forget those wonderful days with my friends and colleagues, Ghazal Sayad-Haghighi, Sreena Thekoot, Bibisomaia Rezaee, Dr. Mehry Fattah, Anirudh Krishnadas, Tongye Wang, Dr. Sven Kochmann, Dr. Stanislav Beloborodov, Zejie Lv, and Bohan Li during my study. I really appreciate all your help and suggestions within and beyond my academic life. Also, even though we haven't met, I want to appreciate Dr. Mohammad Nazari and Dr. Maryam Hariri for their previous works related to this project.

This work could not be accomplished without the help of X-ray diffraction results by Maureen Fitzpatrick and Victoria M. Jarvis at McMaster University, scanning electron microscopy and energy dispersive x-ray analysis by Dr. Magdalena Jaklewicz at York University, ultraviolet-visible diffuse reflectance spectroscopy by Brian Malile and Dr. Jennifer Chen at York University, as well as X-ray and ultraviolet photoelectron microscopy by Dr. Joseph P. Thomas and Dr. Tony Leung. Thanks to all of you for your professional assistances and kindnesses to my study.

I would also like to thank all the staff members of the Department of Physics and Astronomy at York University, especially Cristalina Carmela Del Biondo, Dr. Tom

Kirchner, Dr. Matthew Johnson, Dr. Matthew C. George, and Dr. Patrick Hall for all your kindness and help with the issue I encountered, particularly my course arrangements and teaching assistantships. My academic life could not be this smooth without your efforts.

In the end, it's been more than two years since I left home for my master study. I cherish the love from my considerate fiancé and my supportive families. Thank you all for encouraging me throughout my study, and I feel lucky and blessed to have you all in my life.

Table of contents

List of tables

List of figures

List of symbols and abbreviations

1. **β**: Full width at half-maximum (XRD)
2. **θ**: Bragg angle (XRD)
3. **K**: Shape factor (XRD)
4. **λ**: Wavelength
5. **ν**: Frequency
6. **σ**: Standard deviation
7. **ϕ**: Work function
8. $\mathbf{E_F}$: Fermi level
9. $\mathbf{E_g}$: Band gap energy
10. $\mathbf{E_{SE}}$: Secondary electron edge cut-off energy
11. **h**: Planck constant
12. **R**: Reflectance
13. **%R**: Percentage reflectance
14. **At. %**: Atomic percent
15. **Wt. %**: Weight percent
16. **CBM**: Conduction Band Minimum
17. **DI H_2O**: Deionized Water
18. **EDX:** Energy Dispersive X-ray analysis
19. **EtOH:** Ethanol
20. **TTIP:** Titanium Isopropoxide
21. **SEM:** Scanning Electron Microscopy
22. **UPS:** Ultraviolet Photoemission Spectroscopy
23. **UV:** Ultraviolet
24. **UV-Vis DRS:** Ultraviolet-Visible Diffuse Reflectance Spectroscopy
25. **VBM:** Valence Band Maximum
26. **XPS:** X-ray Photoemission Spectroscopy
27. **XRD:** X-Ray Diffraction

1 Introduction

Titanium dioxide (TiO_2), or titania, is a widely used commercial product in our daily lives. Products such as paints[1], toothpastes[2], pigments[3] and sunscreens[4,5] have TiO_2 as part of their ingredients. In sunscreens, TiO_2 helps prevent solar light from damaging our skin, especially from the UV region of the solar emission spectrum, by absorbing the corresponding wavelengths. It also has been applied in the energy field, such as in dye-sensitized solar cells[6].

TiO_2 was the subject of many studies since the discovery of nanostructured TiO_2 photocatalytic properties by Fujishima and Honda[7] in 1972. Nanostructured TiO_2 produces hydrogen via water splitting[8,9], and it also decomposes dyes in aqueous solutions when illuminated with sun or UV light[10–13]. With these valuable abilities, TiO_2 is a promising material for the energy industry, and it can resolve many pollution problems in modern societies.

TiO_2 can adopt different structures that give rise to anatase, brookite and rutile phases. Both anatase and brookite phases are metastable, which can be transformed into rutile by heating to high temperatures. However, the anatase phase has been determined to have the highest photocatalytic rate due to its indirect band gap[10,14], which is ideal for the photodecomposition process. Photodegradation using anatase TiO_2 is eco-friendly and can be applied widely for water purification purposes. However, the material's performance suffers from its absorption wavelength using solar irradiation. The band gap is about 3.2 eV[15–17] for the anatase phase, which lies in the UV region of the solar spectrum. An estimation of the power distribution from the solar spectrum indicates that less than 10% of the total sun's energy comes from the UV region[18]. Thus, to maximize the solar energy usage, it is optimal to narrow the band gap of the anatase TiO_2 into the visible region.

In fact, there are several paths to narrow the band gap: doping with other elements[10–13,19–21], sensitization with dyes[5], etc. Doping will be our choice since it is easily achievable via the sol-gel synthesis of TiO_2 nanoparticles[22–24].

1.1 Crystal properties

The anatase and brookite phases of titanium dioxide are metastable[25–28]. In other words, under certain conditions, such as elevated temperature or high pressure, both anatase and brookite phases can be converted into the rutile phase. Anatase is likely to be formed under normal pressure at room temperatures, however, rutile is considered to be the most thermodynamically stable phase since it exhibit the lowest surface free energy[29]. Shown in Figure 1.1-1 is a phase diagram of TiO_2.

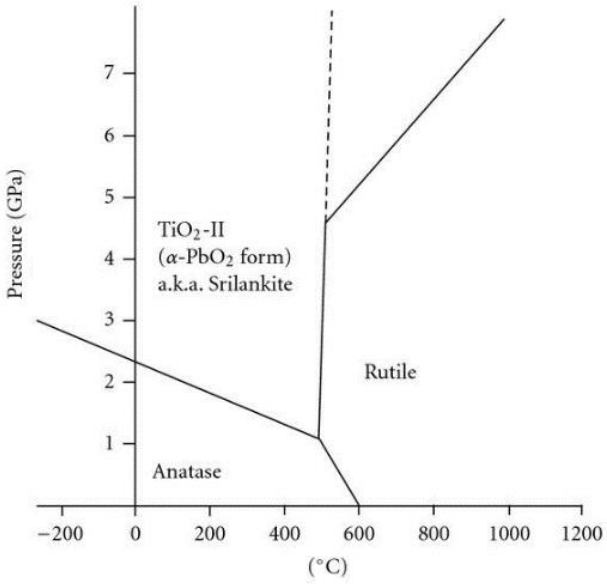

Figure 1.1-1 Composite phase diagram for TiO_2 [25–28]. Reprinted with permission from reference[28], Copyright © 2009 Xiliang Nie et al.

The anatase and rutile phases possess tetragonal unit cells, while brookite is orthorhombic. The crystal structure of each phase is shown in Figure 1.1-2, and their corresponding lattice parameters are summarized in Table 1.1-1.

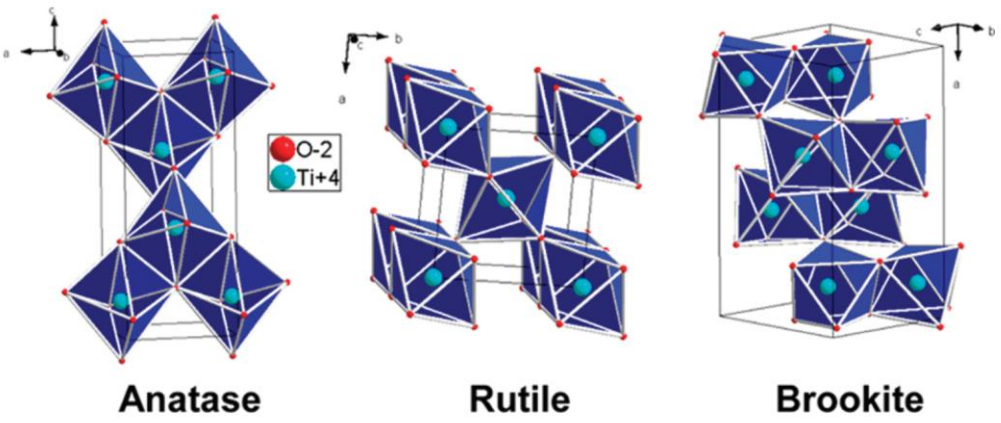

Figure 1.1-2 Representations of the TiO_2 anatase, rutile, and brookite forms. Reprinted with permission from reference [30], Copyright © 2010, American Chemical Society.

Table 1.1-1 Lattice parameters for anatase, rutile, and brookite TiO_2.

Phase	a(Å)	b(Å)	c(Å)	V(Å^3)	$\alpha = \beta = \gamma$(°)	Ref.
Anatase	3.784	3.784	9.515	136.242	90	[18]
Rutile	4.593	4.593	2.959	62.422	90	[18]
Brookite	9.166	5.436	5.135	255.858	90	[30]

1.2 Band structures

The electronic band structure depends on composition and the crystal structure. It can show the energy and symmetry of occupied and empty electronic states in a material. In a general picture, the band structure contains the valence band, conduction band, as well as the Fermi level. The term band gap vividly describes the forbidden regions where no electron states can exist between the valence and conduction bands from the band theory of solid-state physics.

Moreover, the valence band is the band region electrons can occupy, while the conduction band is the unoccupied band region in the electronic band structure. The highest occupied molecular orbital (HOMO) in the valence band is known as the valence band maximum, and the lowest unoccupied molecular orbital (LUMO) is the conduction band minimum. Energy difference between HOMO and LUMO defines the band gap energy of a material.

When a photon with energy no less than that of the band gap is absorbed, one electron gets excited and leaps across the forbidden gap towards the conduction band, leaving a hole (positron) in the valence band. This process has two variants based on the type of the band gap: direct or indirect. For a direct band gap, the HOMO and LUMO have the same crystal momentum, such that electrons can be directly excited from the valence band maximum to the conduction band minimum without changing its momentum. However, for the indirect band gap, the electron must additionally transfer (or absorb) momentum to (or from) the crystal lattice after the excitation to reach the conduction band.

Another feature from the band diagram is the Fermi level. It is a hypothetical energy level used to determine the electronic type of a material, i.e., metal, semi-metal, semiconductor, and insulator. As shown in Figure1.2-1, for metal and semi-metal, the Fermi level is located within at least one of the bands, while it would be within the band gap for semiconductors and insulator[31].

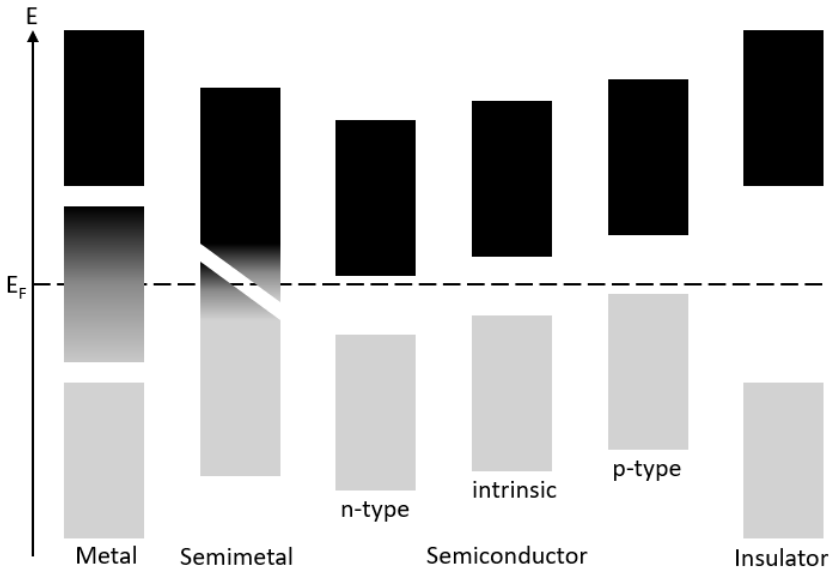

Figure 1.2-1 Positions of the Fermi level in the band structure of materials.

Adapted from Figure 1, Chapter 7 in reference [31].

Previous experimental studies have measured the band gap energies for the three phases

of TiO_2 [15–18,32,33], and the direct and the indirect band gaps for each phase are shown in Table 1.2-1.

Table 1.2-1. Direct and Indirect band gap values for anatase, rutile and brookite TiO_2.

Phase	Direct band gap	Ref.	Indirect band gap	Ref.
Anatase	3.5 eV	[18]	3.2 eV	[15,16]
Rutile	3.7 eV	[18]	3.0 eV	[15,17,33]
Brookite	3.5 eV	[18,32]	3.1 eV	[15,16]

By analyzing the mechanism of electron excitation from the band theory, it is not hard to conclude that materials with lower band gap values should have a higher rate of excitation when using the same light source. However, the study by Luttrell *et al.*[10] shows that even though the TiO_2 rutile phase has a lower band gap value, the anatase has a stronger photocatalytic property due to the longer lifetime of the photogenerated electrons and holes originating from the indirect band gap photoexcitation. This coincides with a theoretical study by Zhang *et al.*[14], which showed that both rutile and brookite phases have direct band gaps, while anatase is showing an indirect band gap. As for the brookite phase, it is not frequently used as a photocatalyst due to the challenge in its synthesis[16].

1.3 Sol-gel method: TiO_2 nanomaterial

Sol-gel method is widely used to produce ceramic materials with high yields[34,35]. It has been applied in the preparation of coatings[36], as well as the production of nanomaterials[37], thin films and fibers[38].

In a sol-gel process, the precursor, usually an inorganic metal salt or a metal alkoxide, undergoes hydrolysis and polymerization, resulting in the formation of a colloidal suspension, known as the ‘sol’. Particles form during this time, and they become larger due to nucleation, growth and aggregation processes[39]. Thus, the size of the particles obtained using sol-gel method is depending on the rate of formation of the ‘sol’.

Later, upon the completion of polymerization, or solvent loss, the 'sol' becomes the 'gel' via gelation[40–42]. Usually, the simplest way to complete this stage is to give enough time for a full sedimentation. The formed 'gel' can be obtained after removing the excess of liquid. Filtration, following by drying, helps to speed up the process to yield the final product.

TiO_2 nanomaterials can be produced from the method described above. There are two main streams of TiO_2 sol-gel synthesis: alcohol-based and aqueous-based. In the alcohol-based method, Ti-O bonds from the precursors, typically $Ti(OC_2H_5)_4$, $Ti(OC_3H_7)_4$, and $Ti(OC_4H_9)_4$, grow into Ti-O-Ti chains by addition of insufficient amount of water. When those precursors are exposed to excess amount of water, formation of $Ti(OH)_4$ is favored instead[40–43]. Using experimental methods, Bessekhouad *et al.* found that the by using $Ti(OC_3H_7)_4$ as the precursor at 65 ºC, the molar ratio of water to the alkoxide group for the best photoactivity was 1:75 [40]. As for the aqueous-based process, the precursors, usually $TiOSO_4$[44] and $TiCl_4$[45], hydrolyze and precipitate once a basic solution is added. Other methods, such as vapor deposition[46], sonochemical[47], and hydrothermal[48,49], can also produce TiO_2 nanomaterials. Among all, the sol-gel method is one of the most favorable methods due to its high yield, short synthesis time, controllable product properties, and it is easy to perform.

1.4 Doping

Doping is a way to introduce impurities to a semiconductor, such that the electronic band structure can be modified by the dopant. Based on the choice of doping element, semiconductors can be divided into two types. For a *p*-type semiconductor, such as boron-doped silicon, the boron dopant acts as an acceptor, such that each dopant accepts an electron from silicon which creates a hole. In terms of the electronic band structure, a sub-band will be created near its valence band theoretically after the dopant is introduced to the crystal matrices. As for the *n*-type, such as phosphorus-doped silicon, the dopant will provide an extra electron to the system, resulting in a sub-band creation near its conduction band[31]. Thus, by doping, the gap between the valence band and the

conduction band becomes smaller. In this way, photons with larger wavelengths can be absorbed by modifying the band structure of a semiconductor through doping.

Based on previous studies, results have been reported on the effect of doping with various elements to modify the electronic structure of TiO_2. Liu *et al.*[19] used N as the dopant, and the direct bandgap was successfully decreased from the undoped 3.22 eV to 3.18 eV (N, 5.70 at. %), which lies within the visible region. The study by Wojtaszek *et at* showed that the nitrogen doping would create sub band is near the valence band[50], which is considered as the *p*-type doping. Meanwhile, Inturi *et al.*[21] doped TiO_2 with Ce, Co, Cu, Mn, Mo, Ni, V and Y, and all dopants successfully narrowed the bandgap into the visible region. Other dopants, such as Fe [10–13,19] and C[51,52], also showed the same effect of decreasing the band gap of TiO_2.

From previous studies, doping TiO_2 with Fe^{3+} would lead to band creation near the conduction band and valence band[53,54]. The majority would be the *n*-type doping by Fe^{3+}, however, it can transform into Fe^{2+} or Fe^{4+}, by losing or gaining an electron, such that additional sub bands can be created near the conduction or the valence band, respectively. This process would also help trap electrons for a longer time, resulting in an overall increase in the photodegradation rate of such material by increasing the time scale of the photoinduction process of TiO_2. Based on measurements performed using time-resolved absorption spectroscopy, charge carriers were generated in 10^{-15} seconds, and they were being trapped for 10^{-14} to 10^{-11} seconds before the recombination process[55].

In addition, iron is an abundant element in nature. Due to the potential of the doped titanium dioxide nanomaterial, the studied material can be applied in several ways, such as being used as photocatalysts in water purification industries. Thus, using iron as a dopant could minimize the cost of producing such materials. Also, iron is non-toxic, and it will be safe to apply the doped material directly to the environment without causing further contamination. Lastly, based on the property of Fe^{3+} ion, its radius of 0.64 Å is close to the radius of Ti^{4+} (0.68 Å)[11]. Hence, doping would minimally affect the TiO_2 crystal structure. With all benefits, Fe^{3+} is a promising candidate for TiO_2

crystal modifications to enhance its photocatalysis properties.

1.5 Mechanism: photodegradation of dyes

From the industrial perspective, photodegradation is viewed as a favorable method for on-site decomposition of organic compounds in water. It uses sunlight as a source of energy, and the process can be tailored for small scale operation. Without addition of any oxidants, titania can produce hydroxyl radicals when illuminated in water under UV light[11–13]. Hydroxyl radicals are known to be strong oxidants, and they are responsible for dye decomposition, resulting in full or partial mineralization of the dye into water and carbon dioxide, or dye intermediates[56,57].

Direct and indirect mechanisms can be used to explain the photodegradation of a dye. The indirect mechanism, as shown in Figure 1.5-1, is the dye decomposition process assisted by external semiconductor materials. When struck with photons of appropriate energy, the semiconductor property of TiO_2 allows electrons to jump towards the conduction band, leaving a hole in its valence band. These photon-generated holes will then interact with water molecules to form hydroxyl radicals. Simultaneously, electrons in the conduction band will combine with surface absorbed oxygen to create more hydroxyl radicals[58]. Thus, the photogenerated electrons and holes can produce OH radicals via the described process.

The rate of the OH radical generation is highly associated with the electron-hole recombination process. These photogenerated charge carriers would also recombine following the emission process of a semiconductor. The emission process decreases the number of available electrons and holes on the surface, such that less OH radicals can be generated from the indirect mechanism[18]. Thus, the recombination process should be suppressed to maximize the photodegradation efficiency.

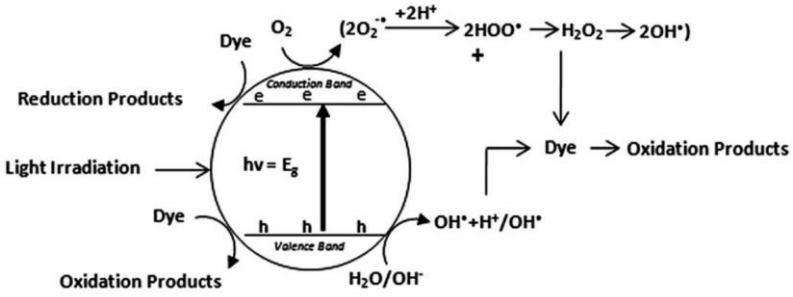

Figure 1.5-1. Schematic representation of indirect photocatalytic dye degradation. Republished with permission from reference [59], Copyright © 2014, RSC Publishing.

On the other hand, the dye is self-decomposing as well, which is known as the direct mechanism. Illustrated in Figure 1.5-2, the dye gets excited by absorbing photons, which wavelength is no less than the dye's band gap. A triplet state forms which offers the external semiconductor material one electron to its conduction band. In the same manner as the indirect mechanism, such electrons would react with surface absorbed oxygens to provide hydroxyl radicals. In comparison, studies have shown that the rate of self-decomposition is far less than the rate from the indirect mechanism[32,59,60].

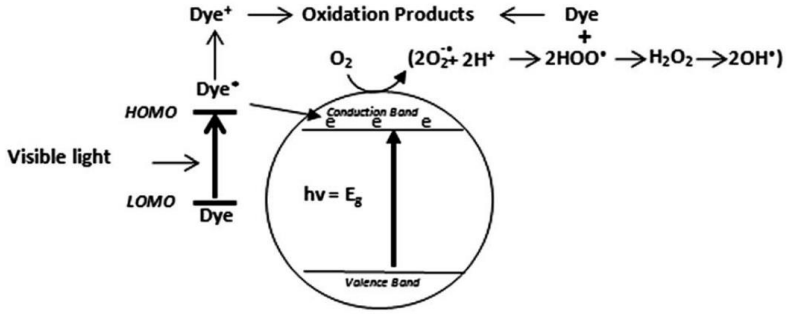

Figure 1.5-2. Schematic representation of direct photocatalytic dye degradation. Republished with permission from reference [59], Copyright © 2014, RSC Publishing.

1.6 Previous results

1.6.1 Synthesis of TiO_2 nanomaterial

As introduced, many synthesis methods could yield TiO_2 nanomaterials with desirable phase and doping compositions. A previous study by Zhang *et al* revealed the relation of TiO_2 particle sizes and the photodecomposition rate of chloroform. Via sol-gel method, TiO_2 nanoparticles were prepared using titanium isopropoxide (TTIP), anhydrous ethanol and deionized water, where iron doping was achieved by adding iron nitrate nonahydrate, followed by drying and calcinating at 450 °C to stabilize the phase. X-ray diffraction measurements of 0.02 to 1.0 at. % iron-doped and undoped samples all showed the anatase phase without significant crystallite size differences[61]. With the same routine, Mi and co-workers successfully synthesized Fe-doped anatase phase TiO_2 nanocrystals. By controlling the ratio of their precursor, TTIP to water, they concluded that higher water percentages would provide smaller crystallite sizes based on x-ray diffraction measurements. In addition, anatase TiO_2 crystallites present lower crystallinity as well as smaller sizes at higher synthesis temperatures from 250 °C to 450 °C [62]. Dr. Nazari, a PhD candidate in the Morin group, synthesized TiO_2 nanoparticles with iron doping level in range of 0 to 5.0 mol% under identical conditions. Results indicated the formation of minor brookite phase in some samples, and iron doping did not have an obvious effect on the estimated crystallite sizes from x-ray diffraction analysis[12].

Using titanium butoxide as the precursor, Baorang Li *et al* conducted studies of preparation conditions to the effect of crystallite sizes using sol-gel method. In their work, adjustments were made based on the ratio of titanium butoxide and deionized water, as well as the reaction pH and calcination temperatures. X-ray diffraction patterns of their synthesized samples indicated the transition from anatase to rutile phase from 600 to 800 °C[63]. Meanwhile, smaller crystallites were obtained with a shorter calcination time and a lower temperature. Concentration of precursors, as well as the pH during reaction, only played a minor role in the particle sizes of the anatase

phase[63].

In another study, Li and colleagues synthesized amorphous TiO_2 nanoparticles, which were then processed under hydrothermal reaction at 200 °C using an appropriate amount of iron nitrate nonahydrate to achieve doping. The x-ray diffraction results for samples containing 0 to 10 mol% iron doping showed an inversely proportional relation between the doping percentage and the crystallite sizes, estimated by the Scherrer equation (section 2.1, equation (1)). In addition, iron doped samples were much smaller and more uniform than the undoped sample according to their TEM analysis[49].

With another synthesis method, Mädler and their research group applied flame spray pyrolysis technique to produce pure and Fe-doped TiO_2 nanoparticles. The synthesized materials were prepared by mixing TTIP and Fe-naphthenate to achieve appropriate doping percentages. The mixture was then diluted with xylene and spray-ignited with methane and oxygen. Ultrafine particles were then collected from a glass filter and characterized using various methods. From x-ray diffraction measurement, the increase of iron doping not only decreased the crystallite sizes, it also increased the portion of rutile phase formed[53].

1.6.2 Photodegradation using Fe-TiO_2 nanomaterial

The photodecomposition of organic compounds is one of the key features scientists are interested in. The rate of catalyzed photodegradation allows to determine the overall efficiency of such photocatalyst. The photodegradation performance of doped TiO_2 nano powder can be analyzed based on its decomposition mechanism. It is the OH radical produced via illumination that decomposes organics. Thus, the role of doping can be deduced quantitatively after measuring the OH radical generation rate.

A study by Choi *et al* tested various doping elements, including iron, for their ability to decompose chloroform. The results showed for every element, there existed an optimal doping percentage to maximize the decomposition rate. More specifically, chloroform degradation quantum yields were calculated for all samples, and the corresponding values for undoped, 0.1 at. %, 0.5 at. %, 1.0 at. %, 2.0 at. %, and 5.0 at. % Fe samples were 0.08%, 0.78%, 1.19%, 0.80%, 0.51%, and 0.10%, respectively. Thus, the optimal

doping level for iron was determined to be 0.5 at. %[64]. A follow-up study from Zhang and co-workers suggested further that there would be an optimal iron doping percentage for particles of a particular size. In their study, experiments were carried using similar routines. Outcomes indicated that the optimal doping level of Fe^{3+} decreases from 0.2 at. % to 0.05 at. %, corresponding to an increased particle size from 6 nm to 11 nm for the anatase phase to achieve the best photodecomposition rate[61].

From a different approach, George *et al* conducted electron paramagnetic resonance measurements to directly quantify the OH radical generation rate of TiO_2 nanoparticles. Samples with various iron doping percentages were illuminated with UV-near visible source. A standard Fenton reaction system, where hydroxide radials and ions are produced from hydrogen peroxide solution using ferrous iron as a catalyst[65], was used to compare spectral features of TiO_2 generated OH radicals. The results showed an obvious trend of decreasing rate of OH radical production with increasing iron doping level, and such conclusion was the result of band gap shrinking due to doping. They also tested the size effect by reducing the crystallites of both undoped and 10 at. % Fe doped samples from 12 nm to 6 nm. Conclusions were made that size reduction effect was not the primary reason to affect the photodegradation rate based on the decomposition of N-acetyl-$_L$-tryptophanamide[53].

Methylene blue is a common pollutant in the textile, plastic, and dye industries[58], thus many researchers have extensively studied this problem. With UV irradiations, Li and colleagues observed the photodegradation of methylene blue solution using anatase TiO_2 nano-crystallites with various iron doping percentages. Results showed that the decomposition rate decreased with higher iron doping percentages, and the highest rate belonged to the undoped anatase phase[49]. Nazari used a solar light simulator as the illumination source for the decomposition process. At pH 4.5, starting with the concentration of methylene blue at 4.0 mg/L, the undoped sample reached a total decomposition within 180 minutes of light exposure. Less amount of methylene blue was decomposed with higher iron doping from the study. In stronger acidic environment at pH 2.4, even though none of the prepared samples fully decomposed the dye within

180 minutes, samples with 0.5 and 0.7 mol% Fe doping decomposed methylene blue faster during the first 90 minutes than the undoped sample, with 0.5 mol% being the fastest[12]. In the visible range, Liu *et al* repeated the photodegradation experiment using Fe, N, and Fe N co-doped nanoparticles. Based on the bandgap narrowing effect, the co-doped sample had the best performance, followed by Fe-doped, N-doped, and lastly the undoped[19].

Therefore, from previous experimental results, the dopants of TiO_2 nanoparticles had shown to affect the photodegradation process. Reasons behind could be complicated, however, the modification to the electronic band structure of TiO_2 can be carefully studied to see the role of the dopant during such process.

1.6.3 Electronic structure of Fe-TiO_2 nanomaterial

The band structure of a material can be obtained through 2 approaches: theoretical and experimental. From a theoretical study by Ramin Gul *et al*, the band structures of Fe-doped, N-doped, and Fe-N-coped anatase TiO_2 were simulated using conventional density functional theory. The simulation results clearly showed the shifting of the Fermi level and the sub-band creation due to the impurities, which lead to the TiO_2 band gap narrowing[66]. Liu and coworkers did another simulation on anatase TiO_2 with Fe and N as dopants, with a focus on electronic density of states near valence and conduction band. From the calculated density of state from 4 models, all Fe doped models presented a state creation slightly beyond the valence band maximum, which was associated with the Fe 3d orbital[19].

Only a few papers are dedicated to the experimental band structure measurements of Fe doped TiO_2 in the anatase phase. An instructive study by Maheu and colleagues used a combination of ultraviolet photoemission spectroscopy (UPS) and UV spectroscopies to measure the band structure difference between undoped anatase and rutile TiO_2. By the determination of the work function, the relative positions of the valence band and vacuum level were established, later the position of the conduction band was discovered by measuring the band gap[67]. Another study by Choudhary and group members revealed more details for the valence band structure of Fe-doped TiO_2 using valence

band spectroscopy. Features in the resulting spectra was determined via resonance photoemission spectroscopy. By doping with iron, a minor state located at around 2.4 eV was concluded to be the consequence of the Fe 3d state, and such feature was observed in all Fe-doped samples synthesized[68]. Other research groups, such as Feng[69] and Chen[70], conducted valence band x-ray photoemission spectroscopy (XPS) measurements to investigate the doping effect of dopants, such as boron and carbon. Therefore, electronic band structure measurements would be a powerful way to determine the modifications of the dopant. Based on the measured band structure, the effect of a dopant can be studied combining with the photodecomposition mechanism.

1.7 Thesis objective

The purpose of this study is to investigate how anatase phase TiO_2, a known photocatalyst, can be improved by iron doping to broaden its absorption from ultraviolet to visible region of the solar spectrum. After confirming the phase, size, morphology, and the iron doping level by powder x-ray diffraction (Powder XRD), scanning electron microscopy (SEM), energy dispersive x-ray analysis (EDX), and x-ray photoemission spectroscopy (XPS), the effect of the iron doping to the photocatalytic property of TiO_2 will be carefully studied. Through ultraviolet-visible diffuse reflectance spectroscopy (UV-Vis DRS), ultraviolet photoemission spectroscopy (UPS) and XPS, the electronic band structure will be obtained experimentally to investigate the modification due to iron doping. Besides, the influence of different sol-gel synthesis conditions, such as titanium isopropoxide (TTIP): deionized water (DI H_2O) ratio, calcination temperature and iron doping percentage, nanoparticle sizes can also be analyzed and discussed in a comparative way. The proposed research will improve the current understanding of such materials, particularly the modification due to various iron concentrations on the electronic band structure of anatase TiO_2 using experimental methods. Results can be also extended to other photodegradation processes which will benefit the water purification industry, especially for on-site water treatments.

2 Characterization methods

2.1 Crystal properties: Powder X-Ray Diffraction analysis

X-Ray Diffraction (XRD) analysis is a characterization method commonly used to study the crystal structure of materials. Results are spectra of the reflected angle 2θ against its intensity, and the phase composition of the sample can be determined using proper fitting methods and databases[71].

Due to the periodicity of the crystal structure, X-ray beam bombarding the crystal sample will be diffracted with respect to the incident angle. Due to the distance between identical crystal planes, parallel X-ray beams at an incident angle would travel slightly different distances. The angles of the incident beam, at which the diffracted beams are in constructive interference, can be expressed as Bragg's law[72]:

$$n\lambda = 2dsin\theta \quad (1)$$

where n is an integer of the diffraction order, λ is the wavelength of the incident X-ray, d is the distance between two identical planes, and θ is the Bragg's angle. The spacing d can be further determined using miller indices h, k, l obtained from the reciprocal lattice vector of the crystal.

It is worth to note that the detector collects the beam of the out-scattered angle, which is equal to two times the incident angle θ. In practice by identifying the 2θ positions of high intensities, the crystal information, such as phase compositions and crystal sizes, can be determined in detail.

To estimate crystallite sizes, the Scherrer equation is an appropriate model[73]:

$$D = \frac{K\lambda}{\beta cos\theta} \quad (2)$$

where D is the estimated average crystallite size, K is the shape factor with a typical value of 0.9, λ is the wavelength of the X-ray source, β is the full width at half-maximum (FWHM) of a peak, and θ is the Bragg angle for such peak. Based on the Scherrer equation, the crystallite size is affected by the frequency of the X-ray source, patterns of the obtained spectra, as well as crystal properties of the sample. The error related to the instrumentation could be minimized via standard samples, such as LaB_6[74]. Another technique, the Rietveld refinement, is a powerful tool to extract information from powder XRD patterns with peak overlapping. Using the least square approach, the refinement process starts by inputting an initial set of lattice parameters for each phase presented in the XRD pattern. Quantities such as phase compositions and lattice parameters would be more precise after each run, and the resulting average crystallite size estimations are much closer to the real ones[75].

2.2 Morphology: Scanning Electron Microscopy

Scanning Electron Microscopy (SEM) is a tool to observe the morphology of samples being measured. Unlike optical microscopy, SEM utilizes electron beams to generate high-resolution images with more details at high magnifications.

Electron beams are generated and travel towards the sample in the vacuum chamber of the apparatus. Detectors collect backscattered as well as secondary electrons to show the topological appearance of the specimen being measured[76]. More specifically, the backscattered electrons are electrons of higher energies that are 'repelled' by the atomic nuclei, while the less energetic secondary electrons are originated from high-energy electron-matter interaction[77]. Thus, materials must have enough electrical conductivity to obtain valid signals for image formation. To lower the noise level, the vacuum chamber ensures a minimum interaction between the electrons travelling to the detector and the environmental contaminations.

Compared with optical microscopes, the detection particles used for SEM have shorter wavelengths than photons in the visible range. The Rayleigh criterion can be used to illustrate the relation between the resolution and the light source:

$$\theta = \frac{1.22\lambda}{D} \tag{3}$$

where θ is the minimum resolvable angle in radians, D is the diameter of the aperture, and λ is the wavelength of the source[78]. In this case, higher frequencies can provide higher resolution using the same aperture. Typically, the resolution of SEM would be less than tens of nanometers, while the optical microscope is usually larger than hundreds of nanometers. Therefore, SEM would be an appropriate tool to learn the morphological properties of a material in the nanometer range.

2.3 Bulk elemental compositions: Energy Dispersive X-ray analysis

Energy Dispersive X-ray spectroscopy (EDX) can analyze elemental compositions of a sample. It is usually a built-in function in advanced SEM apparatuses.

With high enough energy, the incident electron beams can excite and eject the inner-shell electrons of an atom from their orbitals, resulting in partially filled orbitals. The outer-shell electrons have the tendency to fill the vacant inner orbitals positions at a lower energy level. Such process emits characteristic X-rays, with their frequency defined by the energy difference between these orbitals[79]. Like XRD, the characteristic X-ray signal is critical to identify the type and the abundance of each element presented using EDX. Moreover, the penetration depth of the incident electron is limited due to the electrical resistivity, EDX is a tool to analyze the elemental compositions several micrometers deep. The resulting spectra get more stabilized with respect to the acquisition duration, and the elemental composition of the sample can then be evaluated from the spectra using databases.

2.4 Surface elemental compositions and valence band structures: X-ray Photoemission Spectroscopy

X-ray Photoemission Spectroscopy (XPS), also known as Electron Spectroscopy for Chemical Analysis (ESCA), is a technique to determine surface elemental compositions, chemical states, as well as the overall electronic states. This characterization method is built on the photoelectric effect: the valence electron can be freed when such atom absorbs photons with appropriate energies.

In a measurement, photon beams of known wavelengths and fluxes are sent toward the material being measured. By collecting the freed photoelectrons, the kinetic energy and intensity could be measured by the detector. The final XPS spectrum shows the energy distribution of the collected electrons. The lines in the spectrum will be labelled depending on the energy levels from which they originate. During measurements, positive charges could accumulate on the surface of the sample if it is not properly grounded, or due to poor electrical conductivities of the material. This is caused by the creation of a hole when a surface electron is freed, resulting in sample charging. It can be solved by charge compensation, where electron beams are sent towards the charged surface for neutralization.

The result of the XPS spectra would be a count of electrons per second at various kinetic/binding energy. To convert from kinetic energy, which is directly measured, to the binding energy, one can follow:

$$E_{BE} = h\nu - E_{KE} \tag{4}$$

where $h\nu$ is the photon energy of the excitation X-ray source. The most used energy sources are aluminum $K\alpha$ (~1487 eV or 1486.6 eV) and magnesium $K\alpha$ (1254 eV or 1253.6 eV).

To make accurate assignments of spectral lines, the energy scale needs to be properly calibrated using known atomic standards. This can be done using carbon 1s peak (284.8

eV) which is due to hydrocarbon contamination and applies the same shift to all other peaks in the spectrum. It is also essential to consider the background noises when analyzing XPS spectra. There are 3 most common background types to choose from: linear, Shirley[80], and Tougaard[81]. Both Shirley and Tougaard background subtraction provide reasonable and comparable results, however, the background type must remain consistent throughout the analyses for a valid result.

The energy of the incident X-ray can penetrate through less than 100 nanometers from the surface, thus, the chemical composition from XPS analysis consists only the topmost of the sample. An ultra-high vacuumized chamber would help to remove environmental contamination, which benefits not only the sample cleanliness, but also the photo-freed electrons, resulting in accurate measurements. Sputtering is an effective way to obtain a clean surface; however, it may alter the measurement result if the sample is surface sensitive.

2.5 Band gaps: Ultraviolet-Visible Diffuse Reflectance Spectroscopy

UV-Vis Diffuse Reflectance Spectroscopy (UV-Vis DRS) is a powerful tool to measure the band gap value of a substance. Materials can absorb photons with energies higher than or equivalent to its band gap energy. In terms of wavelengths, this effect translates into light with longer wavelengths hitting the sample being reflected, while shorter ones are being absorbed. This phenomenon is used to determine the band gap of a material, known as UV-Vis DRS.

In a typical UV-Vis DRS spectrum, the percentage reflectance is recorded with respect to the source wavelength, where those wavelengths can vary in the ultraviolet and visible range. By viewing the resulting spectrum, the position at which a sudden drop of the percentage reflectance indicates the bandgap wavelength.

The famous Kubelka-Munk theory can be used to estimate the band gap values of materials from diffuse reflectance spectra mathematically. Originally, this theory was used to explain light propagations in parallel colorant layers[82,83]. Using UV-Vis DRS, the theory can be stated as:

$$F(R) = \frac{(1-R)^2}{2R} \tag{5}$$

where R is the reflectance of the sample, which can be converted from the measured percentage of reflectance (%R), and $F(R)$ is the Kubelka-Munk function[84]. The band gap can be extrapolated using the following relation:

$$\alpha h\nu = \frac{F(R)h\nu}{t} = A\left(h\nu - E_g\right)^n \tag{6}$$

where α is the linear absorption coefficient, $h\nu$ is the photon energy, t is the layer thickness, A is an energy-dependent constant, and E_g is the band gap energy. The coefficient n is a constant depending on the band type, which equals 2 or 0.5 for a direct or an indirect band type. By plotting $(\frac{F(R)h\nu}{t})^n$ with respect to photon energy, the band gap of different types can be calculated after a linear fitting of the resulting Tauc plot[85].

2.6 Valence band structures: Ultraviolet Photoelectron Spectroscopy

Ultraviolet Photoelectron Spectroscopy (UPS) is a surface-sensitive technique similar to XPS. Based on the photoelectric effect as well, it uses ultraviolet photon beams instead to obtain spectra from the valence band region of a material with more details. Ultraviolet photons contain smaller energy than X-ray, such that the penetration depth of this technique is only of few nanometers. Information about the valence band structure, position of the valence band maximum, as well as the work function of a sample are available using this measurement.

Like XPS, the spectra of UPS are the count of electrons per second against the photoelectrons' kinetic/binding energy. The energy range is in the valence band region, in other words, more details can be revealed compared with XPS in such region. In addition, a study by comparing the theoretical density of states and the experimentally measured spectra showed that UPS spectrum matched better in the valence band

region[86].

The shape of a UPS spectrum indicates the density of electrons in the valence band region. Without applying any bias voltage, the Fermi edge of such material, which is usually close to 0 eV at 0 K, is located at the highest energy which has no excited photoelectrons on the lower binding energy end. By fitting a linear model to the sharp shoulder in the lower range of the spectrum, the intercept on the energy axis estimates the valence band maximum position.

If bias voltage is applied, or the sample itself is charging, a charging peak, known as the secondary electron edge, would rise in the higher binding energy range on the valence band spectrum. Secondary electron edge cut-off is the binding energy where the count of electrons has the most sudden drop, and it can be used to calculate the work function of the material:

$$\phi = h\nu - (E_{SE} - E_F) \tag{7}$$

where ϕ is the work function, $h\nu$ is the energy of the excitation source, E_{SE} is the cut-off binding energy of the secondary electron edge, and E_F is the Fermi edge. The work function of the material is the minimum energy required to remove an electron from that material to vacuum and the removed electron has 0 J of kinetic energy. By determining the work function, it would allow us to visualize the relative position of the Fermi edge with respect to the vacuum level.

However, when the photon energy $h\nu$ exceeds the electron work function, the excess of energy transfers to the electron and becomes kinetic energy. The relation is given in the following equation:

$$E_{kinetic} = h\nu - \phi \tag{8}$$

3 Methodology

In this study, TiO_2 nanoparticles were synthesized in the Morin group at York University using sol-gel method. Through various preparation conditions, nanoparticles of desired iron doping percentages were expected to possess different particles and crystallite sizes in the anatase phase. Samples were then characterized at several research institutes to study their physical and chemical properties, such as phases, crystallite sizes, particle sizes, elemental compositions, band gaps, and valence band structures.

3.1 Sample preparation: nanoparticles

The sol-gel method used in this study was adapted from Dr. Nazari's work[12], with improvements to yield consistent products of smaller particle sizes.

Typically, the experiment started by cleaning the reaction containers and equipment in acid for 24 hours. A minimum would include: one 500 ml 3-neck round bottom flask (RBF), one pressure-equalizing dropping funnel (dropping funnel), one set of crucibles, one set of mortar and pestle, one 200 ml glass beaker with cover, and a Büchner funnel. All apparatuses were rinsed with tap, distilled, and deionized water (DI H_2O) in sequence after the acid wash.

Since titanium isopropoxide (TTIP, Reagent grade, 97%, Aldrich) is an extremely humid-sensitive chemical, an improvement was made by attaching argon purging to the system, as illustrated in Figure 3.1-1.

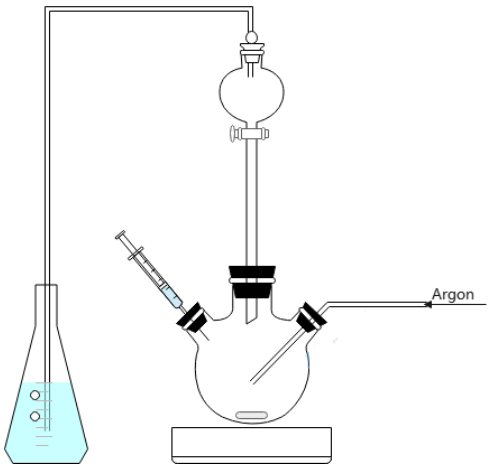

Figure 3.1-1. Apparatus and illustrations of sol-gel synthesis equipment and argon purging system.

To prepare for the synthesis, all glassware was connected and purged for 20 minutes to minimize the humidity in the reaction system before use. Afterwards, 12.4 ml TTIP and 56 ml ethanol (EtOH, Commercial Alcohols Inc., USP) were added to the top dropping funnel using clean syringes. The bottom RBF were filled with 69 ml deionized water (DI H_2O, MilliQ) and 69 ml EtOH, together with a magnetic stir bar with suitable sizes. To achieve the desirable theoretical doping level of Fe, iron (III) nitrate nonahydrate ($Fe(NO_3)_3 \cdot 9H_2O$, Reagent grade, 97%, Aldrich) were added to the RBF according to the following Table 3.1-1.

Table 3.1-1. The amount of $Fe(NO_3)_3$ added for iron doping in sol-gel synthesis.

Theoretical iron doping percentage (mol%)	0.5	1.5	5
Weight of iron (III) nitrate nonahydrate (g)	0.0817	0.2460	0.8174

Later, a clean syringe was used to extract a few milliliters of the well-mixed TTIP and EtOH solution from the dropping funnel. The system remained purging during the preparation stage, to suppress the undesirable reaction in the top dropping funnel due to air humidity.

The actual sol-gel process began after inserting the syringe with the extracted solution

to the side neck of the RBF. It was important to stir the solution in the RBF vigorously, otherwise large chunks of TiO_2 were likely to form on the surface of the RBF solution. To initiate the reaction, the solution from the syringe was injected slowly towards the center of the swirl, at a rate of about 1 drop per 2 seconds, until finished. The syringe was then pulled out, followed by opening the valve of the dropping funnel to achieve a rate of 1 drop per 2 seconds. By completion of the dropping process, a white cloudy solution, or yellow to brown depending on the Fe doping percentage, was obtained as an intermediate product. After removing other equipment, the RBF was sealed and kept stirring for another 24 hours for full condensation.

The following day, a vacuum pump was used for the filtration process. The condensed solution was poured towards filter papers (P5, Fisherbrand) in the Büchner funnel, while pumping. Rinsing with generous amount of EtOH and changing the filter paper frequently would help speed up this process. The obtained gel was cream-like, with colors from white to salmon for higher Fe doping levels.

The gel was then transferred to a clean glass beaker and dried at 110 °C in a furnace for 24 hours with a glass cover. To obtain a final product of separate nanoparticles, dried TiO_2 chunks were gently grinded using mortar and pestle until it became fine powders. Calcination in a furnace at 450 °C for 2 hours ensured the final powder was in the anatase phase.

By repeating the described procedure, TiO_2 nanoparticles listed in Table 3.1-2 were synthesized and kept in separate vials.

Table 3.1-2. Sol-gel synthesis preparation conditions.

Label	Theoretical Fe doping level (mol%)	DI H_2O: EtOH (ml: ml)	Calcination temperature (°C)
T5	0	69:69	450
T6	0.5	69:69	450
T7	0	138:138	450
T8	0.5	138:138	450
T9	0	138:138	350
T10	0.5	138:138	350
T11	5	138:138	450
T12	1.5	138:138	450

3.2 Sample preparation: thin film

For UV-Vis DRS, UPS and XPS *ex-situ* measurements, thin film samples were preferred for precise and reproducible results. Thus, TiO_2 thin layers of different thicknesses were deposited on cleaned low-resistivity Arsenic doped Silicon <111> wafer for different measurement purposes.

3.2.1 Wafer cleaning: RCA method

Radio Corporation of America (RCA) method[87] is an industrial procedure to clean silicon wafer, aiming to remove ionic and organic contaminants from the surface.

For preparation, 3 Pyrex bath containers, labeled as RCA1, RCA2, and water tank, were washed with acid and rinsed thoroughly with tap, distilled and deionized water. In RCA1, 140 ml of DI H_2O (MilliQ) and 22.75 ml of NH_4OH (Reagent grade, 30 %, Sigma-Aldrich) were mixed and heated up to 85 °C. Then, silicon wafers were transferred into the hot solution using a wafer tweezer, together with 22.75 ml of H_2O_2 (Electronic grade, 30%, Sigma-Aldrich). After 10 minutes, wafers were transferred from the hot solution to the DI H_2O water tank with a fluorocarbon tweezer. Meanwhile, 140 ml DI H_2O and 22.75 ml of HCl acid (Electronic grade, 30%, Sigma-Aldrich) were

added to RCA2 and heated up to 85 °C. After 5 minutes of dipping in the water tank, wafers were rinsed and moved to RCA2 container, followed by the addition of 22.75 ml of H_2O_2 for another 15 minutes' treatment at 85 °C. Finally, wafers were again dipped in the water tank with fresh DI H_2O for another 5 minutes, and the final products were dried using argon gas.

This procedure changed surface properties of silicon wafers from hydrophobic to hydrophilic, by creating a thin oxidized layer, which is favorable for the thin film deposition using a water-based slurry. If the oxidized layer is undesirable, removal can be achieved by a treatment using diluted HF for 1 minute before RCA2. Cleaned wafers were kept dry until further uses.

3.2.2 Thin film deposition: Doctor Blade method

Doctor Blade method is regarded as an efficient way to deposit a thin and uniform film on top of a substrate.

To make TiO_2 thin films on top of the cleaned silicon wafer, scotch tapes of various number of layers were applied to achieve desirable film thicknesses for different measurement purposes. Empirically, 1 layer, 2 layers and 4 layers of tape(s) would provide valid spectra for UPS, XPS and UV-Vis DRS measurements, respectively. The thickness for each scotch tape layer was 48 ± 5 micron after measurements. After cutting wafers into smaller pieces, scotch tapes were applied on two parallel edges of the substrate, layer by layer, without any air bubbles in between. The substrate region between two tape stripes remained clean and dry after applying the tape.

To make the slurry, modified from Dr. Hariri's previous work[88], 0.2 g of TiO_2 powder were well mixed and sonicated with 0.7 ml of DI H_2O. Then, 0.06 ml of acetylacetone ($CH_3COCH_2COCH_3$, ≥99%, Reagent grade, Sigma-Aldrich) was added gradually before grinding the mixture with mortar and pestle to form the slurry. To deposit the film on the substrate, a few drops of the slurry were applied to the substrate, followed by spreading the slurry using a glass Pasteur pipet with a quick slide. A thin and uniform film was obtained after drying, and the tape was removed. Using the same procedure, thin films of different compositions and thicknesses were fabricated, followed by a

calcination process at 450 °C in a furnace for an hour. Final products were collected and kept separately in clean vials with their measurement purposes labeled on top.

3.3 Characterization

Characterization techniques using Powder-XRD, SEM, EDX, UV-Vis DRS, XPS, and UPS, are introduced this chapter to characterize the properties of crystals, morphology, elemental compositions, and electronic band structures of the synthesized samples.

3.3.1 Crystal properties: Powder X-Ray Diffraction analysis

XRD patterns were collected using a Bruker D9 Discover Vantec500 Co 2D Powder at McMaster Analytical X-Ray Diffraction Facility at McMaster University, to learn phase compositions and to obtain average crystallite sizes after Rietveld refinements.

The diffraction spectrum for all samples were collected using Co Kα source (~6930 eV) and a step size of 0.01°. The 2θ range used were 0° to 80° for samples with iron doping less than 0.5 mol%, 0° to 90° for 1.5 mol%, and 17° to 102° for 5.0 mol%. Phases were identified using databases.

To prepare XRD samples, depending on the dimension of the well in the sample holder, excess amount of TiO_2 powders were added and pressed firmly using a glass slide, resulting in a smooth porous sample surface. After cleaning the side of the well, samples together with their holders were placed into the XRD apparatus for measurements.

3.3.2 Morphology: Scanning Electron Microscopy

SEM images were captured in the Advanced Light and Electron Microscopy Facility at York University using a FEI Quanta three-dimensional (3D) dual-beam Field Emission-Focused Ion Beam (FEG-FIB) scanning electron microscope, with an Everhart−Thornley detector working under high vacuum. The morphologies of the synthesized materials were observed, and images were captured with measurable particle sizes.

To prepare a sample, TiO_2 powder was gently touched using clean brushes, followed by dusting the powder to the surface of a high-quality carbon tape placed on a sample

holder. Due to the low conductivity of powdered TiO_2, a thin layer of platinum was sputtered on top of each sample using 35 mA current for 50 seconds. Even though the coating process could slightly affect the particle size measurement, it ensures clear and resolvable images at high magnifications. In the absence of platinum, the resulting picture would be blurry with high noise levels due to accumulation of charge on the surface of the sample. Samples were then transferred to the vacuum chamber of the apparatus to begin the measurement.

3.3.3 Bulk elemental composition: Energy Dispersive X-ray analysis

EDX measurements were performed using the SEM apparatus at York University, with its built-in EDAX X-ray detector. EDX used the SEM sample for elemental composition analysis, thus no further treatments beyond the SEM preparation were needed for this measurement.

3.3.4 Surface elemental compositions and valence band structures: X-ray Photoemission Spectroscopy

The XPS measurements were performed using a VGS ESCALab 250 Imaging ESCA with Aluminum X-ray sources in Waterloo Advanced Technology Laboratory at University of Waterloo.

Spectra were obtained with $400\mu m$ by $400\mu m$ spot size using $Al\ K\alpha$(1486.68 eV), with a pass energy of 30 eV. Both survey and high-resolution spectra were recorded for each sample. The step size for survey spectra was 0.5 eV, and 0.1 eV was used for high-resolution spectra, with the dwell time of 100 milliseconds for each step. Spectra were normalized by appropriate sensitivity factors after collection. All obtained spectra were then analyzed using CasaXPS software (version 2.3.20rev 1.2H), with peaks assigned using National Institute of Standards and Technology (NIST) database.

XPS sample preparations followed the description in a previous chapter (section 3.2.2). To do the measurement, thin film samples were grounded using metallic clips and screws to clamp them down to the sample holder. This process not only stabilizes the sample, but it would also reduce the charging effect on the surface. After purging

samples in the ultra-high vacuum chamber for 24 hours, most of the surface absorbed air and humidity contents were eliminated. Finally, XPS spectra of all samples were collected.

3.3.5 Band gaps: Ultraviolet-Visible Diffuse Reflectance Spectroscopy

To measure the band gap of selected samples, a PerkinElmer Lambda 950 UV−vis−NIR spectrophotometer equipped with a 150 mm integrating sphere was available in Professor Jennifer Chen's lab in the Department of Chemistry at York University. Detailed sample preparation methods of UV-Vis DRS measurements were described in a previous section (section 3.2.2).

Before doing UV-Vis DRS measurements of the prepared films, the spectrum of the percentage reflectance was calibrated using 0% and 99% DRS standard sets. The sample being measured was then clamped in a chamber at the back of the integrating sphere. The chamber was then closed before beginning spectra collection.

3.3.6 Valence band structures: Ultraviolet Photoemission Spectroscopy

The UPS measurements were performed in Waterloo Advanced Technology Laboratory at University of Waterloo, using the XPS apparatus with Helium I source instead.

More specifically, spectra were obtained using $He\ I$ source (21.22 eV), with a pass energy of 1 eV. High-resolution valence band spectra of selected samples were recorded using bias voltage of 0 and -5 V. The step size used was 0.02 eV, with a dwell time of 100 milliseconds for each step. The obtained spectra were analyzed using CasaXPS software (version 2.3.2.rev 1.2H).

UPS sample preparations were done as described in a previous section (section 3.3.2). Similar to XPS, the UPS films were grounded before measurements to eliminate the charging effect as well. In addition, a thin layer of gold covered half of the TiO_2 thin film area, which was used as a reference to the Fermi level of gold of the obtained UPS spectra. Samples were left in the ultra-high vacuum chamber for 24 hours before any data collection.

4 Results and discussions

In this chapter, characterization results by Powder XRD, SEM, EDX, UV-Vis, XPS, and UPS are presented. EDX and XPS were used to determine the doping level of iron for selected samples. Phases and crystallite sizes of the synthesized nanomaterials were determined using XRD, with their morphological properties observed using SEM. Finally, by combining the band gaps measured via UV-Vis DRS with the valence band structure by XPS and UPS, the electronic band structures of TiO_2 with different iron concentrations were proposed.

4.1 Bulk elemental compositions: Energy Dispersive X-ray analysis

In this section, the elemental compositions of selected samples were collected to confirm their iron doping levels.

As EDX determines the elemental composition, measurements were done with theoretically 0 mol% (T7), 0.5 mol% (T8), 1.5 mol% (T12) and 5.0 mol% (T11) Fe doped TiO_2 nanoparticles.

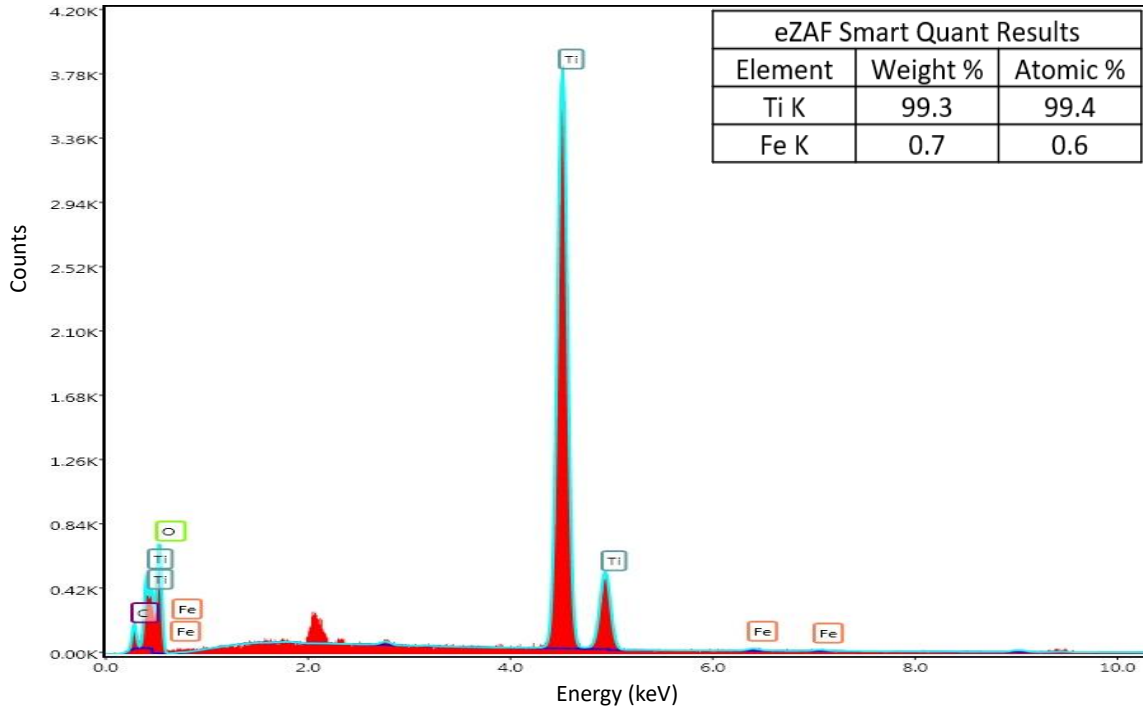

Figure 4.1-1. EDX spectrum of 0.5 mol% Fe doped TiO_2 (T8) nanoparticles.

Spectra were collected at different locations on the surface of the samples. After the spectra were stabilized, databases were used to identify peaks for elemental analysis. As an example, all detected elements are labeled on Figure 4.1-1 for the theoretically 0.5 mol% Fe doped TiO_2 sample. Peaks at around 2.0 keV are excluded from the analysis, which is associated with platinum. Such peak is the detection of the thin layer of coating used to enhance the electrical conductivity property of the sample. Carbon peaks are presented due to the carbon tape for holding the powdered sample as a background. As the doping concentration is low, the intensities of titanium peaks are significant compared with iron peaks. Elemental compositions of all measured samples are summarized in Table 4.1-1.

Table 4.1-1. Theoretical and EDX determined iron doping levels for selected samples.

Label	T7	T8	T11	T12
Theoretical Fe doping level (mol%)	0	0.5	5.0	1.5
EDX Fe doping level (mol%)	0	0.60±0.08	4.68±0.75	2.31±0.32

Results were determined by averaging multiple measurements (minimum of 3, except for T8 which was an average of two) on several surface locations. The iron doping percentage of T12 is higher than expected, while all other samples possess acceptable iron composition levels. The increased iron doping level is likely caused by human error during the synthesis. EDX measurement is a semi-quantitative technique, and it can sample the bulk of the specimen with a typical penetration depth of a few microns[89]. In order to be quantitative, standard of similar roughness and thickness should be employed. For samples with similar characteristics, it is appropriate to compare their bulk compositions. Hence, within uncertainties, EDX confirms that iron was properly doped into TiO_2 for most samples during the synthesis, and the composition of the sample was uniform as seen by the sample standard deviations in Table 4.1-1. Operational mistakes potentially lead to the over-doping of the theoretical 1.5 mol% Fe-TiO_2, which should be confirmed with further characterizations.

4.2 Surface elemental compositions and valence band structures: X-ray Photoemission Spectroscopy

X-ray photoemission technique was employed to study the synthesized nanomaterials in several ways. After proper calibration, high resolution peaks for carbon 1s, oxygen 1s, titanium 2p, iron 2p, and valence spectra were studied to observe the influence of iron doping.

The surface elemental compositions of measured samples are computed using Ti 2p and Fe 2p spectra. Results are summarized in Table 4.2-1.

Table 4.2-1. EDX and XPS elemental compositions of selected samples.

Sample Info.		EDX	XPS
Label	Theoretical Fe doping (mol%)	Fe doping (mol%)	Surface Fe doping (mol%)
T8	0.5	0.60±0.08	0.63±0.20
T11	5.0	4.68±0.75	5.33±0.25
T12	1.5	2.31±0.32	1.84±0.22

Elemental compositions determined by XPS generally agrees with the EDX results. As EDX represents more of the bulk composition compared with XPS, the iron doping is relatively homogenous within the samples being measured. For the 1.5 mol% sample, it is confirmed that the actual doping percentage should be around 2.0 mol%, which could possibly be due to manual mistakes during the sample preparation.

To begin the analysis, all obtained XPS spectra were calibrated individually using their own carbon 1s spectrum for each sample using Shirley backgrounds. As carbon is not in the expected composition, it is not expected to be in our samples. These detected carbon 1s envelopes are due to minor surface contaminations from air, which can be used as a reference to calibrate the measured results. As an example, the carbon 1s peak fitting for 0.5 mol% Fe doped TiO_2 is shown in Figure 4.2-1 a. Calibration was done by confining C-C peak to 248.8 eV, resulting in C-O-C and C-O=C peaks at 286.1 eV and

288.7 eV, respectively. The peak energies were given with an accuracy of ± 0.1 eV based on two measurements.

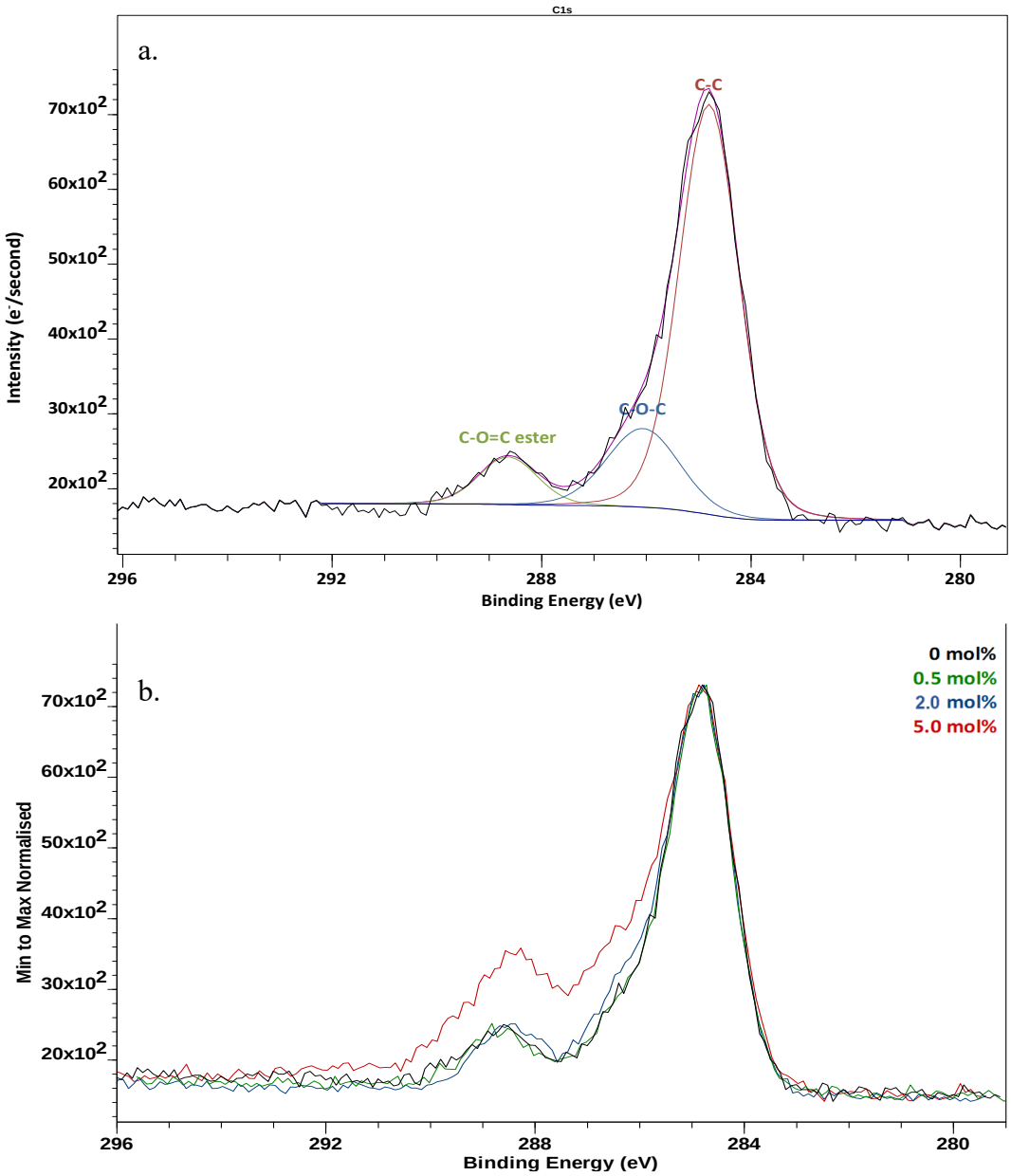

Figure 4.2-1. Carbon 1s high resolution spectra for a. 0.5 mol% iron doped TiO_2, and b. all measured samples.

Deconvoluting using the same technique, the peak components in each spectrum are located at the same position respectively, as illustrated in Figure 4.2-1 b. Detailed component parameters are listed in Table 7.5-2 in the Appendix. (see section 7.5.2). In comparison with other samples, the 5.0 mol% sample has increased intensities of C-

O=C and C-O-C peaks after fitting, which would be the result of slightly higher surface contaminations. These contaminations can be from either the adsorption from the atmosphere or handling, which is unavoidable in *ex-situ* sample preparations.

The oxygen 1s peak of the 0.5 mol% sample can be disintegrated into 2 components: the metal oxide ($-O^{2-}$) at around 530 eV, and the metal hydroxide (-OH) at around 531.5 eV, as shown in Figure 4.2-2 a. The later component is the result of hydroxyl groups, or the detection of moisture on the surface during measurements. By repeating the envelope fitting for all samples, the peak positions of the two components, metal oxide and metal hydroxide, in each envelope were measured to have an energy difference of 1.53±0.10 eV, shown in Figure 4.2-2 b. Details of the components are listed in Table 4.2-2. Meanwhile, all samples present a similar envelope form, thus the bonding states associated with oxygens are homogeneous. However, the observation based on the oxygen 1s peaks for all samples shows that peaks locations are shifted. This could possibly be due to either the charging of the sample, or a miscalibration during the measurement.

Table 4.2-2 XPS components analysis of O 1s peaks for all samples.

Iron doping percentage (mol%)	Metal oxide component	FWHM	Metal hydroxide component	FWHM
0	529.01 eV	1.13	530.41 eV	2.10
0.5	529.86 eV	1.16	531.40 eV	1.87
2.0	529.63 eV	1.19	531.29 eV	1.96
5.0	529.69 eV	1.24	531.19 eV	2.35

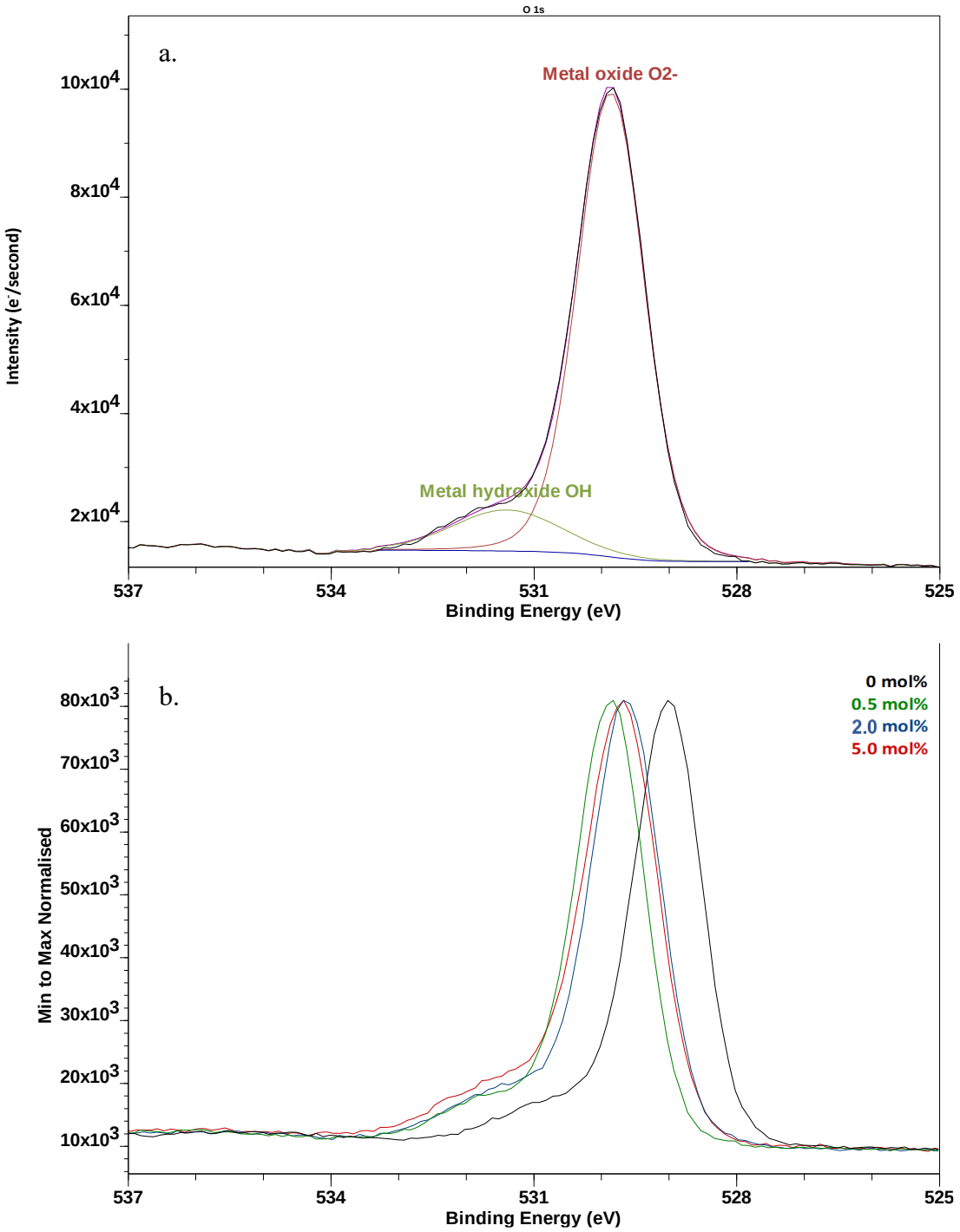

Figure 4.2-2. Oxygen 1s high resolution spectra for a. 0.5 mol% iron doped TiO_2, and b. all measured samples.

The high-resolution spectrum of the 0.5 mol% iron doped sample in Figure 4.2-3 clearly shows the spin-orbit splitting of the Ti 2p orbital, where the $2p_{3/2}$ peak is more intense than the $2p_{1/2}$ peak. The satellite features of these peaks, especially the Ti $2p_{3/2}$ satellite,

can be fitted within the obtained envelope. After proper fittings, the Ti 2p envelope can be constructed using three components: Ti $2p_{3/2}$ at 458.6 eV (Ti^{4+}), Ti $2p_{3/2}$ satellite at 459.0 eV, and Ti $2p_{1/2}$ at 464.3 eV (Ti^{4+}). The satellite peaks can be originated from several factors, such as non-chromatic energy source, or the interactions between the ejected electrons and the surface. No orbitals can be assigned at a lower energy beyond the Ti $2p_{3/2}$ (Ti^{4+}) orbital within the envelope, which means none of Ti^{3+}, Ti^{2+}, or titanium metal were presented on the surface. The component parameters are shown in Table 7.5-2 in the appendix (see section 7.5.2). In addition, the energy split of 5.70 ± 0.03 eV between Ti $2p_{3/2}$ and Ti $2p_{1/2}$ for all spectra further supports such conclusion[90,91]. Meanwhile, the overall spectrum shifts among different samples have indistinguishable amounts comparing with O 1s spectra. For instance, the shift of metal oxide component position from 0 mol% to 0.5 mol% was 0.85 eV, which is very close to the shifting of 0.86 eV observed in their corresponding Ti $2p_{3/2}$ components. Therefore, this confirms that the observed shifting in spectra should be related to the sample charging, because of the low conductivity, or the miscalibration during the measurements, rather than differences of the actual electron orbitals.

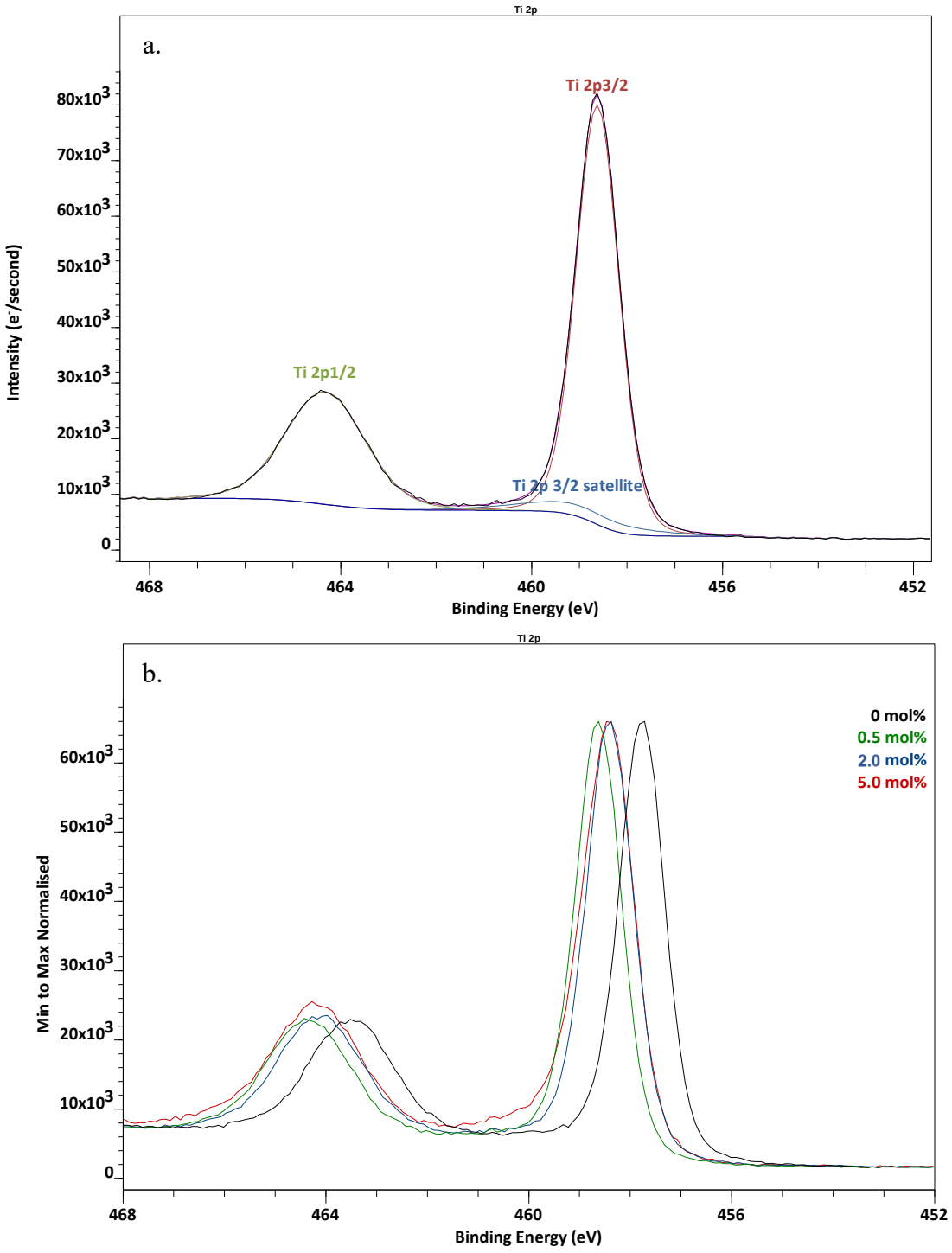

Figure 4.2-3. Titanium 2p high resolution spectra for a. 0.5 mol% iron doped TiO_2, and b. all measured samples.

The collected Fe 2p spectra are tricky to analyze due to their low signal to noise ratio. However, a comparative study can be conducted within the measured samples. Figure 4.2-4 illustrates the Fe 2p peaks obtained from samples with various doping levels.

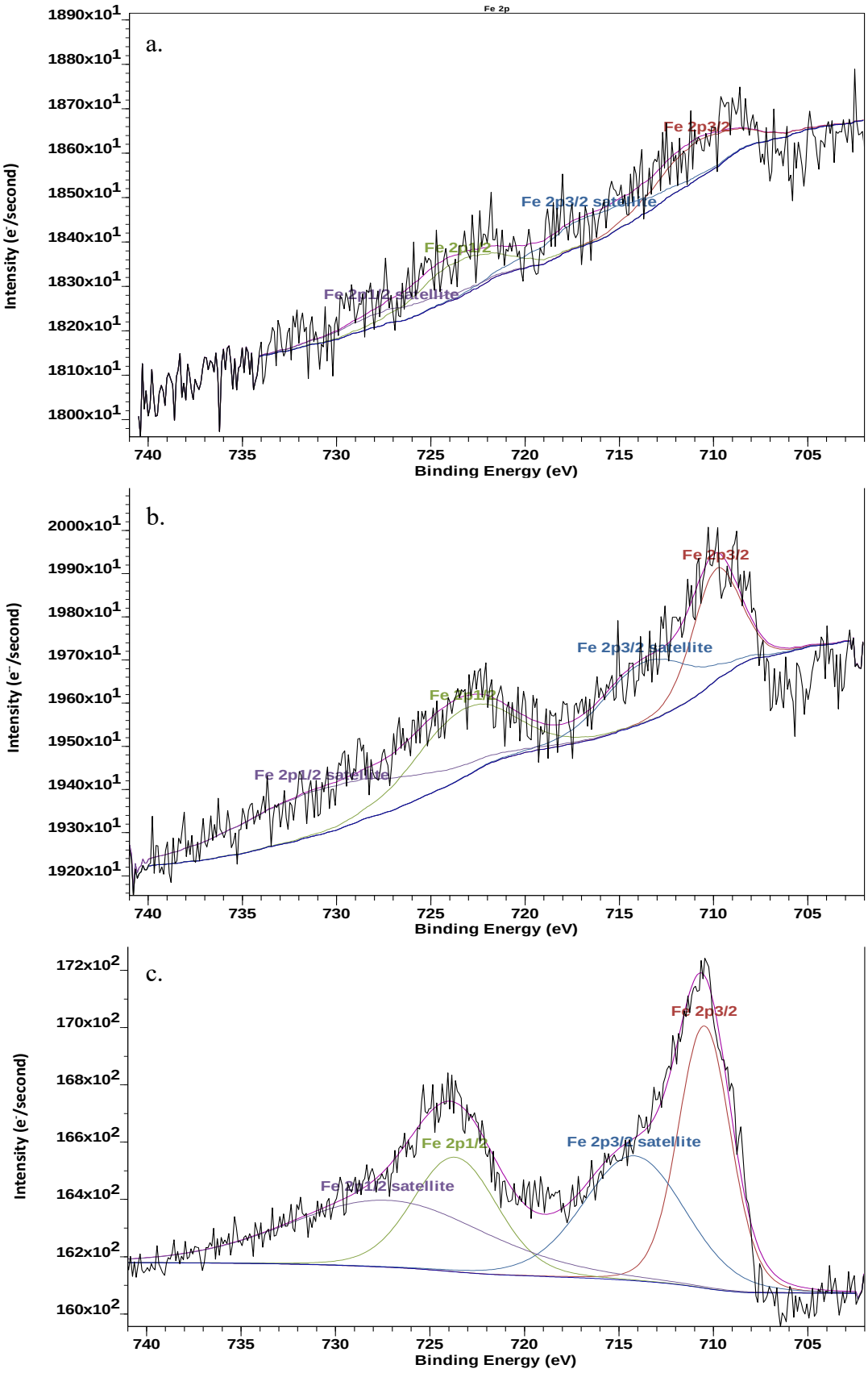

Figure 4.2-4. Iron 2p high resolution spectra for a. 0.5 mol%, b. 2.0 mol%, and c. 5.0 mol% iron doped TiO_2.

As the iron doping levels of synthesized samples are relatively low, it would lead to a lower signal to noise ratio, such that extra measuring time is essential for samples with low iron contents. The Fe 2p envelope can break down into 4 components, namely Fe $2p_{3/2}$, Fe $2p_{1/2}$, and their corresponding satellites. Detailed component fitting can be found in Table 7.5-2 (see section 7.5.2). Yamashita analyzed the Fe 2p peak using XPS after calibrating the C-C component of carbon 1s peak to 285.0 eV. The positions of Fe^{3+} $2p_{3/2}$ and $2p_{1/2}$ components were located at 711.0 ± 0.01 eV and 724.6 ± 0.17 eV respectively, while the corresponding Fe^{2+} components were 2 eV lower in binding energy[92]. By using Yamashita's approach, our results give the component locations at 710.0 ± 0.5 eV for Fe $2p_{3/2}$, and 723.4 ± 0.4 eV for Fe $2p_{1/2}$. The locations of these components lie on the lower range of the previous study. This leads to the possibility that Fe^{3+} and Fe^{2+} were both present on the analyzed surface. More precise results can be achieved using higher resolution spectra to minimize the error while fitting. Thus, the spectrum of 5 mol% Fe doped sample is carefully fitted due to its lower noise level for more details.

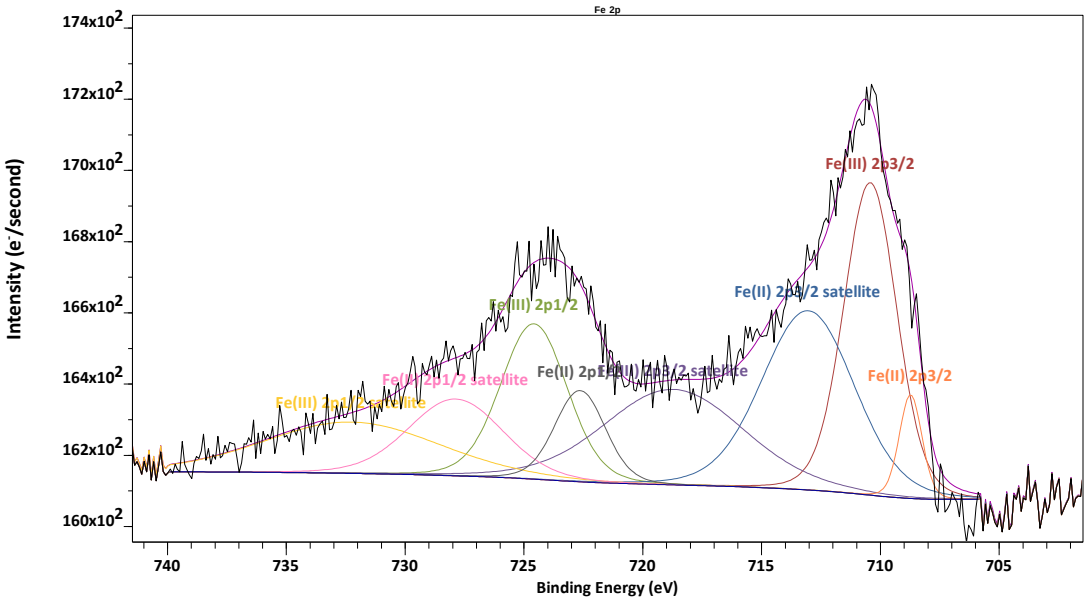

Figure 4.2-5. Iron 2p high resolution spectrum with detailed fitting components for 5.0 mol% iron doped TiO_2.

From Figure 4.2-5, all possible components from the Fe 2p envelope are shown in colored lines. Both Fe^{3+} and Fe^{2+} features can be observed from the fitted envelope. Fe $2p_{3/2}$ at 710.4 eV and Fe $2p_{1/2}$ at 724.58 eV, together with their corresponding satellites at 718.7 eV and 732.3 eV can all be assigned to the existence of Fe^{3+}. Peaks associated with Fe^{2+} are located at 708.7 eV, 713.0 eV, 722.6 eV and 727.9 eV, corresponding to Fe $2p_{3/2}$ and its satellite, as well as Fe $2p_{1/2}$ and its satellite[92,93]. Such result is also observed in a recent study by Ismail and colleagues, where both Fe^{2+} and Fe^{3+} were detected in their iron-doped samples. They also found that, by increasing the iron doping amount, the portion of Fe^{3+} increases comparing to Fe^{2+} [94]. Thus, it confirms that both Fe^{3+} and Fe^{2+} were presented on the surface while measuring. As for Fe^{4+}, it is an unstable state, therefore its concentration should be relatively low compared to Fe^{3+} or Fe^{2+} if present. In consequence, the relative peak intensity associated with Fe^{4+} would be low, which could explain why the Fe^{4+} component was missing from the Fe 2p peak fitting.

4.3 Crystal properties: Powder X-Ray Diffraction analysis

The powder XRD patterns for all samples were acquired to determine all phases presented. Crystallite size of each sample was estimated to see its dependence on preparation conditions, such as iron doping level, calcination temperature, as well as the H_2O:EtOH ratio used in the sol-gel synthesis.

To provide a way to understand how Fe-doping affects the structure of TiO_2, we first measured the XRD pattern of a pure TiO_2 sample prepared using the condition listed under T7 in Table 3.1-2. The powder XRD patterns are shown in Figure 4.3-1, where peak positions for the anatase phase identified in red using databases. Peak positions and their relative intensities for the anatase phase matched well to the standard anatase material (PDF 00-021-1272) in the measured XRD pattern, and there were no other phases observed within the chosen range.

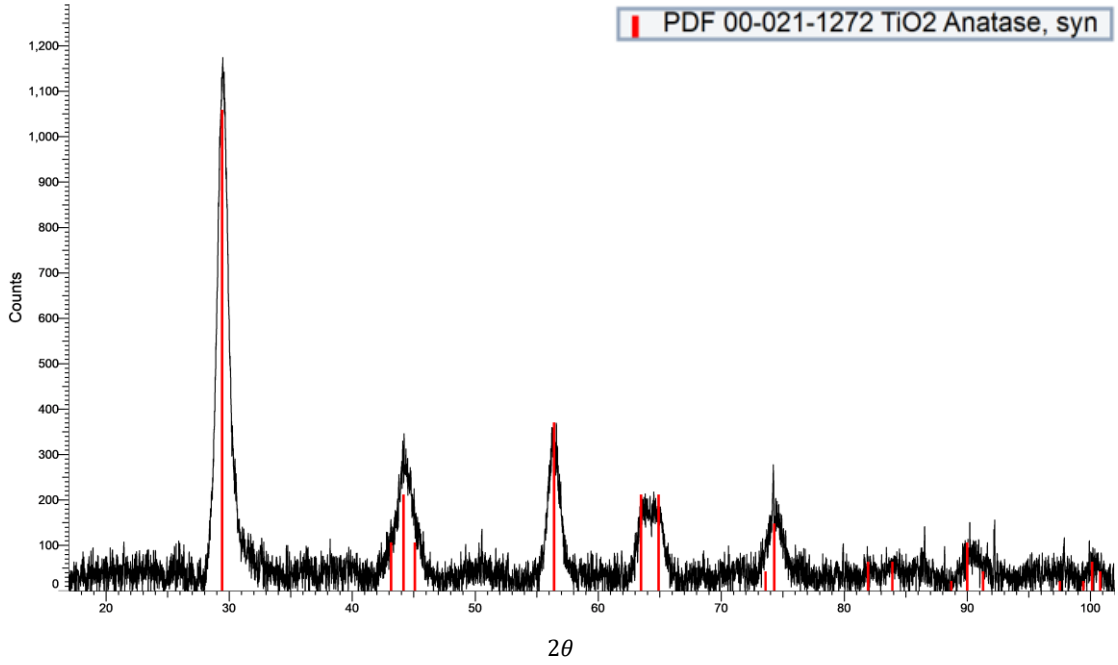

Figure 4.3-1. Powder-XRD pattern for T7 (undoped, EtOH:H_2O=138:138, $T_{calcination}$=450 °C). Black line represents the obtained XRD patterns, with phases identified using colored lines.

Only the anatase phase was present in sample T7, which is consistent with the annealing temperature of 450 °C from the phase diagram in Figure 1.1-1. The phase transition from anatase to rutile is expected around 500 °C, with a complete transformation around 600 °C [25–28,95]. After applying Rietveld refinement, the average crystallite size was estimated to be 10.7 nm using the full XRD pattern from the Scherrer equation, with the error of 0.1 nm from fitting the measured patterns and calculations by software.

Using the same approach, samples with various iron doping percentages and preparation conditions were investigated. The patterns are shown in Figure 4.3-2.

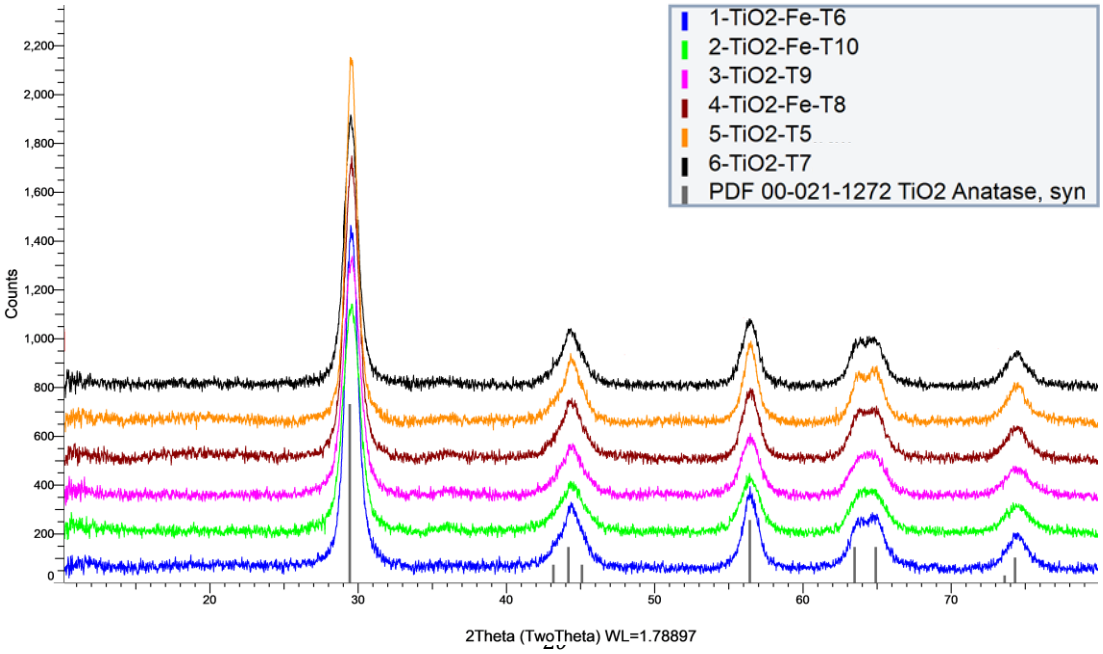

Figure 4.3-2. Powder-XRD patterns from T5 to T10. Colored lines represent XRD patterns, with grey lines identifying phases.

Like T7, for doping with less than 0.5 mol% of iron, samples only showed the anatase phase. This suggests that iron had been successfully doped inside of the TiO_2 matrix without changing the lattice structure, which might be favored by the similar ion radius for Ti^{4+} and Fe^{3+} [11].

However, for higher doping concentrations, phases such as brookite and Fe_2O_3 were present to various degrees. From Figure 4.3-3 a and b, one can see that when the iron doping level increases above 0.5%, changes in phase compositions are observed.

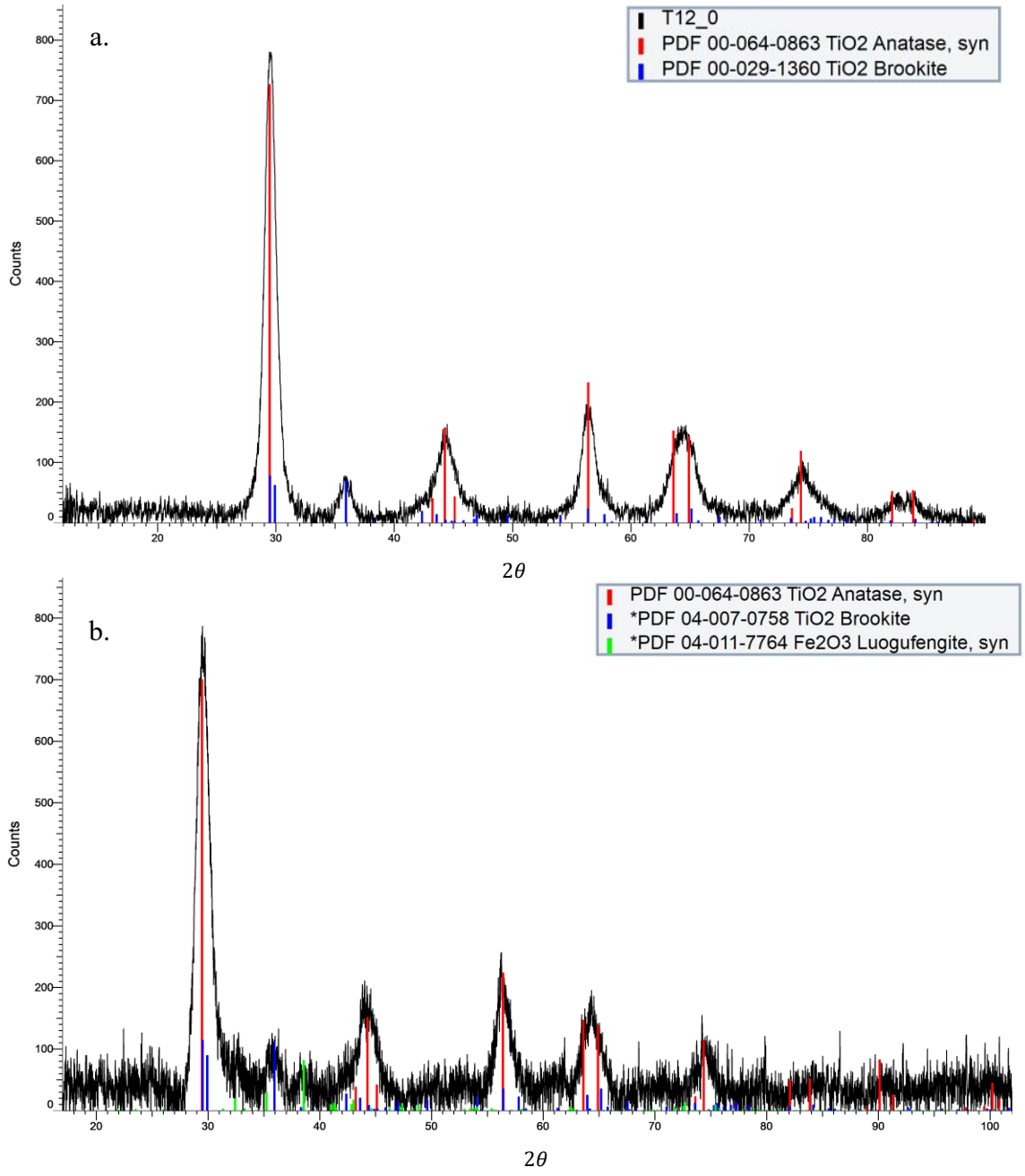

Figure 4.3-3. Powder-XRD spectrum for a. T12 (2.0 mol% Fe, EtOH:H_2O=138:138, $T_{calcination}$=450 °C), and b. T11 (5.0 mol% Fe, EtOH:H_2O=138:138, $T_{calcination}$=450 °C). Black line represents the corresponding XRD patterns, with brookite phase peaks showing in blue, and Fe_2O_3 in green.

For samples T12 and T11 containing 2.0 mol% and 5.0 mol% of iron, respectively, the majority phase for both samples is still anatase. Results show that T12 contains anatase of 89 wt.%, while T11 has 82 wt.%. 13 wt.% of brookite phase, shown as blue lines,

with 5 wt.% of Fe_2O_3, illustrated as green lines, are identified in T11. The presence of Fe_2O_3 is originated from the precipitation of iron nitrate nonahydrate during the sol-gel process, which would happen simultaneously while synthesizing TiO_2 nanoparticles with iron doping using our method.

Based on our result, samples with higher iron loadings have more brookite phase. There are two possible reasons for the detection of the brookite phase. On one hand, the formation of brookite phase could be directly related to the iron doping concentration, as a study from Popa and coworkers suggested, where more iron dopants shortened the lattice parameter c of TiO_2, which may favor the formation of the brookite phase[96]. From our measurements, the lattice parameter c slightly decreases from 9.51 (T7, undoped; T8 0.5 mol% Fe) to 9.49 (T12, 2.0 mol% Fe; T11, 5 mol% Fe), and such deformation in anatase lattice could be related to the ionic radius decrease arising from the substitution of Ti^{4+} (0.67 Å) with Fe^{3+} (0.64 Å). On the other hand, preparation conditions, particularly the pH of the sol-gel process, could alter the phase composition of the final product. Since the only preparation difference between T7, T8, T11, and T12 is the amount of iron nitrate nonahydrate added, and such iron salt is acidic, this could result in a slight change of the pH condition during the sol-gel reaction. This is supported by Meng *et al*, where acidic growth environments lead to the formation of rutile and brookite in the sol-gel synthesis, with brookite nucleation rate being faster[97]. However, Fàbrega and colleagues synthesized sample with iron doping percentages from 0 to 0.62 at. % using the sol-gel method. Results showed that all iron doped samples had brookite phase with calcination temperature less than 800 °C. They claimed that there was no direct correlation between the iron doping level and fraction of brookite phase found[98]. In general, the truth behind the brookite formation is still unrevealed, and more investigations are necessary to discover its mechanism.

To learn about the influence of preparation conditions and iron doping on crystallite sizes, the Scherrer equation was used to estimate these values after Rietveld refinements. The crystallite size results are listed for all samples in Table 4.3-1.

Table 4.3-1. Preparation conditions and the average crystallite size estimation by Powder-XRD analysis.

Label	Fe doping level (mol%)	DI H_2O: EtOH (ml: ml)	Calcination temperature (°C)	Crystallite size (nm) for anatase (±0.1nm)	Crystallite size (nm) for brookite (±0.1nm)
T5	0	69:69	450	13.2	Not present
T6	0.5	69:69	450	11.6	Not present
T7	0	138:138	450	10.7	Not present
T8	0.5	138:138	450	10.3	Not present
T9	0	138:138	350	8.9	Not present
T10	0.5	138:138	350	8.7	Not present
T11	5	138:138	450	13.0	10.9
T12	2.0	138:138	450	12.0	13.0

The influences due to iron doping concentration, H_2O:EtOH ratio, and calcination temperature on the crystallite size in anatase phase are summarized in Figure 4.3-4. The errors in the size estimations for each phase are not a representation of the width of the particle size distribution, as those values are obtained from fitting and calculations. The actual crystallite size distribution could be obtained via multiple measurements in future studies.

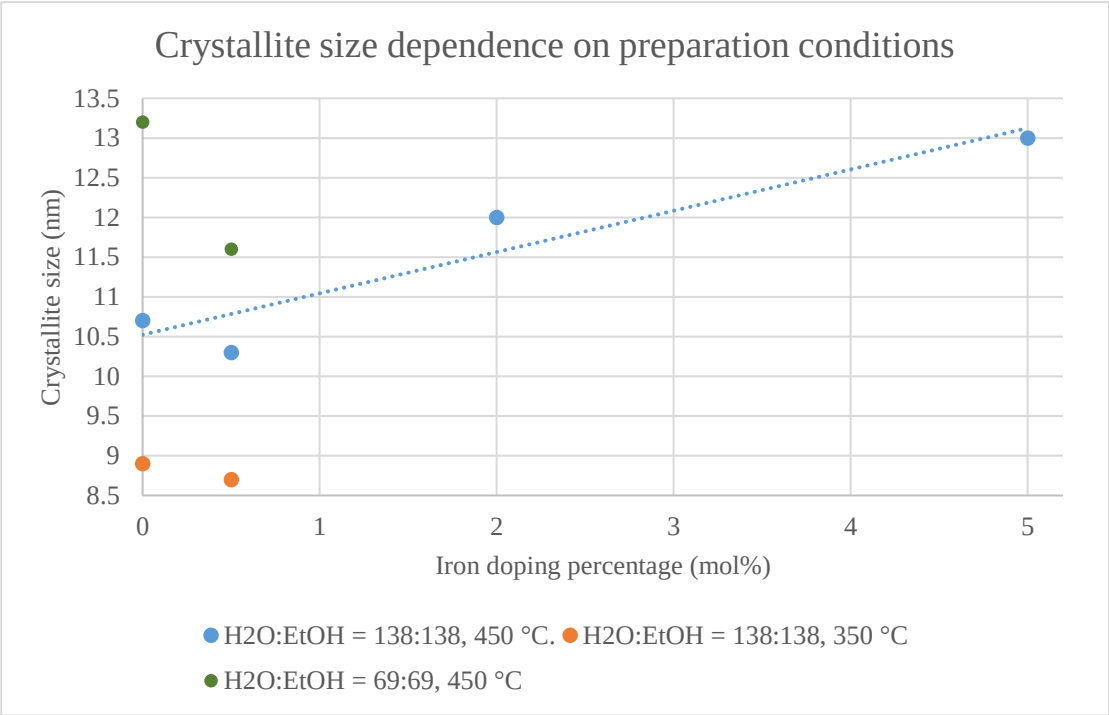

Figure 4.3-4. Relationships between crystallite size estimated by Powder-XRD and iron doping level for materials prepared with a H_2O:EtOH ratio of 138:138 and calcination temperature of 450 °C shown with blue circles. Effects of lowering the calcination temperature to 350 °C, and of decreasing the amount of available water (H_2O:EtOH ratio of 69:69) are shown with orange and green circles, respectively.

By comparing with blue and green circles in Figure 4.3-4, a conclusion can be made that anatase phase TiO_2 crystallites are slightly smaller in size when an excess amount of deionized water was added during the sol-gel reaction, with or without iron doping. In principle, TiO_2 nanoparticles were formed when the first drop of TTIP and EtOH mixture interacted with the mixture of water and EtOH. Due to the excess amount of water, the hydrolysis rate of such titanium alkoxide was high, leading to a shortened duration of nucleation and growth[40–42]. In other words, the initially formed nanoparticles acted like seeds during the sol-gel reaction. Excess amount of water made each seed smaller, and the substance was limited for the seeds to grow larger. Therefore, higher water contents would result in smaller particles overall by the end of the synthesis.

A smaller crystallite size can be also achieved by lowering the calcination temperature

by comparing blue and orange data points in Figure 4.3-4. With doping less than 0.5 mol%, samples calcinated at 350 °C possess smaller crystallites than at 450 °C. Similar phenomenon has also been observed by Li and colleagues, who used a variety of preparation conditions via sol-gel method for TiO_2 nanoparticle synthesis. Their results showed that the crystallite sizes are much smaller at lower calcination temperatures, due to a lowered activation energy of crystal growth[63].

In addition, iron doping level also affects the crystallite sizes, where the size tends to increase with a higher iron doping percentage. Previous studies have synthesized TiO_2 nanoparticles using a range of doping percentages, where the optimal doping level of iron was 0.5 mol% yielding a mean crystallite size of 9 ± 2 nm [12]. In the case of silver-doping, the smallest crystallite size was obtained at 0.75 at. % , with size equal to 17 nm [99]. As in our result, the crystallite size at 0.5 mol% iron doping is only 0.4 nm smaller in diameter comparing with the undoped sample. Since the current uncertainty determinations were based on calculations after Rietveld refinements for each sample, the estimated crystallite sizes could be smaller than their true sizes. Therefore, it is hard to conclude that 0.5 mol% is the optimal doping percentage to minimize the crystallite sizes.

4.4 Morphology: Scanning Electron Microscopy

We used SEM to observe the synthesized nanomaterials to confirm their similarities in morphology, and particle size estimation was acquired based on the captured images. First, all synthesized samples are illustrated in Figure 4.4-1, with identical magnifications for all images at 150,000 times.

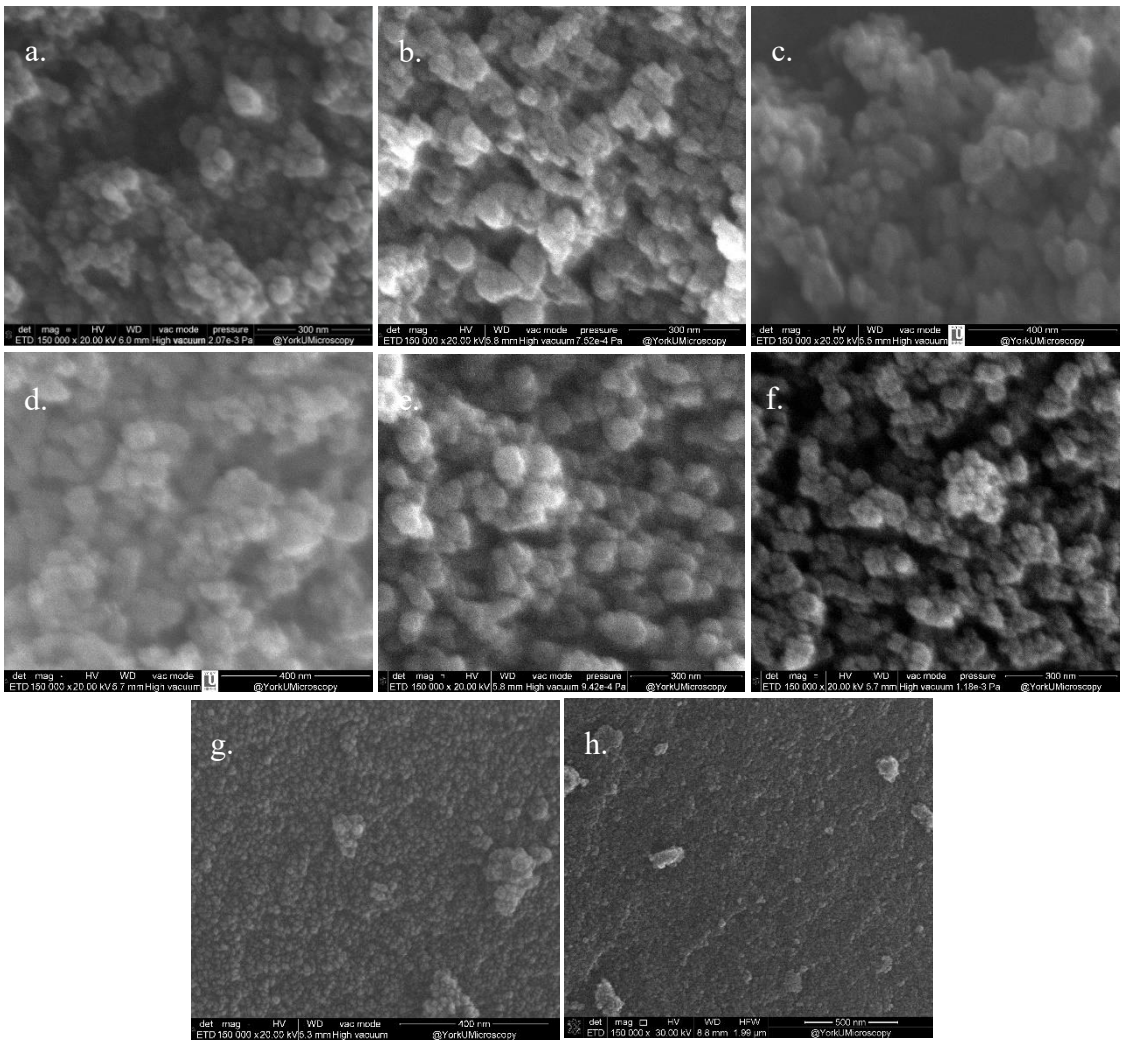

Figure 4.4-1. SEM images captured at 150000-time magnifications for a. T5; b. T6; c. T7; d. T8; e. T9; f. T10; g. T11; and h. T12.

Each image represents the topography of the corresponding sample. Samples are in the form of agglomerates, which were formed during the drying and calcination process. Grinding could break apart the agglomerates into separated nanoparticles, however, ultra-fine powders were not achieved using mortar and pestle in the current synthesis. Thus, more advanced techniques, such as ball-milling, should be applied in the future to obtain finer powders. From captured images, all particles are of a similar spherical shape. Within one sample, nanoparticles are of a similar size in diameter.

Images at much higher magnifications are used to study the size distributions of different samples using ImageJ software. Results are shown in Table 4.4-1.

Table 4.4-1. SEM nanoparticle diameter distribution using ImageJ.

Label	Fe doping percentage (mol%)	Calcination temperature (°C)	H_2O:EtOH (ml:ml)	Mean size (nm)	σ (nm)
T5	0	450	69:69	47.2	8.5
T6	0.5	450	69:69	52.4	8.7
T7	0	450	138:138	62.3	11.6
T8	0.5	450	138:138	63.2	11.6
T9	0	350	138:138	55.1	9.9
T10	0.5	350	138:138	51.6	6.4
T11	5	450	138:138	16.1	2.4
T12	2.0	450	138:138	16.6	2.6

The particle sizes and distributions above may not represent the true size of the synthesize nanoparticles, as they are estimated using images captured with limited resolution. However, the error level for all images at the same magnification would be similar, such that a relative study is reasonable.

From the distribution statistics, particles within one preparation condition generally have a uniformed size, with a standard deviation less than 20%. The mean particle size for each sample is similar to, or few times larger than the crystallite size determined by XRD analysis. This is because for any particle, it can contain one or more crystallites. Moreover, T11 and T12 have similar particle sizes as from XRD crystallite size, while

particles with little to no iron doping have their particle diameter 3 to 4 times larger than the crystallite size. Since the same milling technique and procedure were applied during the synthesis, it can be inferred that iron doping at higher concentrations can help limiting the particle size via sol-gel synthesis.

4.5 Band gaps: Ultraviolet-Visible Diffuse Reflectance Spectroscopy

UV-Vis DRS was used to determine the band-gap values of samples with iron doping from 0 to 5.0 mol%. Both direct and the indirect band gaps are calculated using the Kubelka-Munk model, and the effect of iron doping to the band gaps are illustrated using the measured results.

The as collected UV-Vis DRS spectra for 0 mol% (T7), 0.5 mol% (T8), 2.0 mol% (T12), and 5.0 mol% (T11) Fe-doped TiO_2 were collected using the procedure described in section 3.4.4 and are shown in Figure 4.5-1.

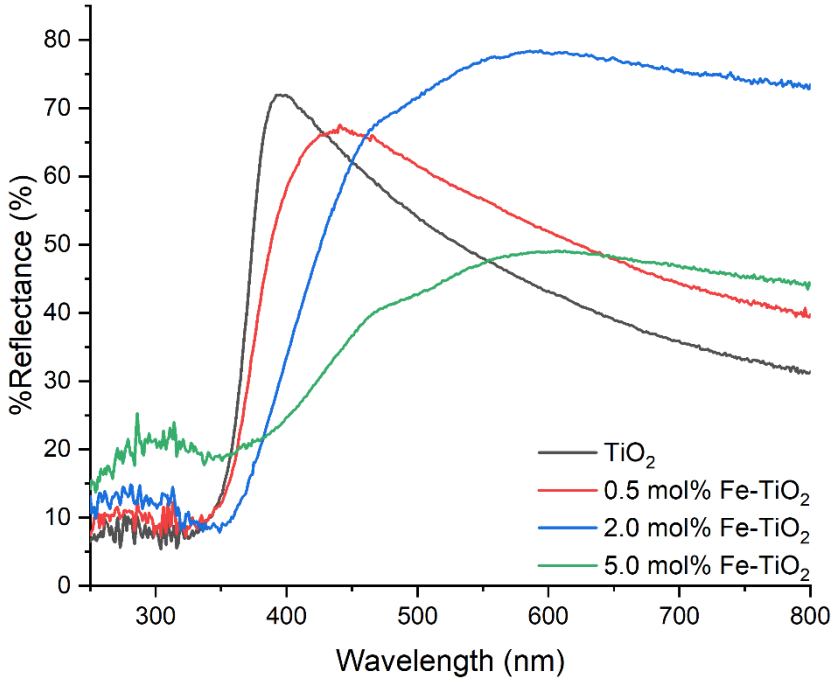

Figure 4.5-1. UV-Vis DRS spectra for T7 (black), T8 (red), T11 (green), and T12 (blue). The abscissa is the wavelength, and the ordinate is the measured percentages of reflectance.

The reflectance percentage (%R) for all samples are normalized for better comparison reasons, and the data are shown in Figure 4.5-2. From this figure, the peak reflectance of the sample shifts toward a longer wavelength as the doping percentage increases.

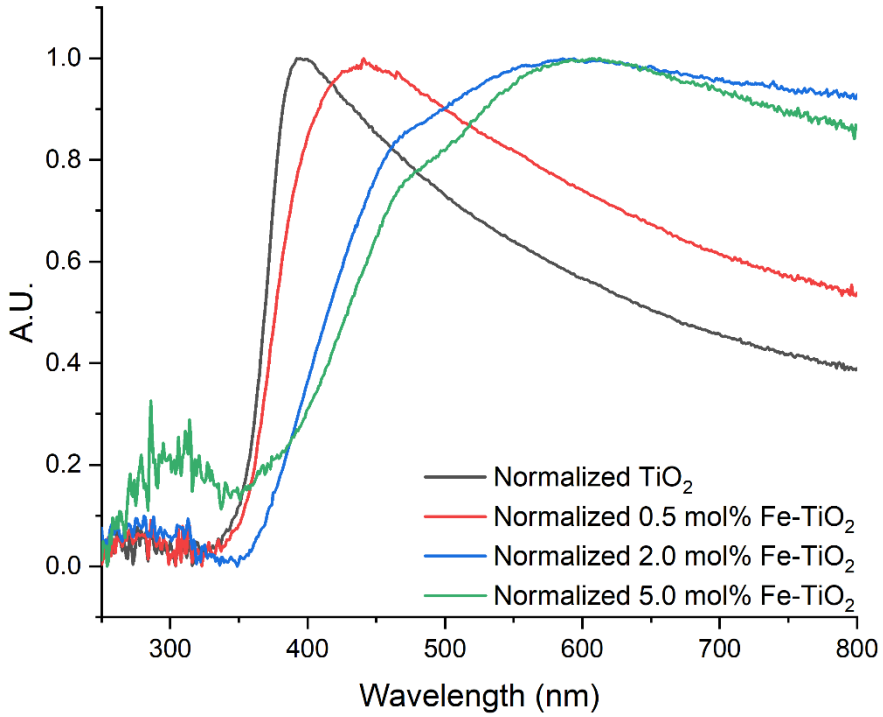

Figure 4.5-2. Normalized UV-Vis DRS spectra for T7 (black), T8 (red), T11 (green), and T12 (blue). The abscissa is the wavelength, and the ordinate is the normalized percentages of reflectance in arbitrary units (A.U.).

Using data from Figure 4.5-1, the corresponding direct and indirect band gaps for all measured samples can be computed by following the procedure in the Appendix (section 7.4.3). By assigning the band type constant $n = 2$, the direct band gap spectra are converted from the percentage of reflectance to $(\frac{F(R)h\nu}{t})^2$ via the Kubelka-Munk function (section 2.4, equation (5) and (6)):

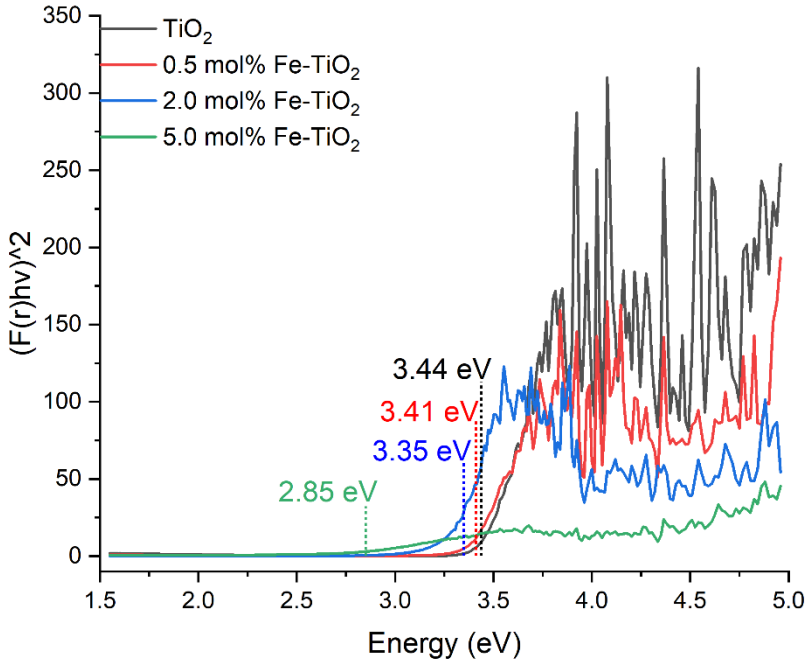

Figure 4.5-3. Direct band gap spectra for T7 (black), T8 (red), T11 (green), and T12 (blue). The abscissas are the photon energy, and the ordinates are the corresponding $(F(r)hv)^2$ values determined using the Kubelka-Munk function.

Even though titanium dioxide in anatase phase mainly presents an indirect band gap, the direct band gap can be measured from UV-Vis DRS. In Figure 4.5-3, the effect of iron doping on the band gap results in the narrowing of the direct band gap from the computed spectra.

On the other hand. by changing the factor $n = 0.5$, the indirect band gaps can be obtained for all measured samples (see Figure 4.5-4). It shows that higher iron doping levels would also give smaller indirect band gap values.

The band gap values of both types can be extrapolated by taking the energy intercept at $\%R = 0$ using linear fitting models on the shoulder of unnormalized spectra (Appendix, section 7.4). The resulting band gaps for all measured samples are summarized in Table 4.5-1.

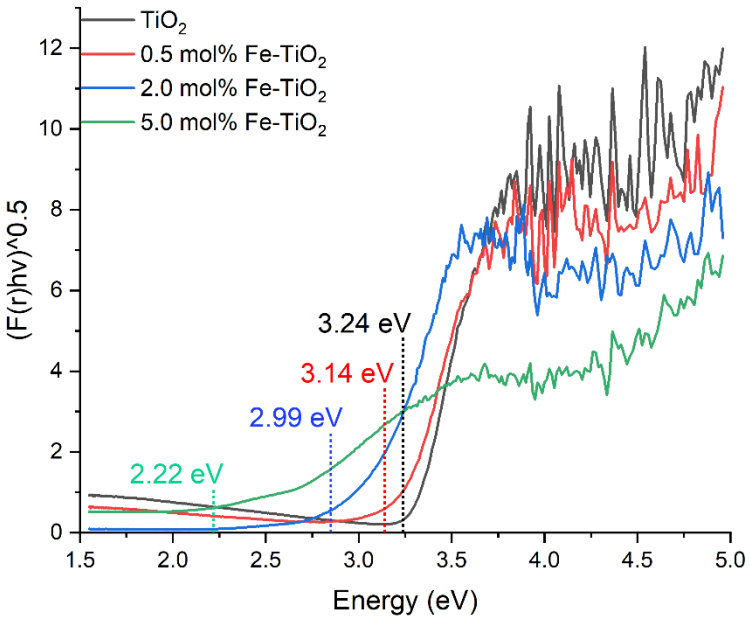

Figure 4.5-4. Indirect band gap spectra for T7 (black), T8 (red), T11 (green), and T12 (blue). The abscissa is the photon energy, and the ordinate is normalized $(F(r)hv)^{0.5}$.

Table 4.5-1. Band gap values of 0 mol% (T7), 0.5 mol% (T8), 2.0 mol% (T12), and 5.0 mol% (T11) Fe doped TiO_2 nanomaterials.

Label	Fe doping level (mol%)	Direct band gap (eV)	error (eV)	Indirect band gap (eV)	error (eV)
T7	0	3.44	0.20	3.24	0.06
T8	0.5	3.41	0.24	3.14	0.08
T11	5.0	2.85	0.10	2.22	0.02
T12	2.0	3.35	0.36	2.99	0.16

Combining the band gap values with the XPS and EDX elemental composition results, the relation between the band gap values and the iron doping percentages as illustrated in Figure 4.5-5.

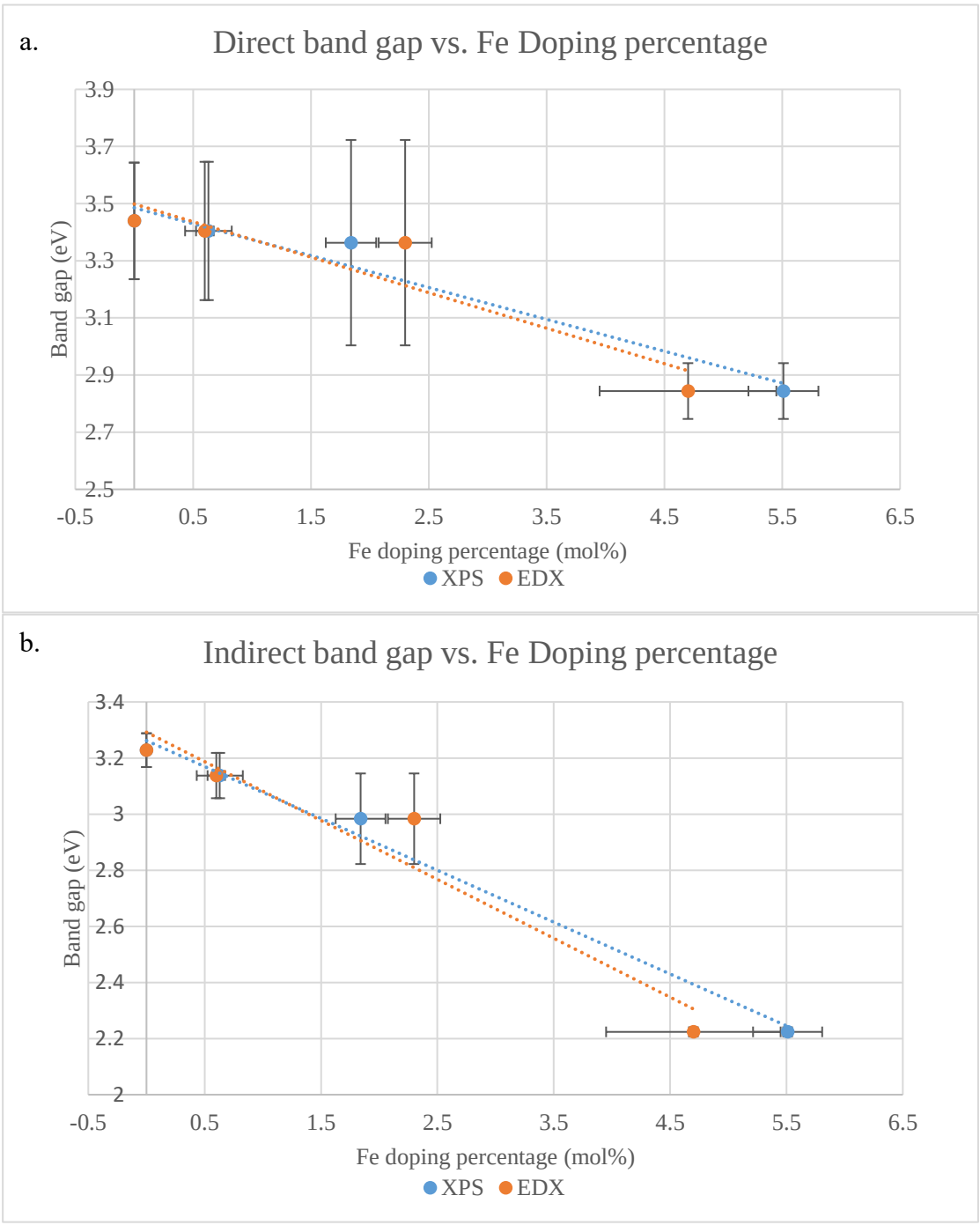

Figure 4.5-5. Relation of UV-Vis DRS measured a. direct, and, b. indirect band gap values, versus the XPS (blue circles) and EDX (orange circles) measured Fe doping percentages of synthesized samples.

The uncertainties in band gap values are determined from the linear fitting model. Independent of the band gap type, the band gap decreases with a higher iron doping

level according to Figure 4.5-4 a. and b. By comparing the values of known iron doping percentages reported in the literature, the measured band gaps are within expectation for this type of material. Using the same Tauc plot method, Nazari demonstrated a decreased indirect band gap from 3.12 eV to 2.30 eV by introducing up to 5.0 mol% Fe to TiO_2 nanoparticles[12]. Christoforidis and coworkers measured the band gaps of samples with iron doping percentage from 0 mol% to 1.5 mol%, and the indirect band gaps were narrowed from 3.12 eV to 2.87 eV[100]. Other studies using different methods for band gap determination, such as fittings on the absorbance and transmittance spectra, have also observed decreases in band gaps for higher iron doping levels, with values comparable to our study[101,102].

Such conclusion can be applied to explain the theoretical enhancement of methylene blue photodegradation using iron doped TiO_2 nanoparticles as a catalyst[18]. Due to the band gap narrowing by the iron dopants, the doped material extends its absorption wavelength from UV to visible region. This process would increase the range and the amount of energy absorbed by the nanoparticle to generate electrons and holes. In principle, combining with the context of the indirect dye decomposition mechanism, a higher rate of OH radicals' production is expected with a higher doping level, which should result in a faster dye photodegradation process.

4.6 Valence band structure: X-ray Photoemission Spectroscopy

The valence band spectra are obtained using XPS with a lower energy input. Illustrated in Figure 4.6-1 a. is the normalized valence band XPS spectra for all measured samples after proper calibrations.

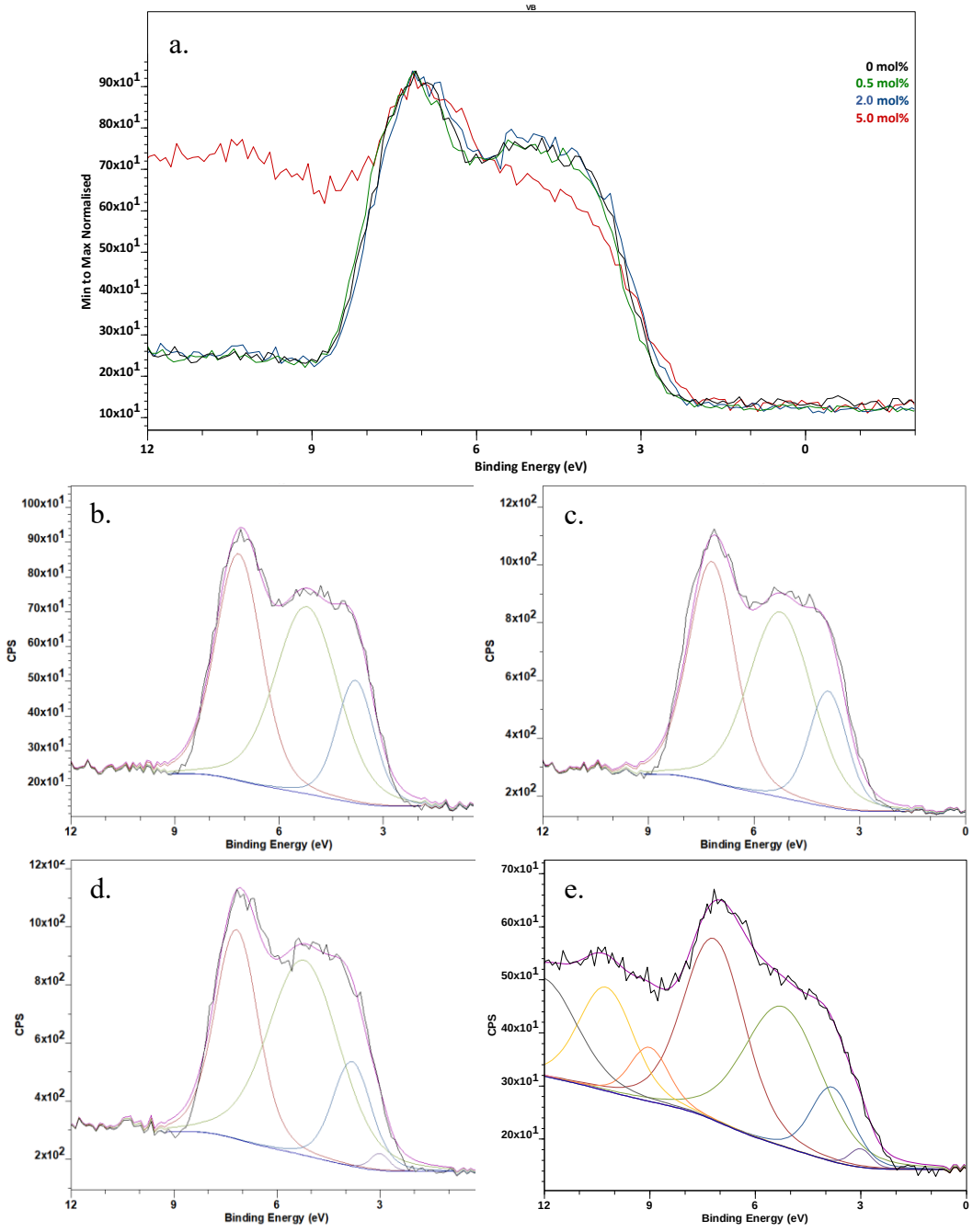

Figure 4.6-1 a. Valence band XPS spectra for 0 mol% - 5.0 mol% Fe doped TiO_2 nanoparticles, and b to e. the valence band fitting for 0 mol% - 5.0 mol%.

The rise from 9 eV to 12 eV for the 5.0 mol% sample is the result of minor charging effects. The envelope within the shown energy range consists of 4 major components. Detailed fitting parameters are listed in Table 7.5-4 in the appendix (see section 7.5.2). All spectra contain the components related to anatase TiO_2 at around 7.2 ± 0.01 eV, 5.2 ± 0.02 eV, and 3.8 ± 0.03 eV. These are the result of O 2p orbitals, Ti 3d orbitals, as well as their hybridizations. The peak at around 3.0 eV rises as iron doping level increases, which correspond to the Fe 3d-O 2p hybridized orbital by iron doping. These features have also been observed in other studies[68,94,103], however, the expected states due to Ti^{3+} defects are not observed at lower binding energies in any of the measured samples.

The valence band edge can be estimated by fitting the spectrum shoulder around 3 eV using linear models (Appendix, section 7.5). Results give valence band maximum positions at 2.52 ± 0.29 eV, 2.50 ± 0.34 eV, 2.39 ± 0.23 eV, and 2.17 ± 0.32 eV for 0 mol%, 0.5 mol%, 2.0 mol%, and 5.0 mol% Fe doped TiO_2 nanoparticles. The relation between characterized iron doping levels and positions of valence band maximum from XPS is illustrated in Figure 4.6-2. Such relationship shows, that with higher iron doping levels, the valence band edge is brought closer towards the conduction band. Doping with iron would turn TiO_2 into an *n*-type semiconductor. This in principle would only affect the conduction band structure, such that the conduction band position should be closer to the valence band. However, our results illustrated the overall valence band position shifted towards a lower binding energy with higher iron contents, which would cause the band gap narrowing of the measured TiO_2 samples on the valence band side as well.

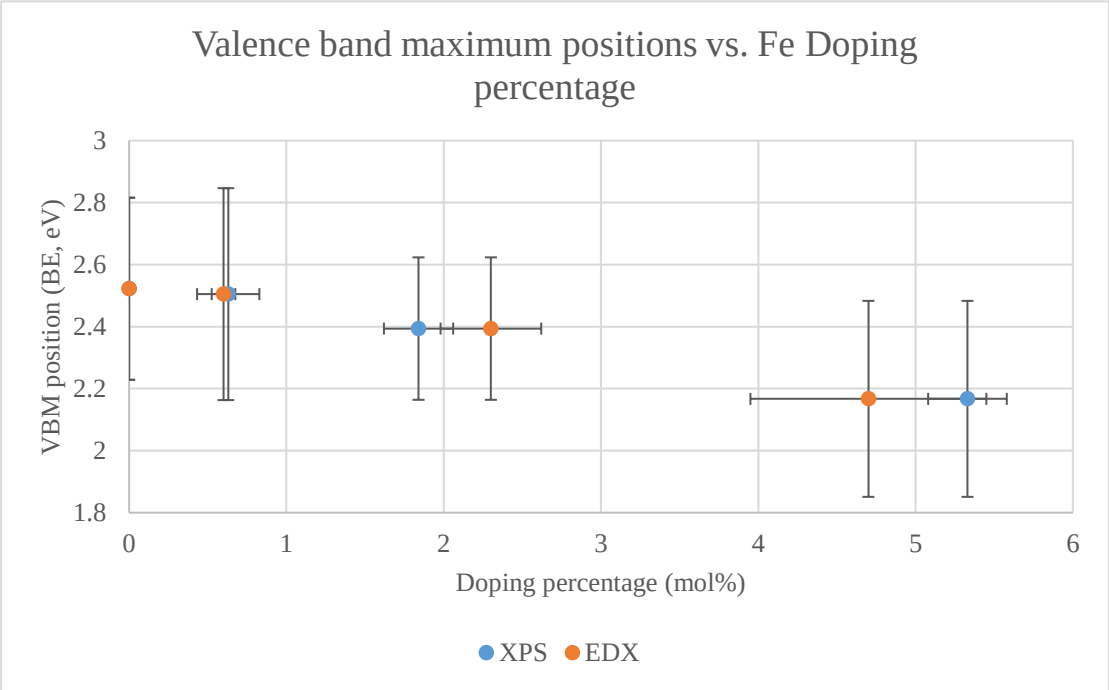

Figure 4.6-2 The relation of iron doping levels and valence band maximum positions. The actual iron doping levels are presented in blue and orange circles, which values were determined using XPS and EDX, respectively.

In terms of the valence band components, the valence band maximum shift with higher doping percentages towards a lower binding energy could be a consequence of higher intensities of Fe 3d-O 2p hybridized orbital. Such hybridized orbital at around 3.0 eV due to iron doping can act as an electron trap, where electrons from the conduction band would stay at the iron-created orbital before travelling to the valence band, resulting in a lowered rate of recombination during emission process. Previous studies by two research groups all stated the possibility of the sub band creation near the TiO_2 valence band due to Fe^{4+} [53,54]. From our XPS chemical state analysis of the Fe 2p peak fittings, the contribution from Fe^{4+} was not detected because of the low Fe^{4+} concentration if present. In this case, the modification on the valence band would not be significant, which supports our measured results from the XPS valence band fitting. Overall, this is in favor of a higher rate of OH radical generation. However, since the relation between Fe 3d-O 2p hybridized orbital and the recombination rate is unknown, more work

should be done to conclude the influence of the iron doping percentage to the overall photodegradation rate quantitatively.

Another possibility of the modification by iron could be done to the valence band by introducing oxygen vacancies, which would affect the O 2p orbital. However, since the detection of oxygen vacancies cannot be accomplished via XPS, new characterization methods should be applied in future studies to verify such possibility.

4.7 Valence band structures: Ultraviolet Photoemission Spectroscopy

The valence band spectra of samples with various iron doping levels were measured using UPS, to observe the modification to the valence band structure upon doping.

UPS spectra were collected using a thin evaporated gold layer deposited on top of the TiO_2 sample as a reference with respect to the Fermi level of gold. First, the spectra for the gold film deposited on top of different samples are shown in Figure 4.7-1.

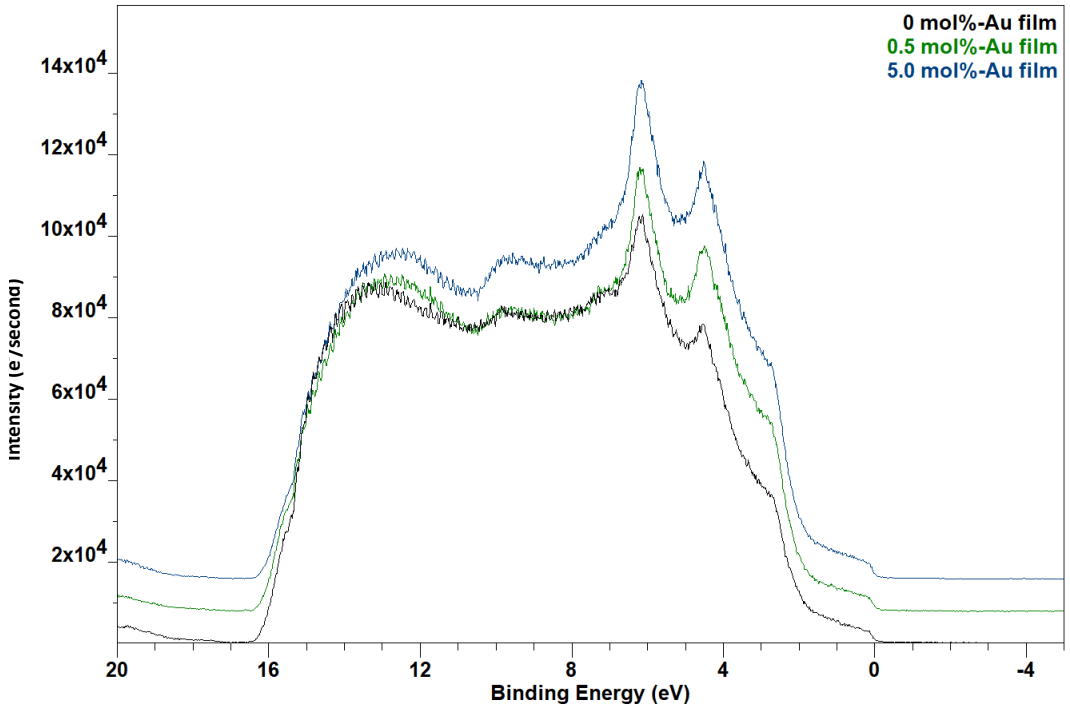

Figure 4.7-1. UPS spectra of the gold films deposited on top of 0 mol% (black), 0.5 mol% (green), and 5.0 mol% (blue) iron doped TiO_2.

Spectrum patterns for all gold films are the same. The feature at 0 eV clearly demonstrated the Fermi edge of gold. Data from 10 eV to 16 eV are associated with sample charging, due to the poor conductivity of the TiO_2 layer below the gold film. Such charging effect can be used to determine the work function of gold. By fitting the sharp edge near 16 eV, the secondary electron edge cut-off energy is determined to be 16.21 ± 0.02 eV (see Appendix, section 7.6.1). This result gives a work function of 5.01 ± 0.02 eV for gold, which matches the previously reported values for photoelectric work function measurement of 5.1 ± 0.1 eV[104].

Using the same samples, UPS spectra for TiO_2 with different iron doping percentages were collected, as shown in Figure 4.7-2 and the valence band spectra were determined.

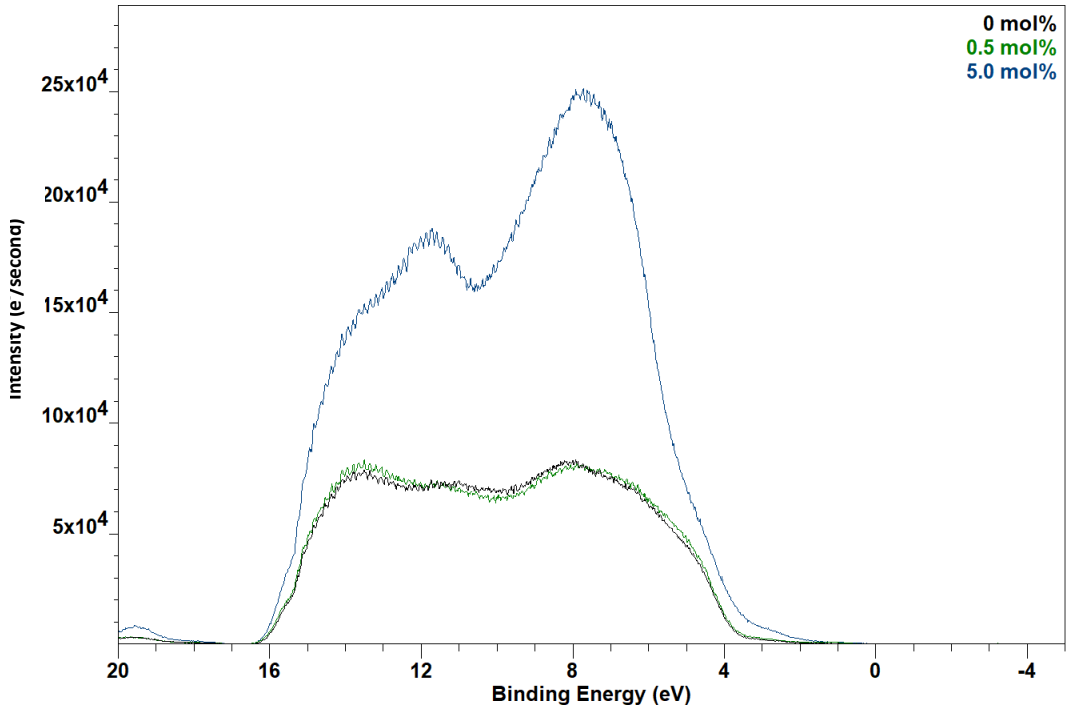

Figure 4.7-2. UPS spectra for 0 mol% (black), 0.5 mol% (green), and 5.0 mol% (blue) iron doped TiO_2 thin films.

From the obtained spectra, the charging peaks are observed from 10 eV to 16 eV, such that samples were suffering from charging effects. Thus, data may not represent the true valence band states of each sample. However, a comparative study can be conducted to see the influence of iron doping. Similar to XPS, there is a noticeable amount of valence

band maximum extension towards a lower binding energy near 4 eV. Applying the same approach for valence band maximum determination via XPS, the UPS valence band maximum positions for selected samples are determined to be 3.62 ± 0.07 eV, 3.60 ± 0.10 eV, and 3.42 ± 0.05 eV for samples of 0 mol%, 0.5 mol% and 5.0 mol% Fe doping, respectively (Appendix, section 7.6.2). Such result agrees with the XPS measurements, since the positions of valence band maximum decrease in binding energies due to iron doping, and the magnitude of the decrease are the same using both methods.

On the other hand, for samples with iron doping, the Fe 3d-O 2p orbital determined from XPS was at a lower binding energy position with respect to the bulk TiO_2 valence band. The presence of the iron-created band leads to the valence band edge extension towards a lower binding energy. Similar phenomena were captured in the UPS measurements as well. The main peak for all samples with Au depositions are located at around 8 eV, which is related to the valence band of anatase phase TiO_2. With higher doping levels, the right shoulders of the bulk valence band envelopes extended to a lower binding energy. This supports the sub-band creation due to iron doping by combining with our XPS results.

To see the true density of states in the valence band, UPS measurements were made without any metal coatings. For instance, the valence band structure of the 0 mol% doped TiO_2 sample without gold coating deposition on top is shown in Figure 4.7-3 a with the green solid line. Charging would change the overall valence band spectrum with shape distortions.

The inserted spectrum in Figure 4.7-3 b. is the valence band structure of anatase phase TiO_2 from Maheu and colleagues using UPS[67]. By comparing the spectra, the valence band structure from our measurement is similar to the spectrum by Maheu *et al* for the anatase phase TiO_2.

The valence band measurements of 0.5 mol% and 5.0 mol% doped TiO_2 using UPS are illustrated in Figure 4.7-4. In general, the charging effect created peaks at around 10 eV to 16 eV, in addition to the distortion of patterns from the sample itself. Besides, 0.5 mol% of iron doping brought minimal changes to its valence band, while 5 mol%

doping made drastic modifications, resulting in a different valence band pattern. The width of the valence band was narrowed due to a higher iron doping. The uncharged valence band spectra collected could reveal the true states, however, these spectra cannot be used for the determination of the valence band maximum positions due to the lack of binding energy references.

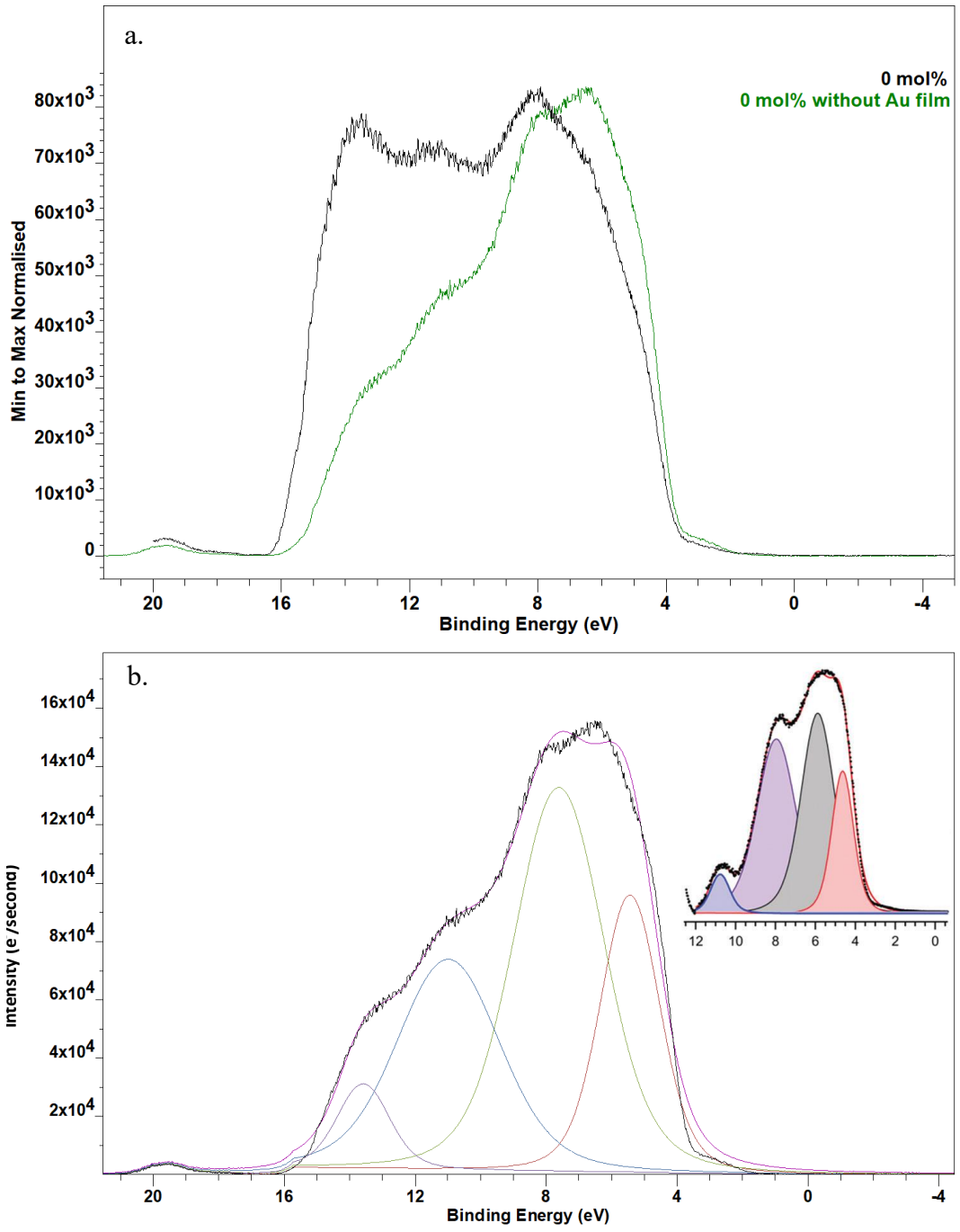

Figure 4.7-3. UPS spectra of a. 0 mol% Fe doped TiO_2 with (black) and without (green) Au coatings, and b. the components for the uncharged 0 mol% TiO_2 after fitting. Inset picture in b. is the He I UP spectra of anatase/ITO from Maheu *et al*. Reproduced from Ref. [68] with permission from the Royal Society of Chemistry.

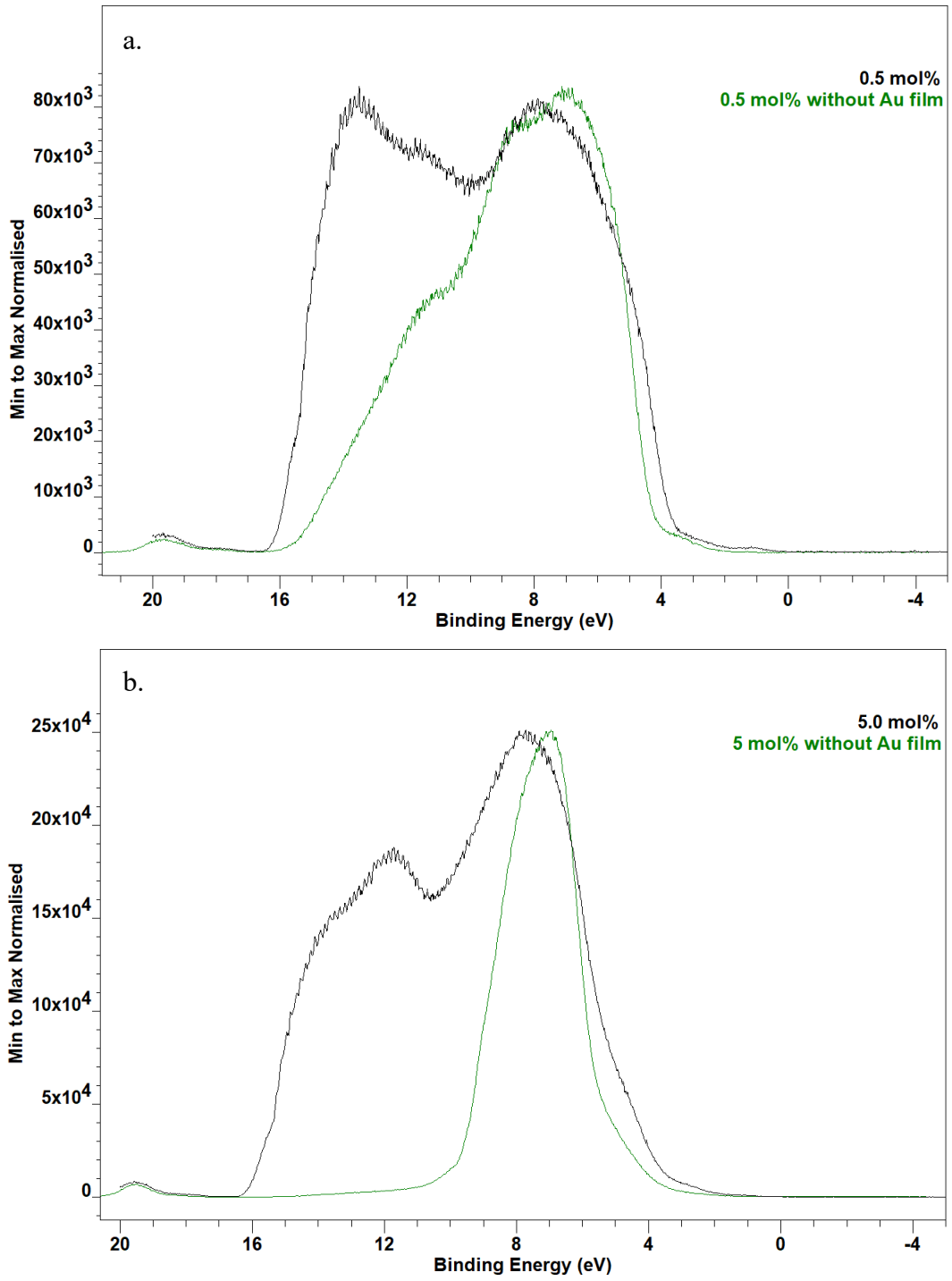

Figure 4.7-4. Valence band spectra of a. 0.5 mol%, and b. 5.0 mol% iron doped TiO_2, with (black) and without (green) Au coatings.

4.8 Band diagram of Fe doped TiO_2

From previous chapters, the valence band maximum positions, the absolute position of the valence band, and the band gap values are experimentally characterized using XPS, UPS, and UV-Vis DRS. By combining these results, we can compute the band diagram of TiO_2 with various iron doping levels. A summary of UV-Vis DRS, XPS, and UPS results for our samples related to the band structure measurements are given in Table 4.8-1.

Table 4.8-1. Summary of UV-Vis DRS, XPS, and UPS results of measured samples.

Fe doping level (mol%)	UV-Vis DRS direct band gap (eV)	UV-Vis DRS indirect band gap (eV)	XPS valence band maximum (eV)	UPS valence band maximum (eV)
0	3.44 ± 0.20	3.24 ± 0.06	2.52 ± 0.29	3.62 ± 0.07
0.5	3.41 ± 0.24	3.14 ± 0.08	2.50 ± 0.34	3.60 ± 0.10
2.0	3.35 ± 0.36	2.99 ± 0.16	2.39 ± 0.23	N/A
5.0	2.85 ± 0.10	2.22 ± 0.02	2.17 ± 0.32	3.42 ± 0.05

4.8.1 UV-Vis DRS and XPS combined band diagram

Our previous results on UV-Vis DRS showed the band gap values between the valence band maximum and the conduction band maximum for 0 mol%, 0.5 mol%, 2.0 mol%, and the 5 mol% iron doped TiO_2 nanoparticles. The position and pattern of the valence band were measured using XPS. Even though the conduction band is not learnt yet, a relative position can be deduced from the existing evidence. By referencing to the same Fermi level, the band diagrams for all measured samples are shown in Figure 4.8-1.

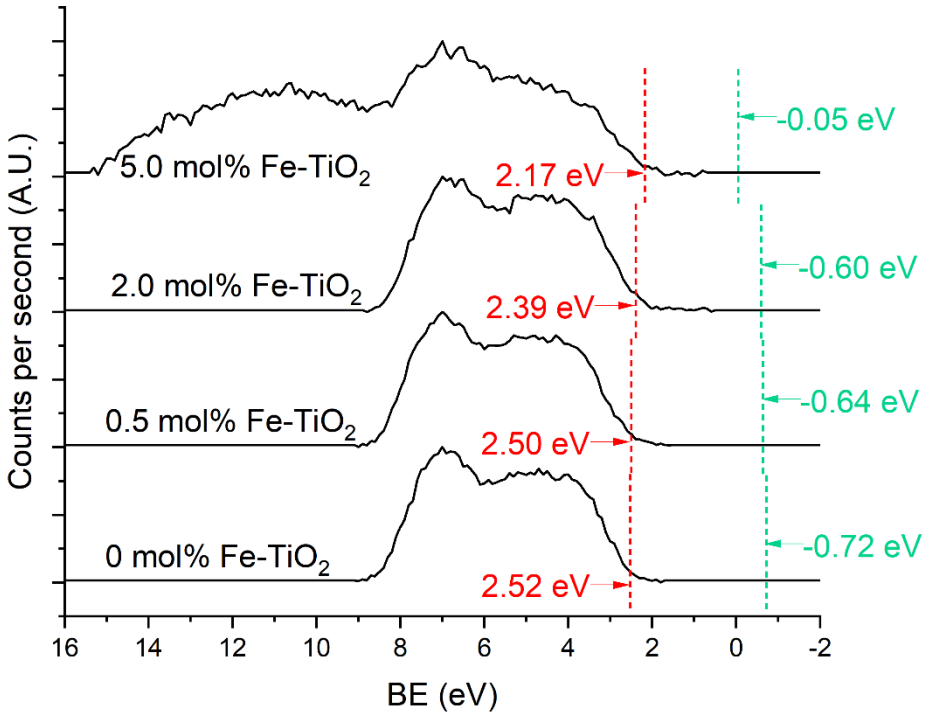

Figure 4.8-1. UV-Vis DRS and XPS combined band diagram. The solid black lines are the valence band structures determined by low energy XPS. The red dashed lines are the valence band maximum positions from fitting, and the greens are the positions of the conduction band minima, deduced from indirect band gaps measured by UV-Vis DRS.

Despite the modifications on the valence band structures, it is worth to note that, the

conduction band minima from the indirect band gaps are at -0.72 eV, -0.64 eV, -0.60 eV, and -0.05 eV, for sample containing 0 mol%, 0.5 mol%, 2.0 mol%, and 5.0 mol% Fe, respectively. This is consistent with our theoretical analysis for *n*-type doping, where the Fe dopant would modify the conduction band structure significantly via sub-band creation. Because of doping, the sub band created by Fe^{3+} would bring the conduction band minimum towards its valence band, such that the band gap is narrowed. In addition, the charge transfer from Fe^{3+} to Fe^{2+} could also contribute to the conduction band modification with additional sub bands, which will need inverse photoelectron characterizations to further verify.

Reasons that lead to uncertainties in the band diagrams could be of several origins. First, the 5.0 mol% sample charging from XPS measurements, associated with peaks from 10 eV to 15 eV, would affect its valence band structure. In this case, it could shift the position of the deduced conduction band. Another possibility could be due to the band gap measurement from UV-Vis DRS. XRD measurements showed that there is 5 wt.% of Fe_2O_3 crystallites in the 5.0 mol% powder. Studies have characterized that the direct band gap for Fe_2O_3 is around 2.67 eV, and the indirect band gap are in range of 1.6 to 1.94 eV depending on the annealing temperature[105]. As those values are smaller compared to the measured band gaps of the iron doped titania, it is possible for Fe_2O_3 to affect the overall band gap by lowering its value, which would bring the conduction band closer to the valence band using our approach. This statement is supported by other studies, that the band gap of TiO_2/Fe_2O_3 mixture was narrowed when the amount of Fe_2O_3 increased, and the band gap values of all mixtures lied in between that of TiO_2 and Fe_2O_3 individually[106,107].

4.8.2 UV-Vis DRS and UPS combined band diagram

Using a similar approach, the band diagram of the measured TiO_2 samples can be demonstrated using UV-Vis DRS and UPS as well. By using UPS results, it could reveal the electron orbitals closer to the reality, as well as the absolute po10sition of orbitals in the valence band region.

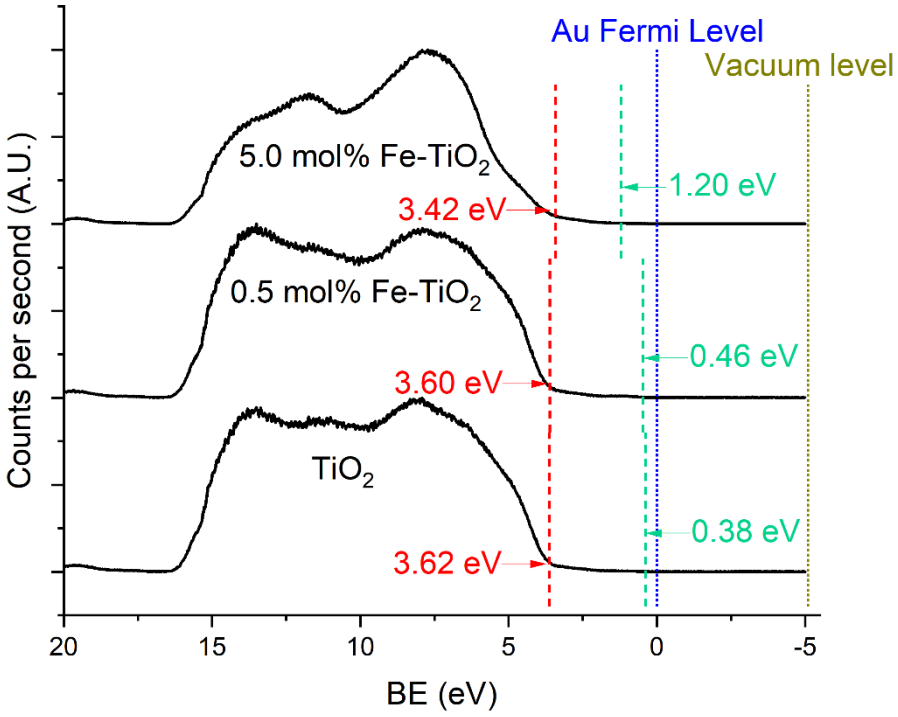

Figure 4.8-2. UV-Vis DRS and UPS combined band diagram. From left to right are 0 mol%, 0.5 mol%, and 5.0 mol% Fe doped TiO_2 samples, respectively. The solid black lines are the valence band structured determined by UPS with respect to the Fermi level of gold at 0 eV in blue dashed lines. The brown dashed line is the vacuum level at -5.1 eV determined using the measured work function. The dashed greens correspond to the conduction band minima, deduced using indirect band gaps measured by UV-Vis DRS.

The band diagram in Figure 4.8-2 utilizes the work function of gold to determine the absolute position of gold's Fermi level with respect to the vacuum. The valence band

spectra of all measured samples are calibrated using such Fermi level, therefore their band structures can be constructed in a same manner as previously demonstrated using XPS and UV-Vis DRS.

Using the proposed model, the conduction band minima for 0 mol%, 0.5 mol% and 5.0 mol% samples are located at 0.38 eV, 0.46 eV, and 1.20 eV with respect to the Fermi level of gold. The absolute positions of the conduction band of TiO_2 are shifted towards the valence band with higher doping levels. This is consistent with our UV-Vis DRS and XPS combined model, such that the band gap narrowing is mainly from the sub band arising from Fe^{3+} doping. As for the decrease of the conduction band maxima, XPS and UPS results both showed that doping with 0.5 mol% shifted the conduction band towards the valence band by 0.08 eV, while that value is increased to 0.82 eV and 0.67 eV with 5.0 mol% Fe doping detected by UPS and XPS, respectively. These values agree with each other within uncertainties, in other words, our proposed models describe the properties of our materials well.

The errors in this model are similar to the XPS and UV-Vis DRS combined one. First, all samples suffered from various charging issue. The undoped and 0.5 mol% iron doped samples had similar charging effect due to their low conductivity, as seen in Figure 4.7-2 (section 4.7). Doping with 5 mol% of iron increased the conductivity of the sample, which gives smaller the charging components. Such difference could cause the apparent shifting of the valence band, resulting in inaccurate measurements. Second, UPS is extremely surface sensitive. 13 wt.% of brookite phase TiO_2 and 5 wt.% of Fe_2O_3 were detected in the 5.0 mol% sample through XRD, and these compositions could affect the valence band structure, especially the valence band maximum position. Third, as previously mentioned (see section 4.8.1), the presence of small amounts of brookite/Fe_2O_3 in the anatase phase may provide a smaller band gap values when UV-Vis DRS is used.

To see more clearly on the conduction band, low energy inverse photoemission spectroscopy can be used to characterize the conduction band structure. Thus, further

measurements would help to investigate how doping with iron changes the conduction band of anatase phase TiO_2.

Therefore, based on experimental results, the proposed models can reasonably illustrate the real band structures of anatase TiO_2 with various iron doping percentages; however, it can be improved with data of higher accuracies by eliminating brookite/Fe_2O_3 contents in the powder during synthesis, as well as the charging effect during XPS/UPS measurements.

4.9 Role of iron dopants in methylene blue photodegradation

Experimental results in this study showed the valence band structure of TiO_2 extended towards a lower binding energy using iron as the dopants. Band gaps measured by UV-Vis DRS demonstrated the forbidden gap shrinking effect due to iron doping, such that longer wavelengths can be absorbed. Such effect leads to a higher efficiency in OH radical generation from the same light source, resulting in a faster decomposition process.

In addition, both XPS and UPS results support the sub-band creation due to Fe^{3+}. The band created when doping with iron can act as a trapping site for electrons during the electron-hole recombination process, such that it would take longer time for these charge carriers to reform into photons. It is known as the defect-assisted recombination process, and the rate of recombination is lowered compared to the band to band recombination without dopant-created defects[108,109]. Thus, because of doping, electrons have higher chances to complete OH radical generation via the indirect mechanism. However, higher iron contents would make the doped TiO_2 more conductive, resulting in a shorter travelling time of photo-created charge carriers. In this case, the recombination rate is increased, which will slow down the OH radical production. Therefore, our results suggest that there would exist an optimal doping level to achieve the best photodegradation rate using Fe-TiO_2 nanoparticles.

On the other hand, iron doping would also affect the morphological properties of the synthesized nanoparticles. From the photocatalysis mechanism, the OH radical generation occurs on the surface of nanoparticles, such that larger reaction area would guarantee a higher reaction rate. From the SEM images and the estimated size distributions of the synthesized samples, results showed that higher iron doping levels, up to 2.0 mol%, provided smaller sized nanoparticles using the same sol-gel process. Increasing the iron loading from 2.0 mol% to 5.0 mol% did not affect much the average particle sizes (from 16.1 ± 2.4 nm to 16.6 ± 2.6 nm, respectively). Therefore, if the synthesized powder is used as photocatalysts without further treatments, powders with lower iron doping percentages would have less total surface area under the same mass, resulting in a lowered photodecomposition rate.

However, if all synthesized materials can achieve a similar size via milling, XRD evidence showed that larger average crystallite sizes belonged to higher iron doping percentages, with the lightly to undoped samples being the smallest. Crystallite size effect to the total surface area can be explained microscopically using an example of isolated nanoparticle without agglomerates. Instead of existing as agglomerates, if each of the obtained nanoparticles are made up of single crystallites, those with larger crystallites, i.e., higher iron concentrations, would have less surface area than that made of smaller crystallite, i.e., undoped TiO_2. In this scenario, the photocatalysis rate would be decreased theoretically using the same weight of ideal nanoparticles.

Moreover, TiO_2 with higher iron contents inside are heavier, such that the total surface area decreases due to a reduced number of particles under a certain mass. Thus, by summarizing all morphological aspects, it again infers that there should be an optimal iron doping level to achieve the best photodegradation performance.

In conclusion, after considering both the electronic and morphological properties of TiO_2 nanomaterials, characterization results from our current study support the existence of an optimal iron doping level to maximize the indirect photodegradation reaction using doped TiO_2 nanoparticles.

5 Future work

The current work demonstrated the electronic band structure of TiO_2 nanoparticles through experimental methods, as well as analyzed the effect of iron doping on morphological and electronic properties. Evidence based on our results support that TiO_2 with iron doping at a certain level could potentially enhance the overall photodegradation rate of a dye, such as methylene blue. To test this hypothesis, dye decomposition experiments should be performed. Using light sources of different wavelengths, the photodegradation rate using catalyst of various iron doping percentages can be obtained experimentally. At the same time, the relation between iron doping level and the overall photodecomposition rate can be determined systematically.

Also, measurements of the conduction band structure would reveal more information of the effects of iron doping in these materials. Using inverse photoelectron spectroscopy, the unoccupied electron orbitals can be detected to construct the density of electrons in the conduction band region. In this case, the whole band structure can be experimentally determined to improve the proposed band diagrams.

Additionally, it will be helpful to measure the recombination rate of the nanomaterial with respect to experimental parameters, such as iron doping percentages, electrical conductivity, pH during decomposition, dye concentration, etc. Measurements such as photoluminescence can be applied to measure the spontaneous radiative recombination process. This will provide additional information to quantify influences due to the described aspects, and the photodegradation rate can be further related using the experimental data.

Meanwhile, measurements of the powder's specific surface area would help to explain the relation between iron doping level and the rate of dye decomposition as well. Powders with smoother surfaces result in larger specific surface area. New specific surface area measurements can be combined with the existed XRD estimations to quantify the amount of active surface area during photodegradation experiments. By

using catalyst of equal mass, samples with higher specific surface area guarantee higher photodegradation rates. Therefore, increasing effective reaction area may counterbalance the enhancement from electronic modifications by iron doping. If powders of the same total surface area are used instead, the function of iron modification on the electronic band structure can be quantified in future studies.

Furthermore, to investigate more accurately iron doping modifications to anatase TiO_2, the synthesis procedure for higher iron doping levels can be improved to suppress the formation of brookite phase TiO_2 as well as Fe_2O_3. Better milling technique, such as ball milling, can also be applied to yield powders of individual nanoparticles instead of aggregates.

Lastly, improvements can be made to XPS and UPS measurements. Current UPS results suffered from charging effects, due to the poor conductivity of the sample. To solve this, samples could be deposited on a more conductive substrate, such as a metal sample. The type of substrate should be considered thoroughly, as some of the metal may interact with the sample. High quality noble metals, such as silver, gold, and platinum, are promising substrate materials. However, the film deposition method should be adjusted accordingly to achieve a proper thickness, since charging effects could rise using thicker films, while substrate signals would interfere with the results using thinner ones.

6 Conclusion

TiO_2 nanoparticles with theoretically 0 mol%, 0.5 mol%, 1.5 mol%, and 5 mol% of iron doping were successfully synthesized via sol-gel method. Elemental analysis by EDX and XPS agreed with the theoretical iron doping levels for most samples, and the actual doping percentage of 1.5 mol% was corrected to 2.0 mol%.

XRD analysis demonstrated both 0 mol% and 0.5 mol% Fe-doped TiO_2 nanoparticles were of pure anatase phase, whereas 11 wt.% and 13 wt.% of brookite phase were formed using higher iron doping levels of 2.0 mol% and 5.0 mol%, respectively. Crystallite size analysis using Scherrer equation after Rietveld refinement showed the average crystallite size of 0 mol%, 0.5 mol%, 2.0 mol%, and 5.0 mol% Fe-doped TiO_2 under the same preparation condition were 10.7 nm, 10.3 nm, 12.0 nm, and 13.0 nm, respectively. Crystallites grew larger with higher levels of iron doping. Calcination at a lower temperature with higher TTIP:H_2O ratio resulted in even smaller crystallites.

SEM measurements revealed the morphology of the synthesized materials, with all samples displaying a similar spherical shape for the nanoparticles on the surface of the formed aggregates. Particle size estimations using the SEM images gave an average particle size of 47.2 nm to 62.3 nm, 51.6 nm to 63.2nm, 16.6 nm, and 16.1 nm in diameters for samples with 0 mol%, 0.5 mol%, 2.0 mol%, and 5.0 mol% iron doping percentages, respectively.

Band gap measurements via UV-Vis DRS confirmed the band narrowing effect by the iron dopants. Direct band gap values determined by Kubelka-Munk function were 3.44 ± 0.20 eV, 3.41 ± 0.24 eV, 3.35 ± 0.36 eV, and 2.85 ± 0.10 eV, with the indirect band gaps of 3.24 ± 0.06 eV, 3.14 ± 0.08 eV, 2.99 ± 0.16 eV, and 2.22 ± 0.02 eV for samples of 0 mol%, 0.5 mol%, 2.0 mol%, and 5.0 mol% iron doping, respectively.

Spectra from XPS and UPS lead to the sub-band creation by iron dopants near the valence band of anatase phase TiO_2, resulting in band edge extension towards lower

binding energies. Band structure models determined experimentally by XPS, UPS, and UV-Vis DRS further illustrated the modification due to the iron dopant on the band structure of anatase TiO_2. These models and results were then used to analyze the theoretical enhancement to photocatalysis rate of methylene blue solutions.

By considering both the morphologic and electronic modifications, our study suggests that there would exist an optimal iron doping percentage to maximize the photodegradation process under a specific illumination wavelength. Such doping percentage can be determined via photodegradation experiments in future studies.

7 Appendix

7.1 Appendix A: Powder X-Ray Diffraction analysis

7.1.1 0 mol% and 0.5 mol% Fe-doped TiO_2 nanoparticles

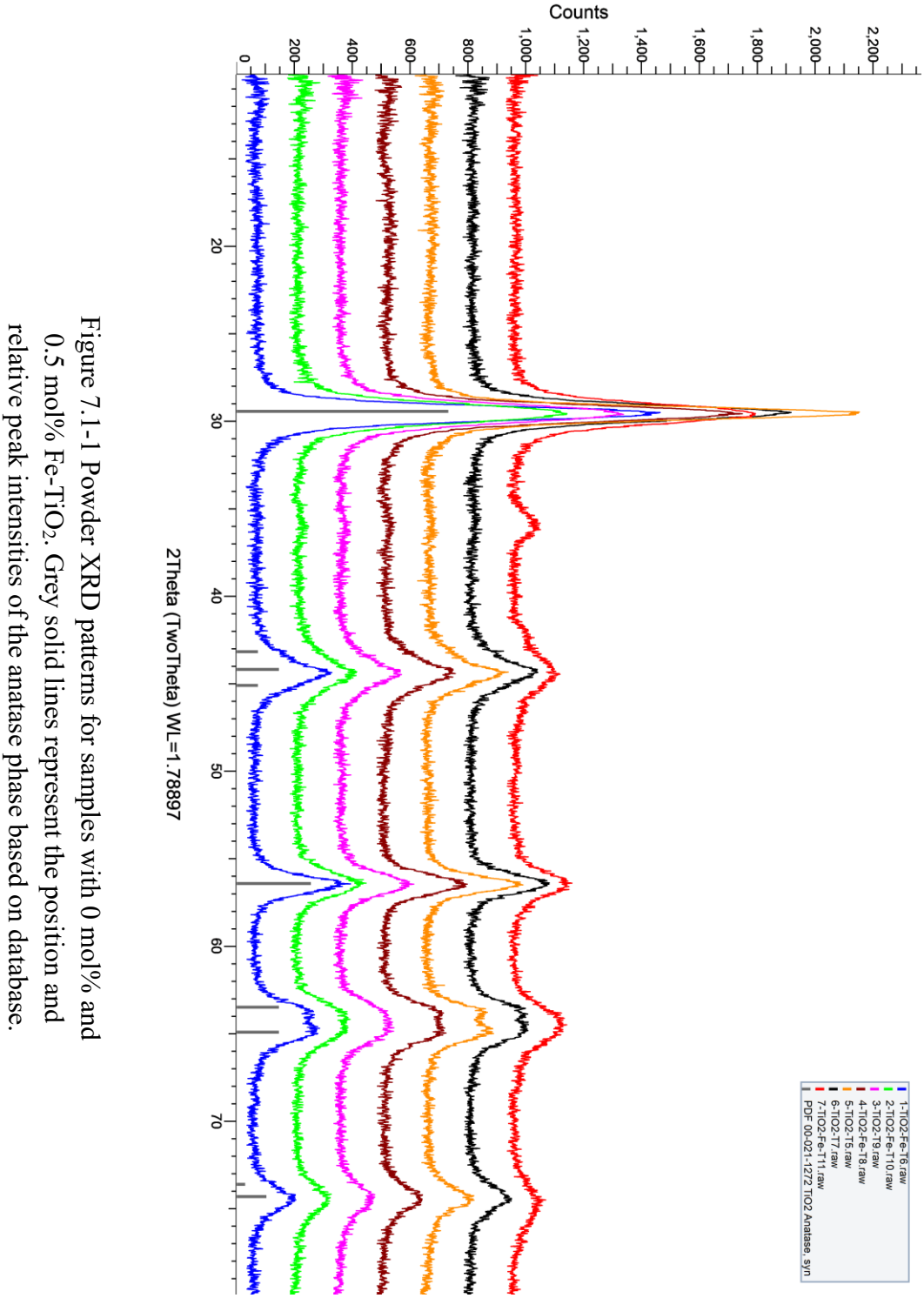

Figure 7.1-1 Powder XRD patterns for samples with 0 mol% and 0.5 mol% Fe-TiO_2. Grey solid lines represent the position and relative peak intensities of the anatase phase based on database.

Table 7.1-1 Powder XRD pattern analysis results for 0 mol% and 0.5 mol% Fe-TiO_2.

Pattern: PDF 00-021-1272 Radiation: 1.78897 Quality: Star (*)

Formula	TiO2
Name	Titanium Oxide
Name (mineral)	Anatase, syn
Name (common)	
Status	Primary
Ambient	Yes

Lattice:	Tetragonal	**Mol. weight =**	79.86
S.G.:	I41/amd (141)	**Volume [CD] =**	136.31
		Dx =	
		Dm =	
		I/Icor =	3.300

a =	3.78520		
c =	9.51390		
a/b =	1.00000	**Z =**	4
c/b =	2.51345		

Additional Patterns: See PDF 01-071-1166. Validated by calculated pattern
General Comments: Anatase and another polymorph, brookite (orthorhombic), are converted to rutile (tetragonal) by heating above 700 C. Pattern reviewed by Holzer, J., McCarthy, G., North Dakota State Univ, Fargo, North Dakota, USA, ICDD Grant-in-Aid (1990). Agrees well with experimental and calculated patterns
Sample Source or Locality: Sample obtained from National Lead Co., South Amboy, New Jersey, USA
Temperature of Data Collection: 298 K
Unit Cell Data Source: Powder Diffraction

Primary Reference
Publication: Natl. Bur. Stand. (U. S.) Monogr. 25
Detail: volume 7, page 82 (1969)

Wavelength:	1.78897	**Filter:**	Not specified
SS/FOM:	F(30)= 74.2 (0.0116, 35)	**d-spacing:**	

d	2θ	I fix	h	k	l
3.52000	29.442	100	1	0	1
2.43100	43.178	10	1	0	3
2.37800	44.191	20	0	0	4
2.33200	45.110	10	1	1	2
1.89200	56.429	35	2	0	0
1.69990	63.498	20	1	0	5
1.66650	64.925	20	2	1	1
1.49300	73.614	4	2	1	3
1.48080	74.322	14	2	0	4
1.36410	81.950	6	1	1	6
1.33780	83.922	6	2	2	0
1.27950	88.708	2	1	0	7
1.26490	90.008	10	2	1	5
1.25090	91.298	4	3	0	1
1.18940	97.536	2	0	0	8
1.17250	99.439	2	3	0	3
1.16640	100.148	6	2	2	4
1.16080	100.811	4	3	1	2
1.06000	115.099	2	2	1	7
1.05170	116.535	4	3	0	5
1.04360	117.988	4	3	2	1
1.01820	122.923	2	1	0	9
1.00700	125.313	2	2	0	8
0.99670	127.649	2	3	2	3
0.95550	138.827	4	3	1	6
0.94640	141.869	4	4	0	0
0.92460	150.673	2	3	0	7
0.91920	153.367	2	3	2	5
0.91380	156.398	2	4	1	1
0.89660	172.127	4	2	1	9

7.1.2 2.0 mol% Fe-doped TiO_2 nanoparticles

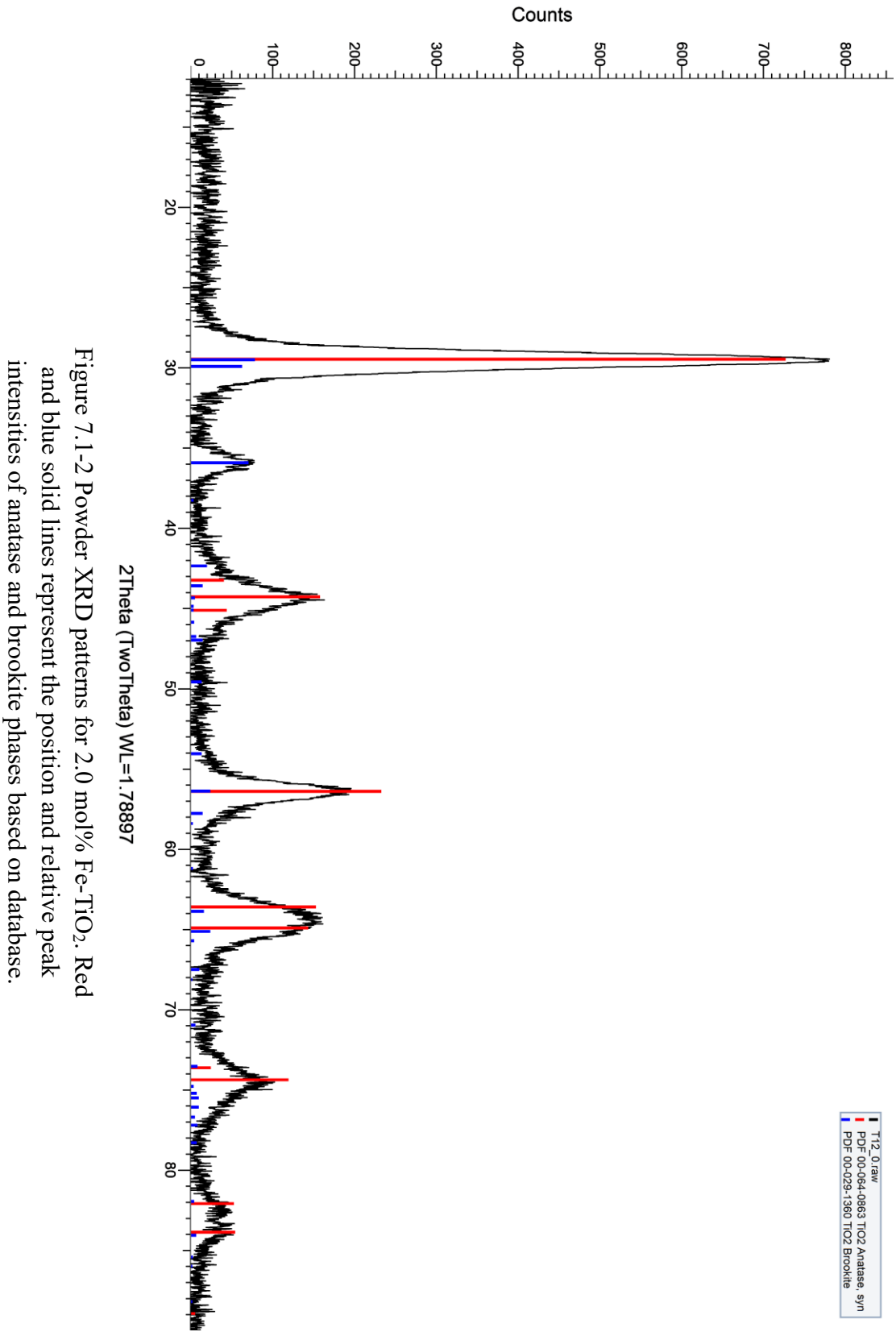

Figure 7.1-2 Powder XRD patterns for 2.0 mol% Fe-TiO_2. Red and blue solid lines represent the position and relative peak intensities of anatase and brookite phases based on database.

Table 7.1-2 Powder XRD pattern analysis results for anatase phase in 2.0 mol% Fe-TiO_2.

Pattern: PDF 00-064-0863 Radiation: 1.78897 Quality: Star (*)

Formula	TiO2
Name	Titanium oxide
Name (mineral)	Anatase, syn
Name (common)	anatase, nano
Status	Primary
Ambient	Yes

Lattice:	Tetragonal	**Mol. weight =**	79.86
S.G.:	I41/amd (141)	**Volume [CD] =**	136.03
		Dx =	3.899
		Dm =	
		I/Icor =	5.010

a =	3.78536		
c =	9.49360		
a/b =	1.00000	**Z =**	4
c/b =	2.50798		

Powder Data: Broad peaks resulting from nano-sized particles
Physical property: Nano-powder
Sample Preparation: Prepared by mixing hexanoic acid, titanium(IV) butoxide, 1-butanol and deionized water in a glass insert of a stainless steel pressure reactor and stirring for 30 minutes at room temperature. The temperature was increased to 508 K in 1 hour and the mixture was stirred for an additional 5 hours. After cooling, the precipitate was isolated by centrifugation and washed with hexane before the final solid was dried in ambient air overnight
Calculated Pattern Original Remarks: Original Max Intensity 999.0 < 1000.0

Primary Reference
Publication: Private Communication
Authors: Blanton, T., Eastman Kodak Co., Rochester, NY, USA.

Radiation:	CuKα1	**Filter:**	Not specified
Wavelength:	1.78897	**d-spacing:**	
SS/FOM:	F(30)= 999.9 (0.0002, 34)		

d	2θ	I fix	h	k	l
3.51616	29.475	999	1	0	1
2.42788	43.237	55	1	0	3
2.37339	44.281	217	0	0	4
2.33152	45.120	60	1	1	2
1.89268	56.407	320	2	0	0
1.69718	63.612	210	1	0	5
1.66658	64.921	197	2	1	1
1.49270	73.631	33	2	1	3
1.47977	74.382	164	2	0	4
1.36208	82.098	72	1	1	6
1.33833	83.881	74	2	2	0
1.27675	88.950	7	1	0	7
1.26357	90.129	118	2	1	5
1.25079	91.309	37	3	0	1
1.18670	97.834	7	0	0	8
1.17205	99.491	10	3	0	3
1.16576	100.224	64	2	2	4
1.16070	100.823	27	3	1	2
1.05844	115.365	8	2	1	7
1.05090	116.676	34	3	0	5
1.04351	118.005	35	3	2	1
1.01613	123.354	27	1	0	9
1.00541	125.664	17	2	0	8
0.99646	127.705	12	3	2	3
0.95463	139.106	49	3	1	6
0.94634	141.890	30	4	0	0
0.92380	151.055	4	3	0	7
0.91877	153.594	53	3	2	5
0.91382	156.386	35	4	1	1
0.89526	175.232	46	2	1	9
0.89474	177.264	54	1	1	10

Table 7.1-3 Powder XRD pattern analysis results for brookite phase in 2.0 mol% Fe-TiO_2.

Pattern: PDF 00-029-1360 Radiation: 1.78897 Quality: Star (*)

Formula	TiO2
Name	Titanium Oxide
Name (mineral)	Brookite
Name (common)	
Status	Primary
Ambient	Yes

Lattice:	Orthorhombic
S.G.:	Pcab (61)

Mol. weight =	79.86
Volume [CD] =	257.63
Dx =	
Dm =	4.14
I/Icor =	-1.000

a =	5.45580
b =	9.18190
c =	5.14290
a/b =	0.59419
c/b =	0.56011
Z =	8

Additional Patterns: To replace 00-016-0617 and validated by calculated pattern. See PDF 01-076-1934
Analysis: Spectrographic analysis: 0.1-1.0% Si; 0.01-0.1% each of Al, Fe, and V; 0.001-0.01% Mg. Niobian brookite from Mozambique (Chemical analysis (wt %): "Ti O2" 80.7, "Nb2 O5" 14.1, FeO 5.53); Carvalho et al., Rev. Cien. Geol. Ser. A, 7 61 (1974) reports an identical pattern
General Comments: Intensities verified by calculated pattern
Sample Source or Locality: Specimen from Magnet Cove, Arkansas, USA (USNM 97661)
Temperature of Data Collection: 298 K
Unit Cell Data Source: Powder Diffraction

Primary Reference
Publication: Dana's System of Mineralogy, 7th Ed.
Detail: volume I, page 588 (1944)
Publication: Natl. Bur. Stand. (U. S.) Monogr. 25
Detail: volume 3, page 57 (1964)

Radiation:	CuKα1
Wavelength:	1.78897
SS/FOM:	F(30)= 57.5 (0.0116, 45)
Filter:	F
d-spacing:	

d	2θ	I fix	h	k	l
3.51200	29.511	100	1	2	0
3.46500	29.920	81	1	1	1
2.90000	35.931	90	1	2	1
2.72900	38.267	4	2	0	0
2.47600	42.355	25	0	1	2
2.40900	43.593	18	2	0	1
2.37000	44.348	6	1	3	1
2.34400	44.866	4	2	2	0
2.33200	45.110	4	2	1	1
2.29600	45.857	6	0	4	0
2.25400	46.762	8	1	1	2
2.24400	46.983	18	0	2	2
2.13300	49.588	16	2	2	1
1.96850	54.053	16	0	3	2
1.89340	56.383	30	2	3	1
1.85140	57.781	18	1	3	2
1.83320	58.410	3	2	1	2
1.75680	61.215	3	2	4	0
1.69080	63.880	21	3	2	0
1.66170	65.135	30	2	4	1
1.64860	65.718	6	1	5	1
1.60980	67.511	13	1	1	3
1.59680	68.136	2	2	3	2
1.54080	70.976	7	1	2	3
1.49420	73.545	11	0	5	2
1.47290	74.788	4	1	6	0
1.46560	75.225	9	3	1	2
1.46090	75.510	12	2	5	1
1.45150	76.085	12	2	0	3
1.44150	76.709	6	1	3	3
1.43360	77.209	11	2	1	3
1.41670	78.305	9	1	6	1
1.36400	81.958	6	4	0	0
1.33580	84.076	8	3	3	2
1.31860	85.431	3	4	0	1
1.31160	85.997	2	2	3	3
1.28520	88.212	2	0	0	4
1.23810	92.517	11	0	2	4
1.21070	95.261	2	4	3	1
1.20740	95.605	1	1	2	4
1.15520	101.485	4	3	3	3
1.14800	102.369	2	0	8	0
1.14320	102.969	2	4	4	1
1.12170	105.772	4	0	4	4
1.03990	118.670	3	5	2	1
1.03990	118.670	3	4	2	3

7.1.3 5.0 mol% Fe-doped TiO_2 nanoparticles

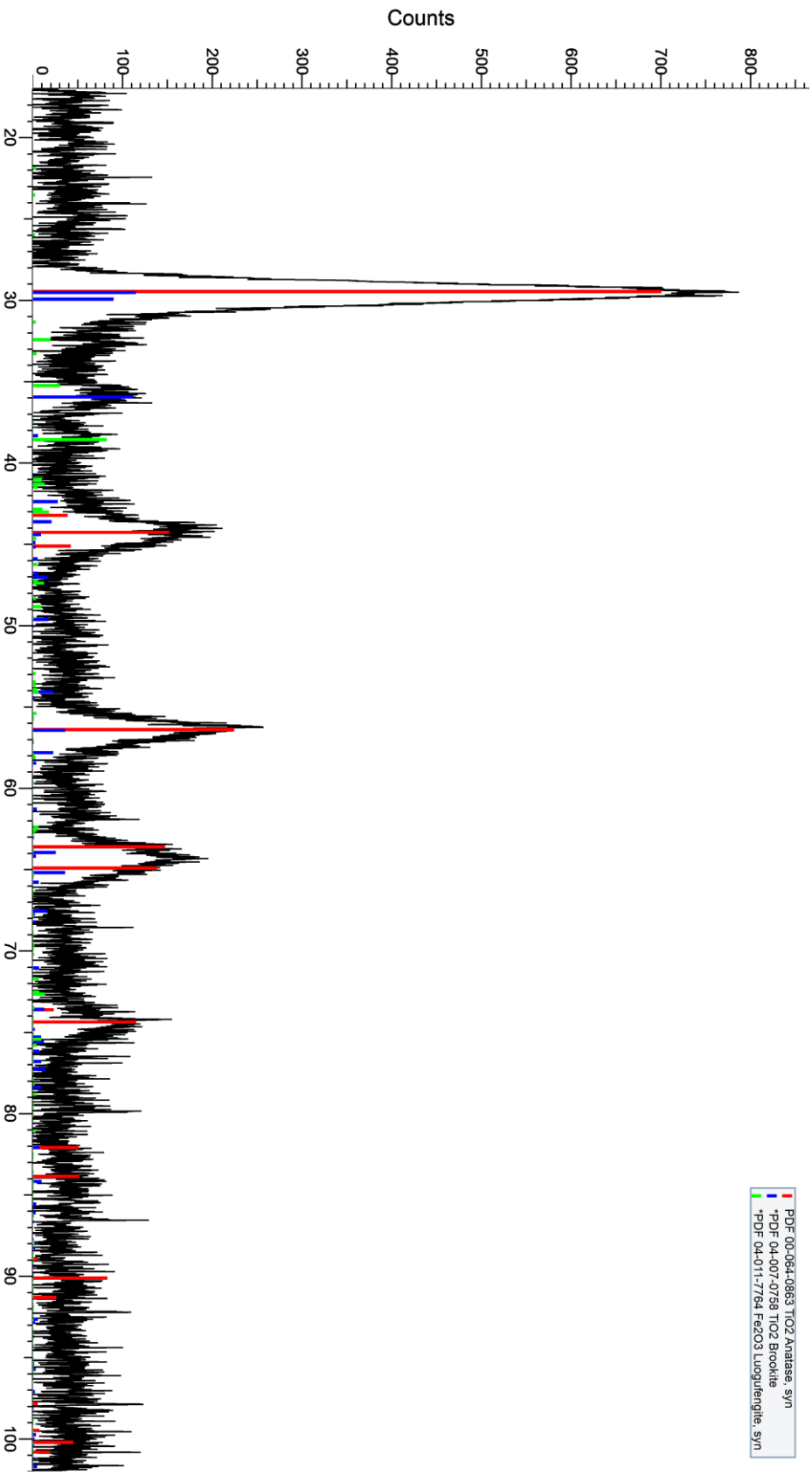

Figure 7.1-3 Powder XRD patterns for 5.0 mol% Fe-TiO_2. Red, blue, and green solid lines represent the position and relative peak intensities of the anatase, brookite, and Fe_2O_3 based on database.

Table 7.1-4 Powder XRD pattern analysis results for anatase phase in 5.0 mol% Fe-TiO_2.

Pattern: PDF 00-064-0863 Radiation: 1.78897 Quality: Star (*)

Formula	TiO2
Name	Titanium oxide
Name (mineral)	Anatase, syn
Name (common)	anatase, nano
Status	Primary
Ambient	Yes

Lattice:	Tetragonal	**Mol. weight =**	79.87
S.G.:	I41/amd (141)	**Volume [CD] =**	136.033
		Dx =	3.899
		Dm =	
		I/Icor =	5.010

a =	3.78536		
c =	9.49360		
a/b =	1.00000	**Z =**	4
c/b =	2.50798		

Physical property: Nano-powder
Sample Preparation: Prepared by mixing hexanoic acid, titanium(IV) butoxide, 1-butanol and deionized water in a glass insert of a stainless steel pressure reactor and stirring for 30 minutes at room temperature. The temperature was increased to 508 K in 1 hour and the mixture was stirred for an additional 5 hours. After cooling, the precipitate was isolated by centrifugation and washed with hexane before the final solid was dried in ambient air overnight
Raw Data Comment: Broad peaks resulting from nano-sized particles
Calculated Pattern Original Remarks: Original Max Intensity 999.0 < 1000.0

Radiation:	CuK±1	**Filter:**	Not specified
Wavelength:	1.78897	**d-spacing:**	
SS/FOM:	F(30)= 999.9 (0.0002, 34)		

d	2θ	I fix	h	k	l
3.51616	29.475	999	1	0	1
2.42788	43.237	55	1	0	3
2.37339	44.281	217	0	0	4
2.33152	45.120	60	1	1	2
1.89268	56.407	320	2	0	0
1.69718	63.612	210	1	0	5
1.66658	64.921	197	2	1	1
1.49270	73.631	33	2	1	3
1.47977	74.382	164	2	0	4
1.36208	82.098	72	1	1	6
1.33833	83.881	74	2	2	0
1.27675	88.950	7	1	0	7
1.26357	90.129	118	2	1	5
1.25079	91.309	37	3	0	1
1.18670	97.834	7	0	0	8
1.17205	99.491	10	3	0	3
1.16576	100.224	64	2	2	4
1.16070	100.823	27	3	1	2
1.05844	115.365	8	2	1	7
1.05090	116.676	34	3	0	5
1.04351	118.005	35	3	2	1
1.01613	123.354	27	1	0	9
1.00541	125.664	17	2	0	8
0.99646	127.705	12	3	2	3
0.95463	139.106	49	3	1	6
0.94634	141.890	30	4	0	0
0.92380	151.055	4	3	0	7
0.91877	153.594	53	3	2	5
0.91382	156.386	35	4	1	1
0.89526	175.232	46	2	1	9
0.89474	177.264	54	1	1	10

Table 7.1-5 Powder XRD pattern analysis results for brookite phase in 5.0 mol% Fe-TiO_2.

Pattern: PDF 04-007-0758 Radiation: 1.78897 Quality: Star (*)

Formula	TiO2
Name	Titanium Oxide
Name (mineral)	Brookite
Name (common)	titanium dioxide
Status	Primary
Ambient	Yes

Lattice:	Orthorhombic	**Mol. weight =**	79.86
S.G.:	Pbca (61)	**Volume [CD] =**	256.84
		Dx =	4.13
		Dm =	
		I/Icor =	1.630

a =	9.17400		
b =	5.44900		
c =	5.13800		
a/b =	1.68361	**Z =**	8
c/b =	0.94293		

ANX: AX2
General Comments: brookite
LPF Collection Code: 1250448
Sample Source or Locality: Binntal, Switzerland
Temperature Factor: Reported Anisotropic temperature factors (in Beta) were converted to B

Radiation:	CuK±1	**Filter:**	Not specified
Wavelength:	1.78897	**d-spacing:**	
SS/FOM:	F(30)= 999.9 (0.0000, 30)		

d	2θ	I fix	h	k	l	d	2θ	I fix	h	k	l
4.58700	22.490	4	2	0	0	1.53914	71.064	58	2	1	3
3.50917	29.535	999	2	1	0	1.52900	71.608	3	6	0	0
3.46186	29.948	782	1	1	1	1.49309	73.609	107	5	0	2
2.89780	35.959	975	2	1	1	1.49309	73.609	107	3	3	1
2.72450	38.333	48	0	2	0	1.47214	74.834	17	6	1	0
2.56900	40.753	3	0	0	2	1.46408	75.317	76	1	3	2
2.47383	42.394	239	1	0	2	1.45920	75.613	104	5	2	1
2.40703	43.630	178	0	2	1	1.44998	76.179	61	0	2	3
2.36693	44.408	78	3	1	1	1.44998	76.179	61	4	2	2
2.34246	44.898	22	2	2	0	1.44001	76.803	80	3	1	3
2.32823	45.187	26	1	2	1	1.44001	76.803	80	5	1	2
2.29350	45.910	44	4	0	0	1.43220	77.299	122	1	2	3
2.25256	46.794	42	1	1	2	1.42389	77.835	5	4	3	0
2.24141	47.040	146	2	0	2	1.41520	78.404	78	6	1	1
2.13140	49.628	150	2	2	1	1.38255	80.629	2	2	2	3
2.11388	50.067	5	4	1	0	1.37218	81.366	2	4	3	1
2.07289	51.128	4	2	1	2	1.36225	82.086	63	0	4	0
1.96701	54.097	195	3	0	2	1.33443	84.182	82	3	3	2
1.95490	54.460	14	4	1	1	1.33443	84.182	82	6	2	0
1.89139	56.449	310	3	2	1	1.31676	85.579	30	0	4	1
1.86911	57.183	3	0	2	2	1.31390	85.810	12	6	0	2
1.85015	57.824	195	3	1	2	1.31016	86.115	24	3	2	3
1.83149	58.470	29	1	2	2	1.31016	86.115	24	5	2	2
1.75458	61.301	35	4	2	0	1.30340	86.671	7	1	4	1
1.73093	62.231	1	2	2	2	1.29063	87.746	4	6	2	1
1.71089	63.043	9	4	0	2	1.28450	88.273	20	0	0	4
1.68876	63.966	219	2	3	0	1.27729	88.902	2	6	1	2
1.68340	64.194	27	1	3	1	1.27209	89.362	9	1	0	4
1.66043	65.191	311	4	2	1	1.26564	89.941	1	2	4	1
1.64710	65.785	56	5	1	1	1.25192	91.203	1	5	3	1
1.63232	66.458	5	4	1	2	1.24539	91.818	1	4	3	2
1.60855	67.570	140	1	1	3	1.23677	92.646	47	2	0	4
1.60432	67.773	17	2	3	1	1.23677	92.646	47	7	1	1
1.59480	68.233	20	3	2	2	1.23474	92.843	20	1	3	3

Table 7.1-6 Powder XRD pattern analysis results for Fe_2O_3 in 5.0 mol% Fe-TiO_2.

Pattern: PDF 04-011-7764 Radiation: 1.78897 Quality: Star (*)

Formula	Fe2O3
Name	Iron Oxide
Name (mineral)	Luogufengite, syn
Name (common)	^-Fe2 O3
Status	Primary
Ambient	Yes

Lattice:	Orthorhombic	**Mol. weight =**	159.69
S.G.:	Pna21 (33)	**Volume [CD] =**	417.25
		Dx =	5.08
		Dm =	
		I/Icor =	2.010

a =	5.07150	**Z =**	8
b =	8.73590		
c =	9.41780		
a/b =	0.58054		
c/b =	1.07806		

ANX: A2X3
LPF Collection Code: 1122025
Sample Preparation: Compound Preparation: heated at 1173 K, heated to 1243 K at a rate of 0.5 K·min-1, held for 30 h, cooled to 343 K, product washed with NaOH for 5 d and water
CRUCIBLE: alumina
Unit Cell Data Source: Powder Diffraction

Radiation:	CuK±1	**Filter:**	Not specified
Wavelength:	1.78897	**d-spacing:**	
SS/FOM:	F(30)= 114.5 (0.0069, 38)		

d	2θ	I fix	h	k	l	d	2θ	I fix	h	k	l
6.40473	16.056	96	0	1	1	1.91852	55.581	10	1	2	4
4.70890	21.900	37	0	0	2	1.91232	55.777	11	2	3	0
4.38599	23.535	26	1	1	0	1.87407	57.018	8	2	3	1
3.97596	26.003	25	1	1	1	1.84543	57.986	22	1	4	2
3.30963	31.360	33	1	2	0	1.84125	58.130	35	0	1	5
3.20236	32.439	239	1	1	2	1.79778	59.676	16	2	2	3
3.20236	32.439	239	0	2	2	1.77179	60.643	3	2	3	2
3.12243	33.294	47	1	2	1	1.73071	62.240	9	1	1	5
2.95431	35.248	369	0	1	3	1.72539	62.453	78	2	0	4
2.78202	37.510	14	0	3	1	1.72208	62.587	47	1	3	4
2.70773	38.579	1000	1	2	2	1.71787	62.758	24	0	5	1
2.55276	41.023	118	1	1	3	1.69269	63.800	10	2	1	4
2.53575	41.311	153	2	0	0	1.69269	63.800	10	1	4	3
2.52529	41.490	61	1	3	0	1.65971	65.223	2	3	1	0
2.44855	42.854	128	2	0	1	1.65481	65.440	10	2	4	0
2.43913	43.027	215	1	3	1	1.63702	66.242	3	1	2	5
2.43913	43.027	215	2	1	0	1.63316	66.419	2	2	3	3
2.35445	44.657	43	0	0	4	1.63316	66.419	2	3	1	1
2.35445	44.657	43	2	1	1	1.62985	66.571	3	2	4	1
2.27764	46.248	59	1	2	3	1.60473	67.753	2	2	2	4
2.23262	47.237	57	2	0	2	1.60118	67.924	4	0	4	4
2.22547	47.398	147	1	3	2	1.58154	68.885	9	0	3	5
2.18397	48.355	40	0	4	0	1.57655	69.134	5	3	2	0
2.16309	48.853	110	2	1	2	1.56963	69.482	7	0	0	6
2.13585	49.517	13	2	2	1	1.56533	69.701	20	3	1	2
2.13585	49.517	13	0	3	3	1.56122	69.911	12	2	4	2
2.07445	51.086	4	1	1	4	1.55491	70.236	16	3	2	1
2.07445	51.086	4	0	2	4	1.52666	71.735	77	1	4	4
2.00589	52.966	35	1	4	0	1.52666	71.735	77	0	5	3
1.98798	53.481	34	2	2	2	1.51206	72.537	83	2	0	5
1.98125	53.677	33	0	4	2	1.50983	72.661	163	1	3	5
1.97261	53.931	48	2	0	3	1.49498	73.500	18	3	2	2
1.96767	54.077	73	1	3	3	1.48990	73.792	4	2	1	5
1.92416	55.404	48	2	1	3	1.48438	74.112	2	2	3	4

7.2 Appendix B: Scanning Electron Microscopy images

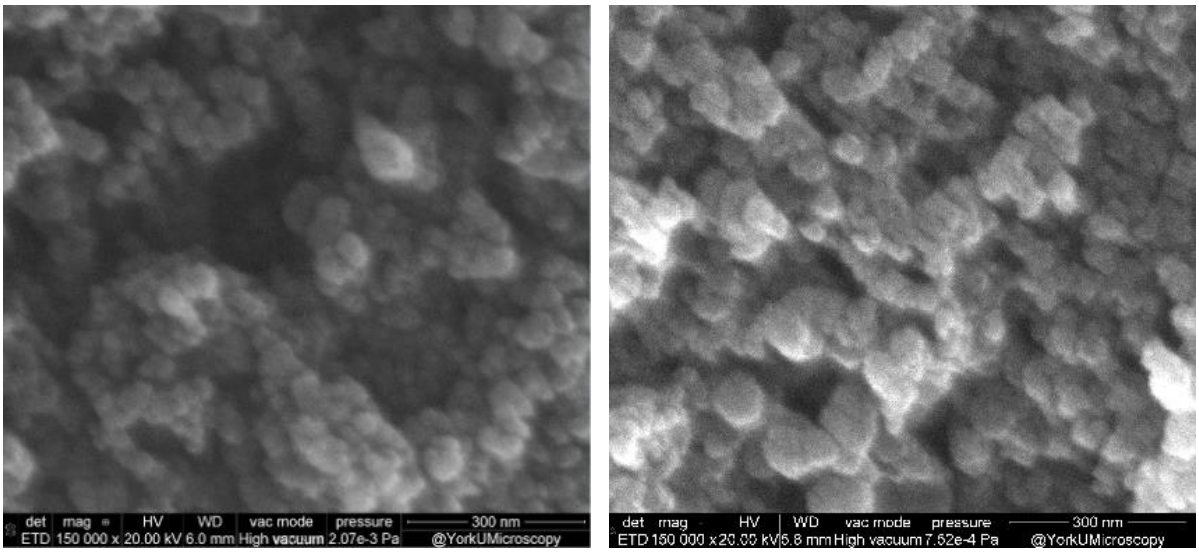

Figure 7.2-1 SEM images captured at 150000 times magnification for left: 0 mol%, and right: 0.5 mol% Fe-TiO_2 with H_2O:EtOH ratio of 69:69, calcinated at 450 °C.

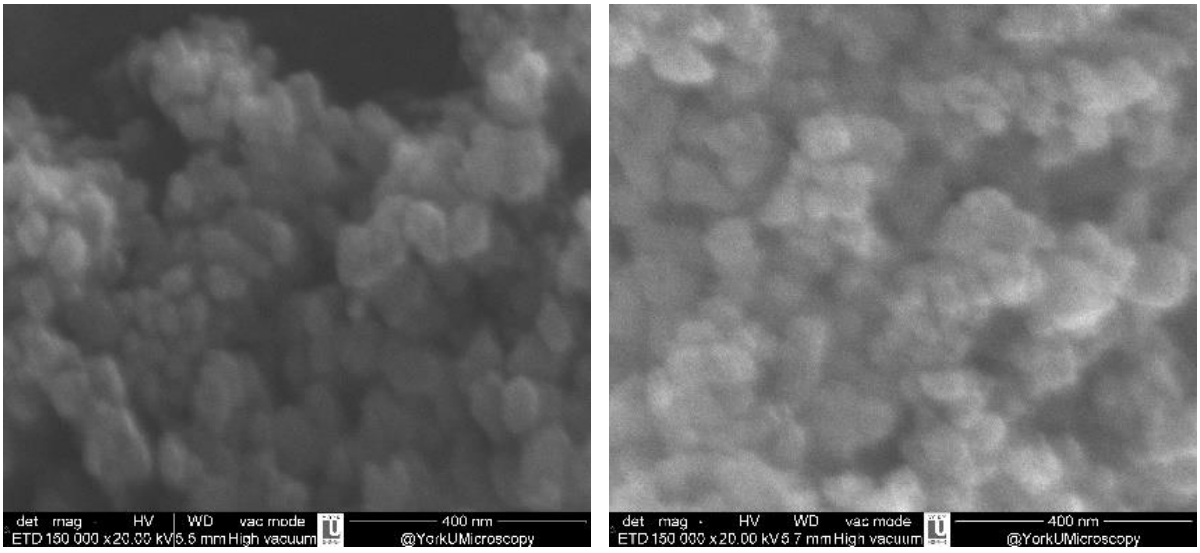

Figure 7.2-2 SEM images captured at 150000 times magnification for left: 0 mol%, and right: 0.5 mol% Fe-TiO_2 with H_2O:EtOH ratio of 138:138, calcinated at 450 °C.

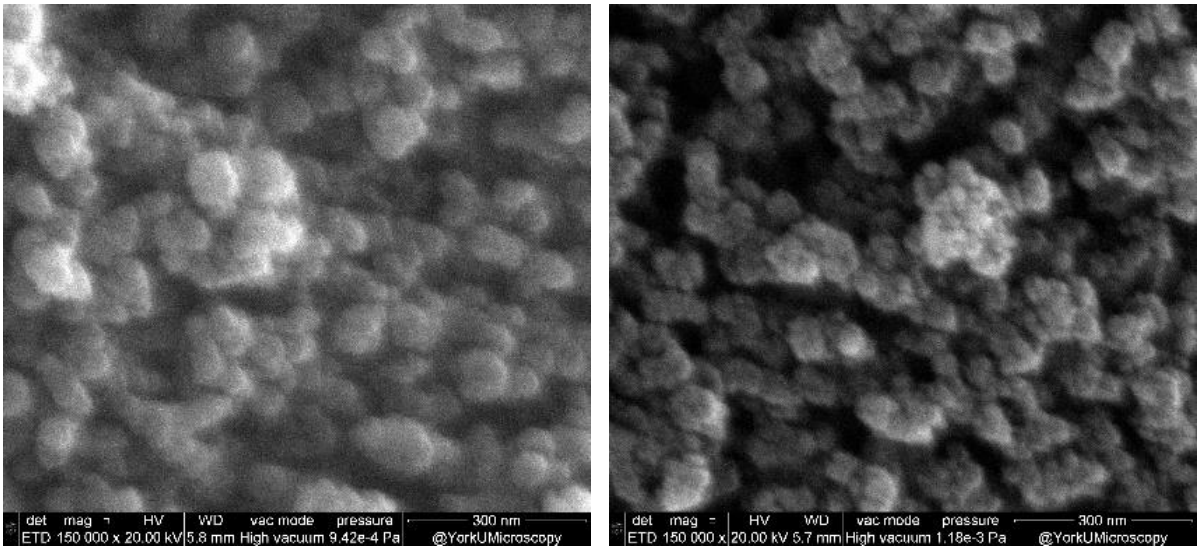

Figure 7.2-3 SEM images captured at 150000 times magnification for left: 0 mol%, and right: 0.5 mol% Fe-TiO_2 with H_2O:EtOH ratio of 138:138, calcinated at 350 °C.

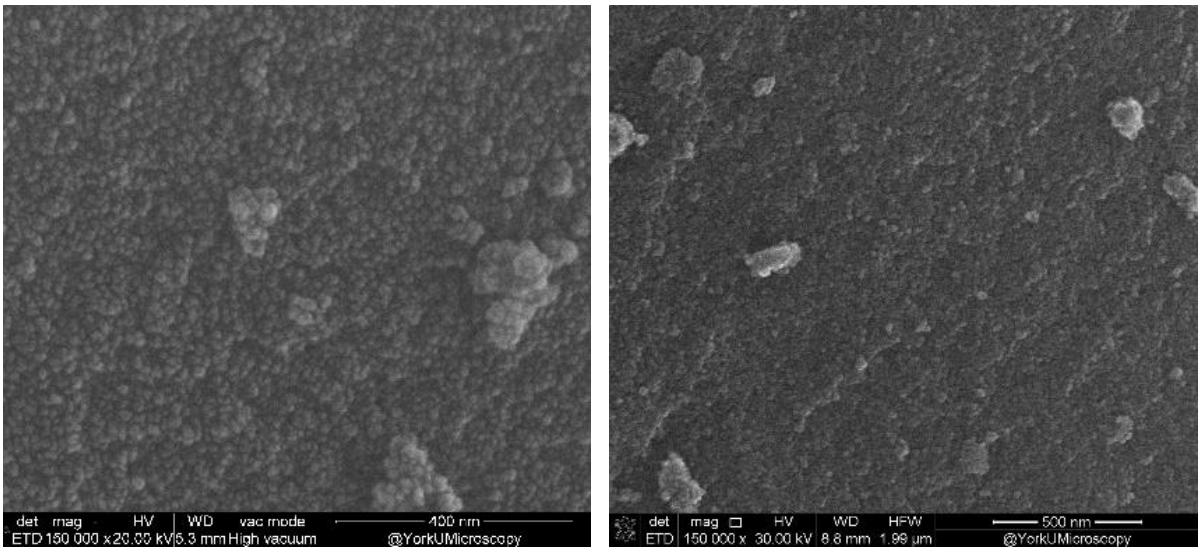

Figure 7.2-4 SEM images captured at 150000 times magnification for left: 2.0 mol%, and right: 5.0 mol% Fe-TiO_2 with H_2O:EtOH ratio of 138:138, calcinated at 450 °C.

7.3 Appendix C: Energy Dispersive X-ray spectra

7.3.1 0 mol% Fe doping

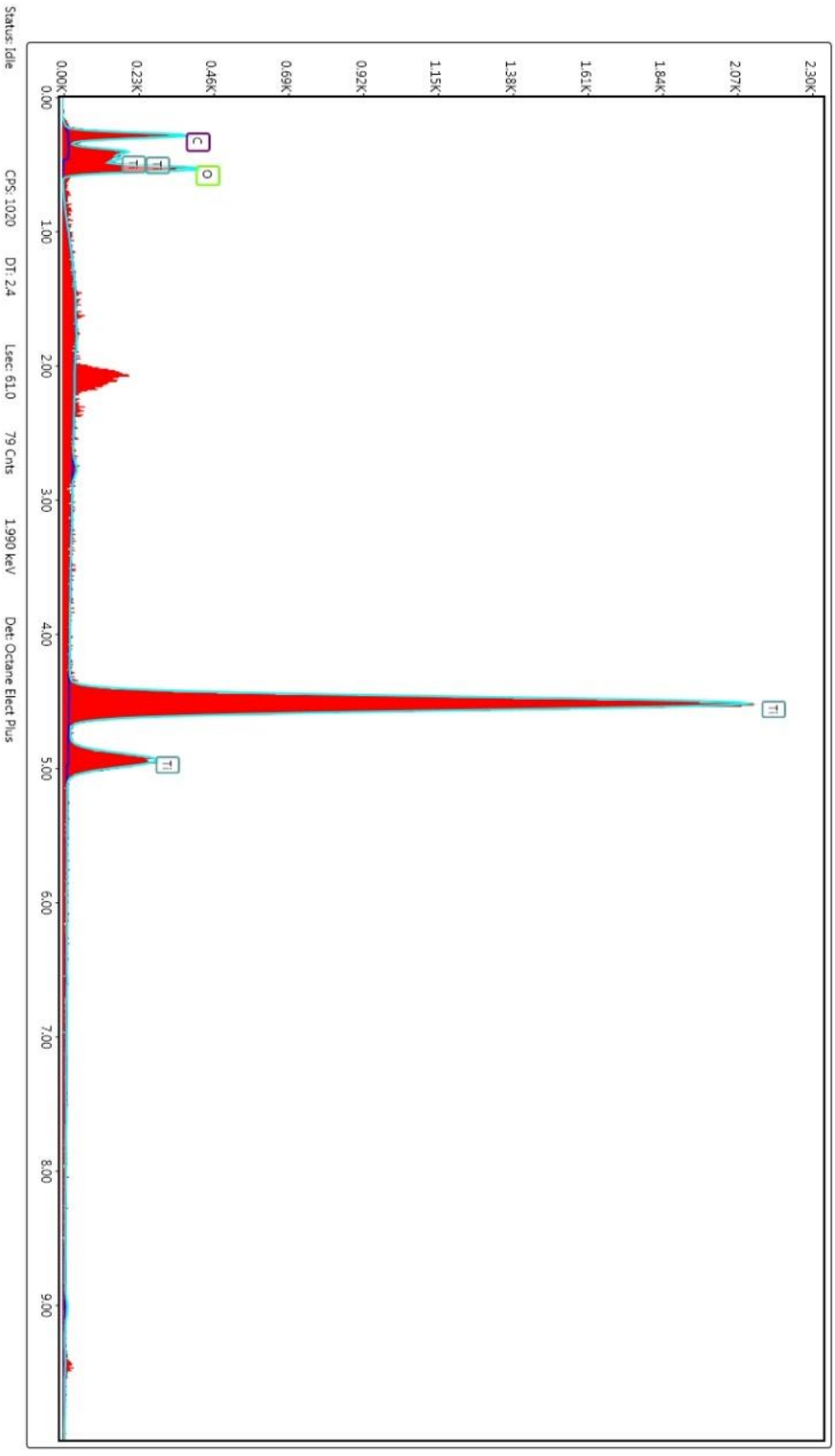

Figure 7.3-1 EDX spectrum of 0 mol% Fe-TiO_2.

7.3.2 0.5 mol% Fe doping

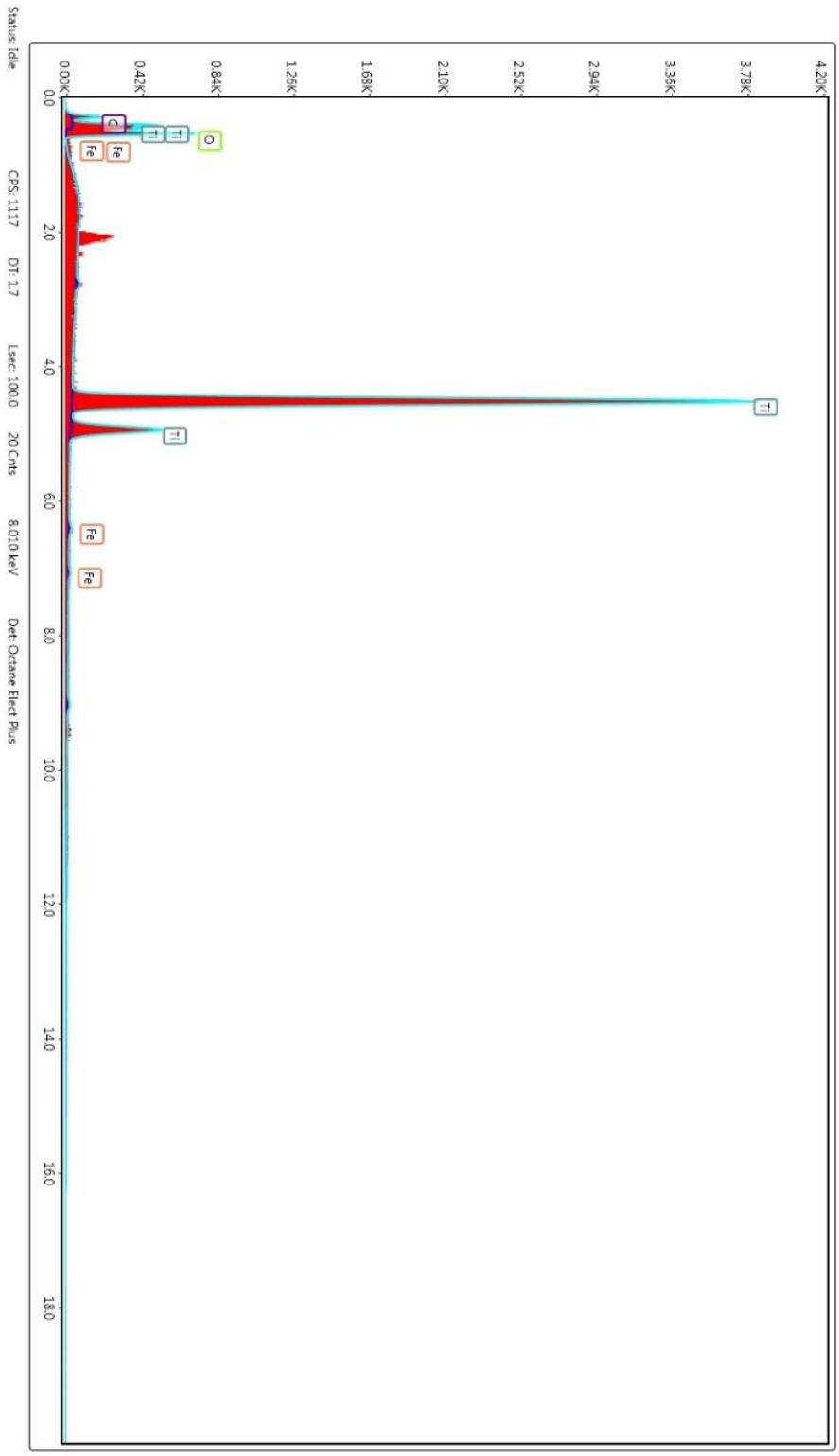

Figure 7.3-2 EDX spectrum of 0.5 mol% Fe-TiO_2.

7.3.3 2.0 mol% Fe doping

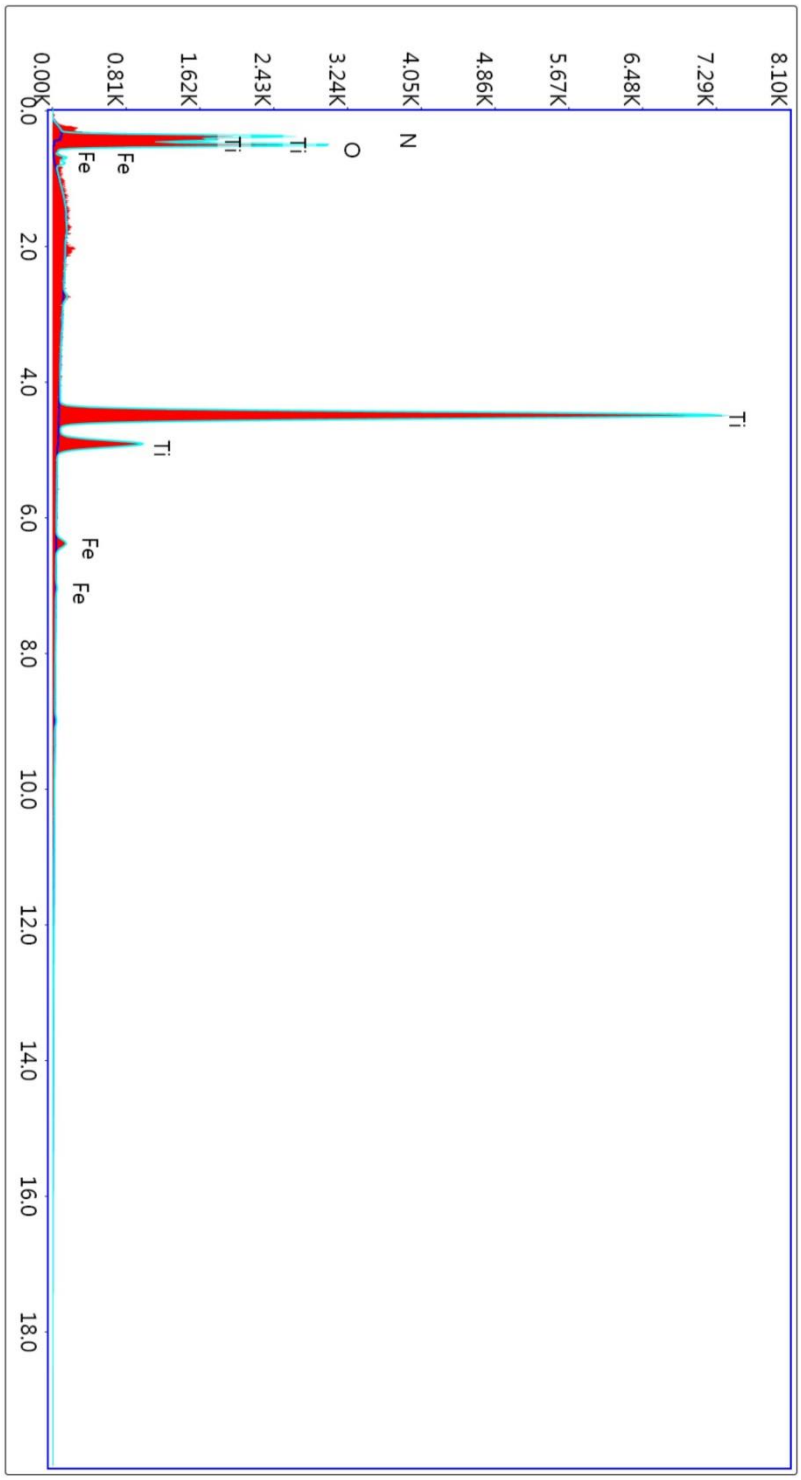

Figure 7.3-3 EDX spectrum of 2.0 mol% Fe-TiO_2.

7.3.4 5.0 mol% Fe doping

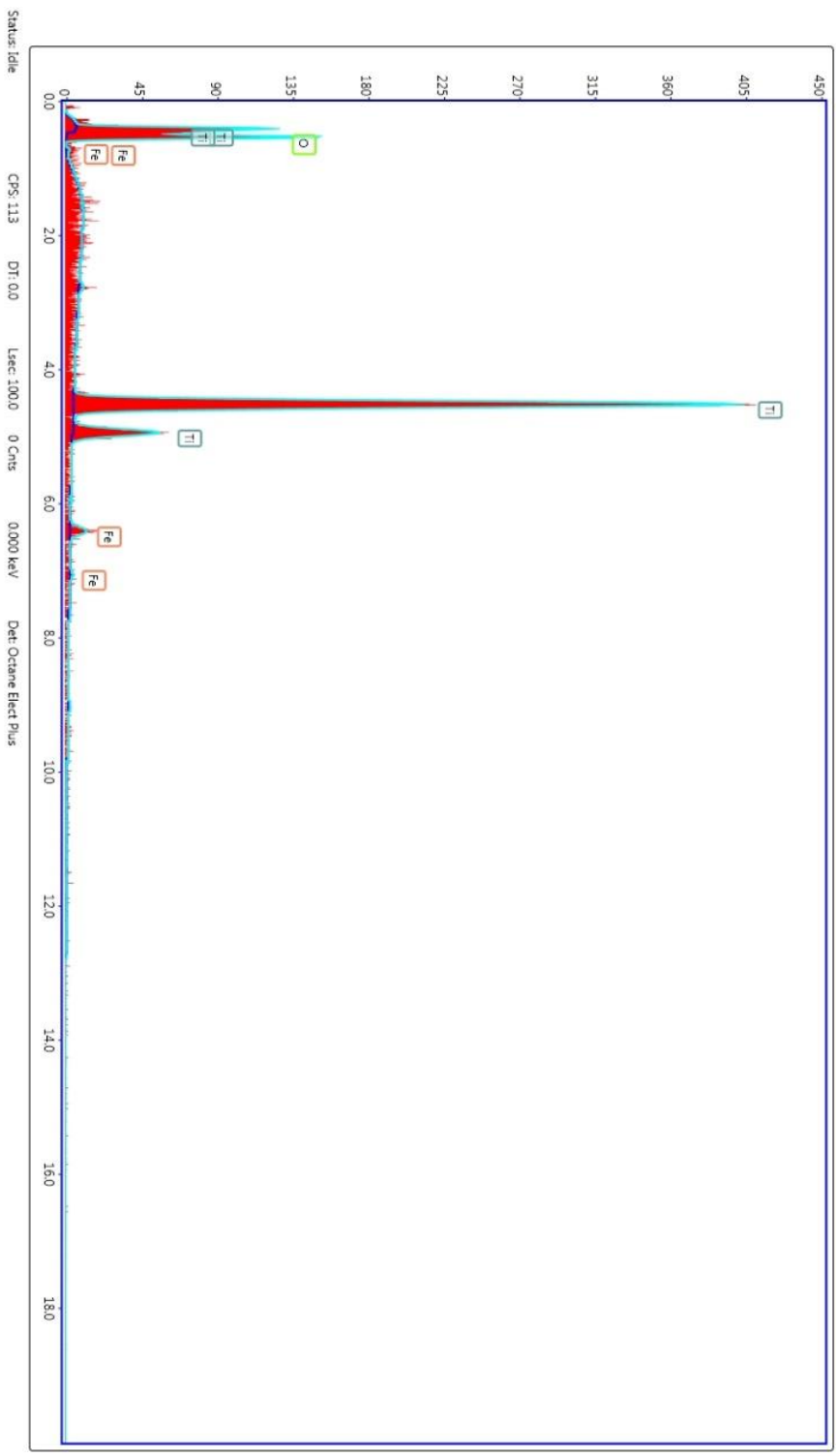

Figure 7.3-4 EDX spectrum of 5.0 mol% Fe-TiO_2.

7.4 Appendix D: Ultraviolet-Visible Diffuse Reflectance Spectroscopy fitting

7.4.1 Direct band gap

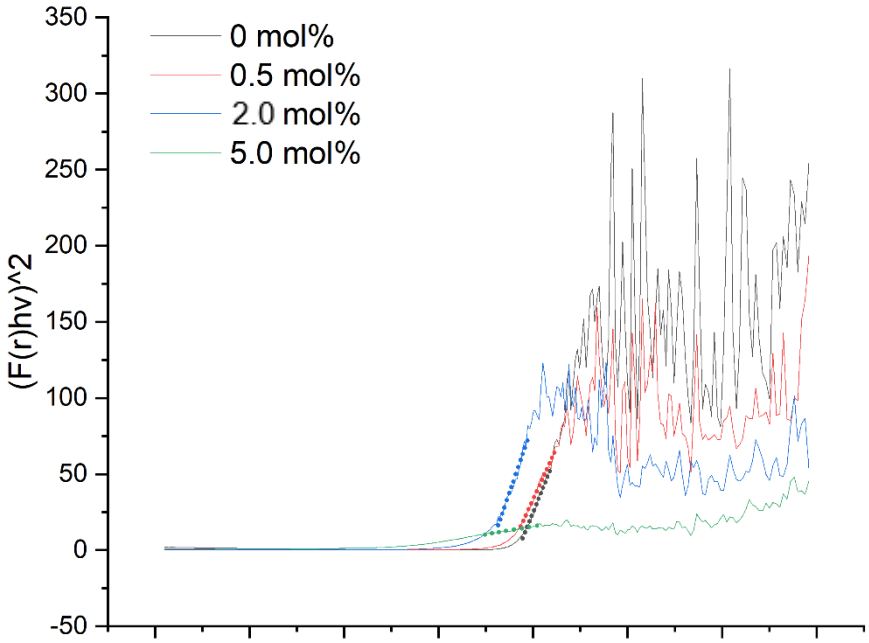

Figure 7.4-1 UV-Vis DRS spectra for direct band Tauc plot of 0 mol% (black), 0.5 mol% (red), 2.0 mol% (blue) and 5.0 mol% (green) Fe-TiO_2. The abscissa is the energy, and the ordinate is the coefficient calculated from Kubelka-Munk function with $n = 2$. Dashed lines are linear fittings for the corresponding spectrum.

Table 7.4-1 Linear fitting and direct band gap results for 0 mol% to 5.0 mol% Fe-TiO_2.

Fe doping (mol%)	0	0.5	2.0	5.0
Slope	0.5117	0.635	2999.868	1.49803
Error	0.01497	0.0222	158.1855	0.02468
Intercept	1.75999	2.16176	10089.77	4.26045
Error	0.0529	0.07812	546.4044	0.07607
Band gap (eV)	3.439496	3.404346	3.363406	2.844035
Error (eV)	0.204005	0.242042	0.359498	0.097635

7.4.2 Indirect band gap

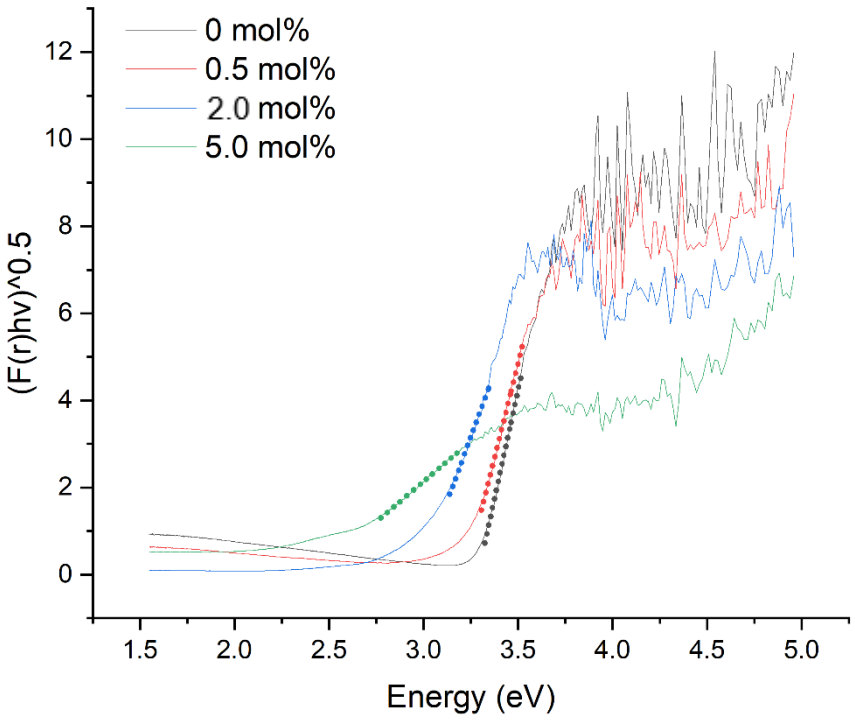

Figure 7.4-2 UV-Vis DRS spectra for indirect band Tauc plot of 0 mol% (black), 0.5 mol% (red), 2.0 mol% (blue) and 5.0 mol% (green) Fe-TiO_2. The abscissa is the energy, and the ordinate is the coefficient calculated from Kubelka-Munk function with $n = 0.5$. Dashed lines are linear fittings for the corresponding spectrum.

Table 7.4-2 Linear fitting and indirect band gap results for 0 mol% to 5.0 mol% Fe-TiO_2

Fe doping (mol%)	0	0.5	2.0	5.0
Slope	10.42987	8.34965	8.21172	4.45422
Error	0.09395	0.1025	0.21072	0.01398
Intercept	33.66839	26.19779	24.50084	9.90601
Error	0.32418	0.35282	0.697	0.04081
Band gap (eV)	3.228074	3.137591	2.983643	2.223961
Error	0.06016	0.080773	0.161442	0.016142

7.4.3 Kubelka-Munk function: from %R spectrum to Tauc plot

After the UV-Vis DRS measurement, the resulting spectrum is a relationship between photon wavelengths and its corresponding reflectance. The conversion of the undoped TiO2 UV-Vis DRS spectrum can be used as an example.

The resulting UV-Vis DRS spectrum consists two columns: %R and wavelength. The reflectance R can be obtained by converting %R into decimals, and the wavelength can be rewritten as the energy using:

$$E = h\nu = \frac{hc}{\lambda} \tag{6}$$

where h is the Planck constant, λ is the wavelength of the light source, ν is the corresponding frequency, and c is the speed of light. Thus, with the help of Equation (3) (section 2.4), conversions can be made as shown in Table 7.4-3 to obtain the resulting Tauc plot. For direct band gap, the bang gap value can be determined by plotting and fitting X1 and Y1 columns, and the indirect using X1 and Y2.

Table 7.4-3 Conversion of UV-Vis DRS data using Kubelka-Munk function.

Raw data			→	Conversion		
	X	Y		X1	Y1	Y2
Name	Wavelength	%Reflectance		Energy	$(F(R)h\nu)^2$	$(F(R)h\nu)^{1/2}$
Units	nm	%		eV		
Data	800	31.38275		1.54975	1.85219	0.92102
	799	31.13364		1.55169	1.89801	0.93259
	798	31.25542		1.55363	1.87895	0.92864
	…	…		…	…	…

7.5 Appendix E: XPS fitting

7.5.1 Valence band XPS

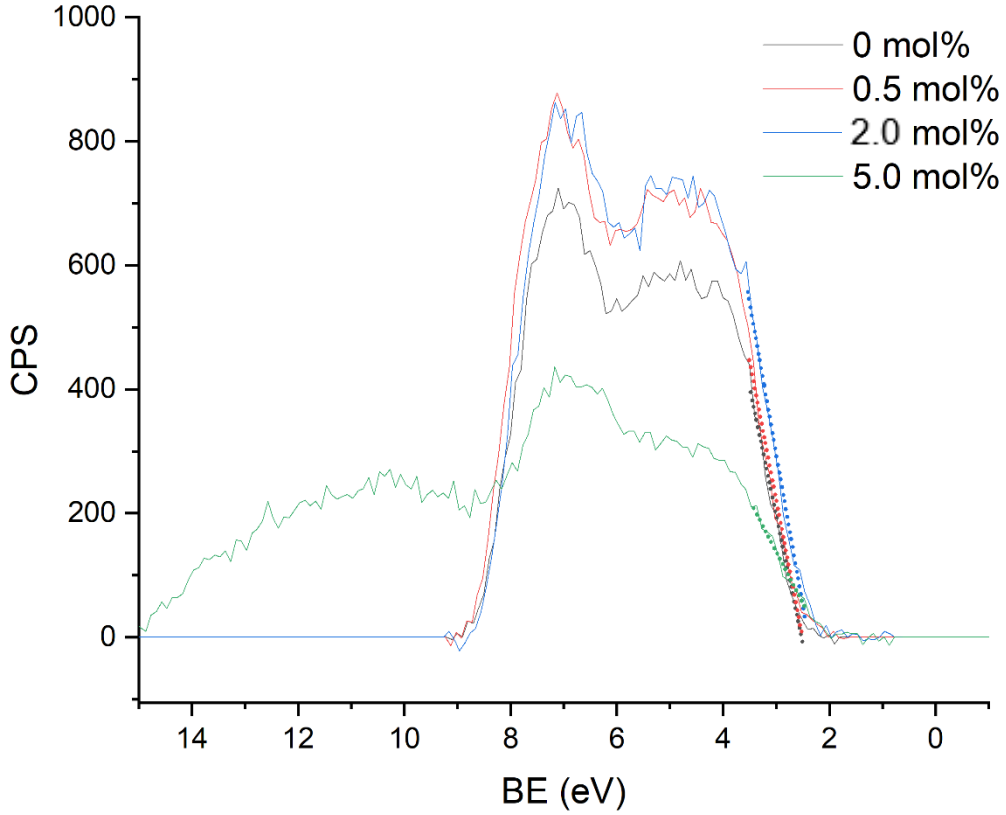

Figure 7.5-1 XPS valence band spectra of 0 mol% (black), 0.5 mol% (red), 2.0 mol% (blue) and 5.0 mol% (green) Fe-TiO_2. The abscissa is the binding energy, and the ordinate is the count of detected electrons per second. Dashed lines are linear fittings for the corresponding spectrum.

Table 7.5-1 Linear fitting and valence band maximum results for 0 mol% to 5.0 mol% Fe-TiO_2.

Fe doping (mol%)	0	0.5	2.0	5.0
Slope	412.2738	447.6637	165.7301	487.2984
Error	21.8309	27.57426	10.16306	20.63337
Intercept	1039.866	1121.348	359.1509	1166.48
Error	65.98409	83.88314	30.35894	62.55659
Valence band maximum (eV)	2.522271	2.504888	2.167083	2.393769
Error (eV)	0.29361	0.341671	0.316075	0.229732

7.5.2 XPS component fitting

Table 7.5-2 XPS component analysis for all high-resolution spectra.

Iron doping percentage (mol%)	0	0.5	2.0	5.0
Ti 2p				
Ti 2p 3/2	457.76 eV	458.62 eV	458.4 eV	458.42 eV
FWHM	1.02	1.05	1.09	1.16
Ti 2p 3/2 satellite	457.84 eV	459.03 eV	459.39 eV	459.65 eV
FWHM	2.07	2.97	3.77	2.93
Ti 2p 1/2	463.46 eV	464.32 eV	464.10 eV	464.18 eV
FWHM	1.88	1.95	2.00	2.32
C 1s				
C-C	284.80 eV	284.80 eV	284.80 eV	284.80 eV
FWHM	1.34	1.33	1.36	1.42
C-O-C	286.07 eV	286.15 eV	286.19 eV	286.22 eV
FWHM	1.62	1.71	1.68	1.60
C-O=C	288.64 eV	288.74 eV	288.48 eV	288.45 eV
FWHM	1.31	1.45	1.40	2.21
O 1s				
Metal oxide	529.01 eV	529.86 eV	529.63 eV	529.69 eV
FWHM	1.13	1.16	1.19	1.24
Metal hydroxide	530.41 eV	531.40 eV	531.29 eV	531.19 eV
FWHM	2.10	1.87	1.96	2.35
Fe 2p				
Fe 2p 3/2	N/A	709.25 eV	709.57 eV	710.46 eV
FWHM		1.96	3.50	3.67
Fe 2p 3/2 satellite		713.25 eV	713.61 eV	714.61 eV
FWHM		6.64	6.74	7.50
Fe 2p 1/2		723.15 eV	722.76 eV	723.69 eV
FWHM		8.89	6.42	5.61
Fe 2p 1/2 satellite		731.76 eV	729.89 eV	729.09 eV
FWHM		8.98	13.02	10.46

Table 7.5-3 XPS detailed component analysis for Fe 2p spectrum of the 5.0 mol% Fe-TiO_2.

Fe(II) 2p 3/2	708.73 eV	FWHM	1.13
Fe(III) 2p 3/2	710.43 eV		2.62
Fe(II) 2p 3/2 satellite	713.04 eV		4.57
Fe(III) 2p 3/2 satellite	718.72 eV		6.93
Fe(II) 2p 1/2	722.64 eV		2.50
Fe(III) 2p 1/2	724.58 eV		3.28
Fe(II) 2p 1/2 satellite	727.87 eV		4.69
Fe(III) 2p 1/2 satellite	732.27 eV		8.71

Table 7.5-4 XPS component analysis for all valence band spectra.

Iron doping percentage (mol%)	0	0.5	2.0	5.0
Valence band				
Ti-O component 1	7.16 eV	7.19 eV	7.17 eV	7.17 eV
FWHM	1.56	1.56	1.48	2.07
Ti-O component 2	5.21 eV	5.25 eV	5.22 eV	5.22 eV
FWHM	2.14	2.14	2.47	2.61
Ti-O component 3	3.81 eV	3.89 eV	3.82 eV	3.82 eV
FWHM	1.27	1.27	1.32	1.41
Fe component	N/A	N/A	3.01 eV	3.01 eV
FWHM			0.64	0.73

7.6 Appendix F: UPS fitting

7.6.1 Work function

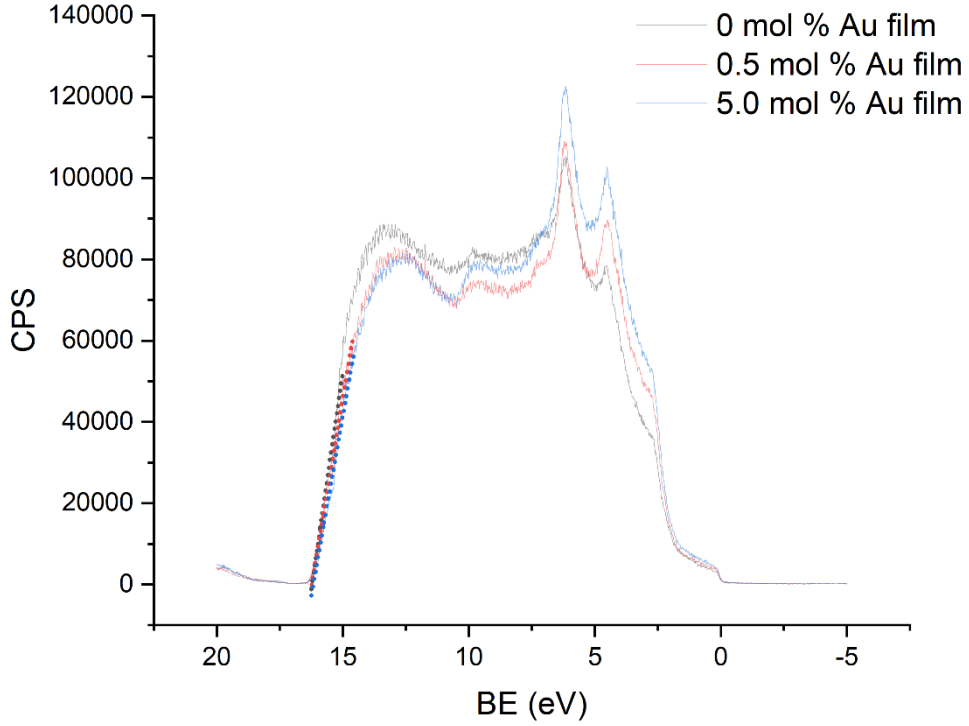

Figure 7.6-1 UPS valence band spectra of the gold film deposited on 0 mol% (black), 0.5 mol% (red), and 5.0 mol% (blue) Fe-TiO_2. The abscissa is the binding energy, and the ordinate is the count of detected electrons per second. Dashed lines are linear fittings for the corresponding spectrum.

Table 7.6-1 Linear fitting, Secondary electron edge cut-off and work function results of the gold film deposited on 0 mol% to 5.0 mol% Fe-TiO_2.

Fe doping (mol%)	0	0.5	5
Slope	-42728.4	-37144.7	-35297.1
Error	878.2292	399.5139	475.8074
Intercept	693060.8	602880.2	570769.5
Error	13748.12	6175.529	7345.508
Secondary electron edge cut-off (eV)	16.22015	16.23059	16.17045
Error (eV)	0.011629	0.008314	0.009874
Work function (eV)	4.999853	4.989415	5.049552

7.6.2 Valence band maximum

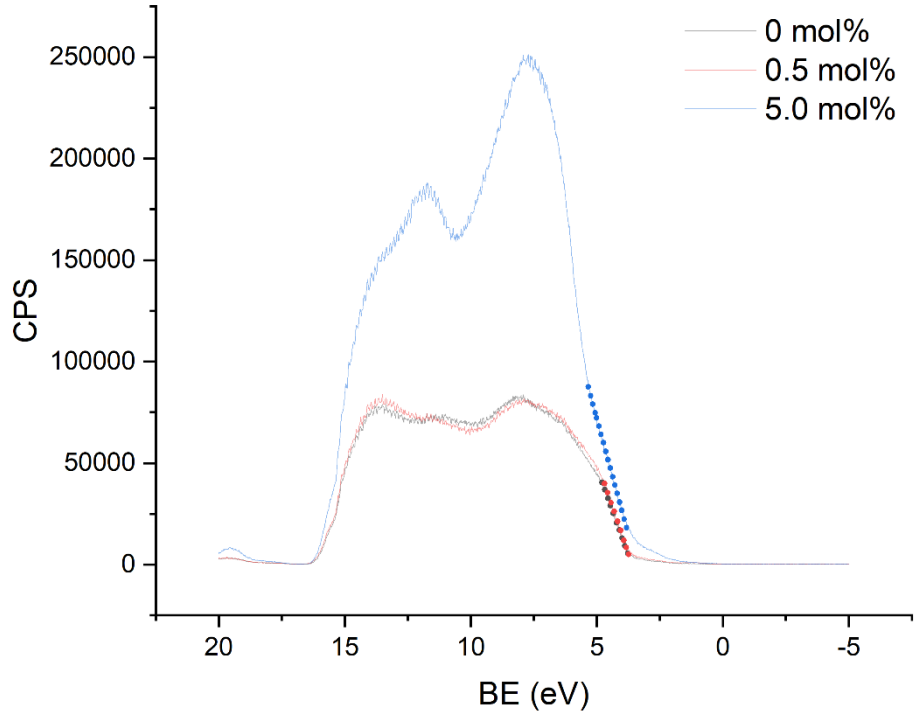

Figure 7.6-2 UPS valence band spectra of 0 mol% (black), 0.5 mol% (red), and 5.0 mol% (blue) Fe-TiO_2. The abscissa is the binding energy, and the ordinate is the count of detected electrons per second. Dashed lines are linear fittings for the corresponding spectrum.

Table 7.6-2 Linear fitting and valence band maximum results of 0 mol% to 5.0 mol% Fe-TiO_2.

Fe doping (mol%)	0	0.5	5.0
Slope	34573.17	36586.87	45594.01
Error	303.6801	480.4119	292.0912
Intercept	125134.1	131735.9	156073
Error	1305.973	2036.867	1353.281
Valence band maximum (eV)	3.619399	3.600633	3.423103
Error (eV)	0.069566	0.102951	0.051611

8 Reference

1. Braun, J. H., Baidins, A. & Marganski, R. E. TiO2 pigment technology: a review. *Prog. Org. Coat.* **20**, 105–138 (1992).
2. Yuan, S., Chen, W. & Hu, S. Fabrication of TiO2 nanoparticles/surfactant polymer complex film on glassy carbon electrode and its application to sensing trace dopamine. *Mater. Sci. Eng. C* **25**, 479–485 (2005).
3. Pfaff, G. & Reynders, P. Angle-Dependent Optical Effects Deriving from Submicron Structures of Films and Pigments. *Chem. Rev.* **99**, 1963–1982 (1999).
4. Salvador, A., Pascual-Martí, M. C., Adell, J. R., Requeni, A. & March, J. G. Analytical methodologies for atomic spectrometric determination of metallic oxides in UV sunscreen creams. *J. Pharm. Biomed. Anal.* **22**, 301–306 (2000).
5. Zallen, R. & Moret, M. P. The optical absorption edge of brookite TiO2. *Solid State Commun.* **137**, 154–157 (2006).
6. Hagfeldt, A. & Graetzel, M. Light-Induced Redox Reactions in Nanocrystalline Systems. *Chem. Rev.* **95**, 49–68 (1995).
7. Fujishima, A. & Honda, K. Electrochemical Photolysis of Water at a Semiconductor Electrode. *Nature* **238**, 37–38 (1972).
8. Grätzel, M. Conversion of sunlight to electric power by nanocrystalline dye-sensitized solar cells. *J. Photochem. Photobiol. Chem.* **164**, 3–14 (2004).
9. Grätzel, M. Dye-Sensitized Solid-State Heterojunction Solar Cells. *MRS Bull.* **30**, 23–27 (2005).
10. Luttrell, T. *et al.* Why is anatase a better photocatalyst than rutile? - Model studies on epitaxial TiO 2 films. *Sci. Rep.* **4**, 4043 (2014).
11. Lei, J. *et al.* Arrayed porous iron-doped TiO2 as photoelectrocatalyst with controllable pore size. *Int. J. Hydrog. Energy* **36**, 8167–8172 (2011).
12. Nazari, M. Iron-Doped Titanium Dioxide Nanomaterials: Synthesis, Characterization and Photodegradation Catalytic Behavior. (2019).
13. Popa, M. *et al.* Fe, Ce and Cu influence on morpho-structural and photocatalytic properties of TiO2 aerogels. *Rev. Roum. Chim.* **55**, 369–375 (2010).
14. Zhang, J., Zhou, P., Liu, J. & Yu, J. New understanding of the difference of photocatalytic activity among anatase, rutile and brookite TiO2. *Phys. Chem. Chem. Phys.* **16**, 20382–20386 (2014).
15. Reyes-Coronado, D. *et al.* Phase-pure TiO(2) nanoparticles: anatase, brookite and rutile. *Nanotechnology* **19**, 145605 (2008).
16. Lin, H. *et al.* Synthesis of High-Quality Brookite TiO $_2$ Single-Crystalline Nanosheets with Specific Facets Exposed: Tuning Catalysts from Inert to Highly Reactive. *J. Am. Chem. Soc.* **134**, 8328–8331 (2012).
17. Scanlon, D. O. *et al.* Band alignment of rutile and anatase TiO 2. *Nat. Mater.* **12**, 798–801 (2013).
18. Linsebigler, A. L., Lu, G. & Yates, J. T. Photocatalysis on TiO2 Surfaces: Principles, Mechanisms, and Selected Results. *Chem. Rev.* **95**, 735–758 (1995).
19. Liu, Z., Wang, Y., Chu, W., Li, Z. & Ge, C. Characteristics of doped TiO2 photocatalysts for the degradation of methylene blue waste water under visible light. *J. Alloys Compd.* **501**, 54–59

(2010).
20. Yang, X., Wang, S., Sun, H., Wang, X. & Lian, J. Preparation and photocatalytic performance of Cu-doped TiO2 nanoparticles. *Trans. Nonferrous Met. Soc. China* **25**, 504–509 (2015).
21. Inturi, S. N. R., Boningari, T., Suidan, M. & Smirniotis, P. G. Visible-light-induced photodegradation of gas phase acetonitrile using aerosol-made transition metal (V, Cr, Fe, Co, Mn, Mo, Ni, Cu, Y, Ce, and Zr) doped TiO2. *Appl. Catal. B Environ.* **144**, 333–342 (2014).
22. Akpan, U. G. & Hameed, B. H. The advancements in sol–gel method of doped-TiO2 photocatalysts. *Appl. Catal. Gen.* **375**, 1–11 (2010).
23. Nolan, N. T. *et al.* Effect of N-doping on the photocatalytic activity of sol–gel TiO2. *J. Hazard. Mater.* **211–212**, 88–94 (2012).
24. Subramanian, M., Vijayalakshmi, S., Venkataraj, S. & Jayavel, R. Effect of cobalt doping on the structural and optical properties of TiO2 films prepared by sol–gel process. *Thin Solid Films* **516**, 3776–3782 (2008).
25. Withers, A. C., Essene, E. J. & Zhang, Y. Rutile/TiO2II phase equilibria. *Contrib. Mineral. Petrol.* **145**, 199–204 (2003).
26. Beltrán, A., Gracia, L. & Andrés, J. Density Functional Theory Study of the Brookite Surfaces and Phase Transitions between Natural Titania Polymorphs. *J. Phys. Chem. B* **110**, 23417–23423 (2006).
27. Ren, R., Yang, Z. & Shaw, L. L. Polymorphic transformation and powder characteristics of TiO2 during high energy milling. *J. Mater. Sci.* **35**, 6015–6026 (2000).
28. Nie, X., Zhuo, S., Maeng, G. & Sohlberg, K. Doping of TiO2 Polymorphs for Altered Optical and Photocatalytic Properties. *Int. J. Photoenergy* **2009**, e294042 (2009).
29. Hanaor, D. A. H., Xu, W., Ferry, M. & Sorrell, C. C. Abnormal grain growth of rutile TiO2 induced by ZrSiO4. *J. Cryst. Growth* **359**, 83–91 (2012).
30. Pauling, L. & Sturdivant, J. H. The crystal structure of brookite. *Z. Für Krist. - Cryst. Mater.* **68**, 239–256 (1928).
31. Kittel, C. *Introduction to Solid State Physics*. (wiley, 2004).
32. Ma, Y. & Yao, J. Photodegradation of Rhodamine B catalyzed by TiO2 thin films. *J. Photochem. Photobiol. Chem.* **116**, 167–170 (1998).
33. Kim, D.-H., Kim, W.-S., Kim, S. & Hong, S.-H. Brookite TiO2 Thin Film Epitaxially Grown on (110) YSZ Substrate by Atomic Layer Deposition. *ACS Appl. Mater. Interfaces* **6**, 11817–11822 (2014).
34. Pierre, A. C. & Pajonk, G. M. Chemistry of Aerogels and Their Applications. *Chem. Rev.* **102**, 4243–4266 (2002).
35. Lu, Z., Lindner, E. & Mayer, H. A. Applications of Sol−Gel-Processed Interphase Catalysts. *Chem. Rev.* **102**, 3543–3578 (2002).
36. Yakovlev, A. V., Milichko, V. A., Vinogradov, V. V. & Vinogradov, A. V. Inkjet Color Printing by Interference Nanostructures. *ACS Nano* **10**, 3078–3086 (2016).
37. Dabbs, D. M. & Aksay, I. A. Self-Assembled Ceramics Produced by Complex-Fluid Templation. *Annu. Rev. Phys. Chem.* **51**, 601–622 (2000).
38. Sakka, S. & Kamiya, K. The sol-gel transition in the hydrolysis of metal alkoxides in relation to the formation of glass fibers and films. *J. Non-Cryst. Solids* **48**, 31–46 (1982).
39. Van Blaaderen, A., Van Geest, J. & Vrij, A. Monodisperse colloidal silica spheres from tetraalkoxysilanes: Particle formation and growth mechanism. *J. Colloid Interface Sci.* **154**,

481–501 (1992).

40. Bessekhouad, Y., Robert, D. & Weber, J. Synthesis of photocatalytic TiO2 nanoparticles: Optimization of the preparation conditions. *J. Photochem. Photobiol. Chem.* **157**, 47–53 (2003).
41. Oskam, G., Nellore, A., Penn, R. L. & Searson, P. C. The Growth Kinetics of TiO2 Nanoparticles from Titanium(IV) Alkoxide at High Water/Titanium Ratio. *J. Phys. Chem. B* **107**, 1734–1738 (2003).
42. Sugimoto, T. Preparation of monodispersed colloidal particles. *Adv. Colloid Interface Sci.* **28**, 65–108 (1987).
43. Schubert, U. Chemical modification of titanium alkoxides for sol–gel processing. *J. Mater. Chem.* **15**, 3701 (2005).
44. Periyat, P., Baiju, K. V., Mukundan, P., Pillai, P. K. & Warrier, K. G. K. Aqueous colloidal sol–gel route to synthesize nanosized ceria-doped titania having high surface area and increased anatase phase stability. *J. Sol-Gel Sci. Technol.* **43**, 299–304 (2007).
45. Baiju, K. V. *et al.* Enhanced photoactivity of neodymium doped mesoporous titania synthesized through aqueous sol–gel method. *J. Sol-Gel Sci. Technol.* **43**, 283–290 (2007).
46. Seifried, S., Winterer, M. & Hahn, H. Nanocrystalline Titania Films and Particles by Chemical Vapor Synthesis. *Chem. Vap. Depos.* **6**, 239–244 (2000).
47. Arami, H., Mazloumi, M., Khalifehzadeh, R. & Sadrnezhaad, S. K. Sonochemical preparation of TiO2 nanoparticles. *Mater. Lett.* **61**, 4559–4561 (2007).
48. Gomathi Thanga Keerthana, B., Solaiyammal, T., Muniyappan, S. & Murugakoothan, P. Hydrothermal synthesis and characterization of TiO2 nanostructures prepared using different solvents. *Mater. Lett.* **220**, 20–23 (2018).
49. Li, Z., Shen, W., He, W. & Zu, X. Effect of Fe-doped TiO2 nanoparticle derived from modified hydrothermal process on the photocatalytic degradation performance on methylene blue. *J. Hazard. Mater.* **155**, 590–594 (2008).
50. Wojtaszek, K. *et al.* The influence of nitrogen doping on the electronic structure of the valence and conduction band in TiO_2. *J. Synchrotron Radiat.* **26**, 145–151 (2019).
51. Park, J. H., Kim, S. & Bard, A. J. Novel Carbon-Doped TiO_2 Nanotube Arrays with High Aspect Ratios for Efficient Solar Water Splitting. *Nano Lett.* **6**, 24–28 (2006).
52. Mor, G. K., Varghese, O. K., Paulose, M., Shankar, K. & Grimes, C. A. A review on highly ordered, vertically oriented TiO2 nanotube arrays: Fabrication, material properties, and solar energy applications. *Sol. Energy Mater. Sol. Cells* **90**, 2011–2075 (2006).
53. George, S. *et al.* Role of Fe Doping in Tuning the Band Gap of TiO2 for the Photo-Oxidation-Induced Cytotoxicity Paradigm. *ACS Publications* https://pubs.acs.org/doi/pdf/10.1021/ja202836s (2011) doi:10.1021/ja202836s.
54. Shi, J. *et al.* Hydrothermal synthesis of graphene wrapped Fe-doped TiO2 nanospheres with high photocatalysis performance. *Ceram. Int.* **44**, 7473–7480 (2018).
55. Schneider, J. *et al.* Understanding TiO2 Photocatalysis: Mechanisms and Materials. *Chem. Rev.* **114**, 9919–9986 (2014).
56. Sunil Paul, M. M., Aravind, U. K., Pramod, G. & Aravindakumar, C. T. Oxidative degradation of fensulfothion by hydroxyl radical in aqueous medium. *Chemosphere* **91**, 295–301 (2013).
57. Spadaro, J. T., Isabelle, Lorne. & Renganathan, V. Hydroxyl radical mediated degradation of azo dyes: evidence for benzene generation. *Environ. Sci. Technol.* **28**, 1389–1393 (1994).

58. Ajmal, A., Majeed, I., Malik, R. N., Idriss, H. & Nadeem, M. A. Principles and mechanisms of photocatalytic dye degradation on TiO2 based photocatalysts: a comparative overview. *RSC Adv.* **4**, 37003–37026 (2014).
59. Galindo, C., Jacques, P. & Kalt, A. Photodegradation of the aminoazobenzene acid orange 52 by three advanced oxidation processes: UV/H2O2, UV/TiO2 and VIS/TiO2: Comparative mechanistic and kinetic investigations. *J. Photochem. Photobiol. Chem.* **130**, 35–47 (2000).
60. Chen, F., Xie, Y., Zhao, J. & Lu, G. Photocatalytic degradation of dyes on a magnetically separated photocatalyst under visible and UV irradiation. *Chemosphere* **44**, 1159–1168 (2001).
61. Zhibo Zhang, †, Chen-Chi Wang, ‡, Rama Zakaria, ‡ and & Jackie Y. Ying*, ‡. Role of Particle Size in Nanocrystalline TiO2-Based Photocatalysts. *ACS Publications* https://pubs.acs.org/doi/pdf/10.1021/jp982948%2B (1998) doi:10.1021/jp982948+.
62. Mi, J.-L. *et al.* Highly controlled crystallite size and crystallinity of pure and iron-doped anatase-TiO $_2$ nanocrystals by continuous flow supercritical synthesis. *J. Mater. Res.* **28**, 333–339 (2013).
63. Li, B., Wang, X., Yan, M. & Li, L. Preparation and Characterization of Nano-TiO 2 Powder. *Key Eng. Mater. - KEY ENG MAT* **224–226**, 577–580 (2002).
64. Choi, W., Termin, A. & Hoffmann, M. R. The Role of Metal Ion Dopants in Quantum-Sized TiO $_2$: Correlation between Photoreactivity and Charge Carrier Recombination Dynamics. *J. Phys. Chem.* **98**, 13669–13679 (1994).
65. Haber, F. & Weiss, J. Über die Katalyse des Hydroperoxydes. *Naturwissenschaften* **20**, 948–950 (1932).
66. Ramin Gul, S., Khan, M., Yi, Z. & Wu, B. DFT Insights into the Role of Relative Positions of Fe and N Dopants on the Structure and Properties of TiO2. *Materials* **11**, 313 (2018).
67. Maheu, C., Cardenas, L., Puzenat, E., Afanasiev, P. & Geantet, C. UPS and UV spectroscopies combined to position the energy levels of TiO2 anatase and rutile nanopowders. *Phys. Chem. Chem. Phys.* **20**, 25629–25637 (2018).
68. Bapna, K., Phase, D. M. & Choudhary, R. J. Study of valence band structure of Fe doped anatase TiO $_2$ thin films. *J. Appl. Phys.* **110**, 043910 (2011).
69. Feng, N. *et al.* Unravelling the Efficient Photocatalytic Activity of Boron-induced Ti3+ Species in the Surface Layer of TiO2. *Sci. Rep.* **6**, 34765 (2016).
70. Chen, X. & Burda, C. The Electronic Origin of the Visible-Light Absorption Properties of C-, N- and S-Doped TiO2 Nanomaterials. *J. Am. Chem. Soc.* **130**, 5018–5019 (2008).
71. Hart, M. X-ray diffraction by L. V. Azaroff, R. Kaplow, N. Kato, R. J. Weiss, A. J. C. Wilson and R. A. Young. *Acta Crystallogr. A* **31**, 878–878 (1975).
72. Kennedy, J. F. & Thorley, M. Crystal Structure Determination, William Clegg, Oxford University Press, Oxford, 1998, 84 pp., ISBN 0-19-855-901-1. *Bioseparation* **8**, 339–339 (1999).
73. Patterson, A. L. The Scherrer Formula for X-Ray Particle Size Determination. *Phys. Rev.* **56**, 978–982 (1939).
74. Cheary, R. W. & Coelho, A. A fundamental parameters approach to X-ray line-profile fitting. *J. Appl. Crystallogr.* **25**, 109–121 (1992).
75. Rietveld, H. M. A profile refinement method for nuclear and magnetic structures. *J. Appl. Crystallogr.* **2**, 65–71 (1969).
76. Cheney, B. Introduction to Scanning Electron Microscopy. 13.

77. Wells, O. C. Scanning Electron Microscopy. in *Encyclopedia of Materials: Science and Technology* (eds. Buschow, K. H. J. et al.) 8265–8269 (Elsevier, 2001). doi:10.1016/B0-08-043152-6/01479-0.
78. Urone, P. P. & Hinrichs, R. Limits of Resolution: The Rayleigh Criterion. (2012).
79. Goldstein, J. *et al. Scanning Electron Microscopy and X-Ray Microanalysis: Third Edition*. (Springer US, 2003).
80. Shirley, D. A. High-Resolution X-Ray Photoemission Spectrum of the Valence Bands of Gold. *Phys. Rev. B* **5**, 4709–4714 (1972).
81. Tougaard, S. Practical algorithm for background subtraction. *Surf. Sci.* **216**, 343–360 (1989).
82. Kubelka, P. & Munk, F. Ein Beitrag zur Optik der Farbanstriche. *Z Techn Phys.* **12**, 593–601 (1931).
83. Kubelka, P. New Contributions to the Optics of Intensely Light-Scattering Materials. Part I. *JOSA* **38**, 448–457 (1948).
84. Hecht, H. G. The Interpretation of Diffuse Reflectance Spectra. *J. Res. Natl. Bur. Stand. Sect. Phys. Chem.* **80A**, 567–583 (1976).
85. López, R. & Gómez, R. Band-gap energy estimation from diffuse reflectance measurements on sol–gel and commercial TiO<Subscript>2</Subscript>: a comparative study. *J. Sol-Gel Sci. Technol.* **61**, 1–7 (2011).
86. Cornil, J. *et al.* Valence Electronic Structure of π-Conjugated Materials: Simulation of the Ultraviolet Photoelectron Spectra with Semiempirical Hartree−Fock Approaches. *Chem. Mater.* **11**, 2436–2443 (1999).
87. Kern. in *Handbook of Semiconductor Cleaning Technology* (1993).
88. Hariri, M. Designing Nanostructured Titanium Dioxide-Based Potentiometric Sensors for the Analysis of Chromium(III) and Iron(III) Ions. 193.
89. Joshi, M. & Bhattacharyya, A. Characterization techniques for nanotechnology applications in textiles. *Indian J. Fibre Text. Res.* **33**, 304–317 (2008).
90. Ong, J. L., Lucas, L. C., Raikar, G. n., Connatser, R. & Gregory, J. C. Spectroscopic characterization of passivated titanium in a physiologic solution. *J. Mater. Sci. Mater. Med.* **6**, 113–119 (1995).
91. Aas, N., Pringle, T. J. & Bowker, M. Adsorption and decomposition of methanol on TiO2, SrTiO3 and SrO. *J. Chem. Soc. Faraday Trans.* **90**, 1015–1022 (1994).
92. Yamashita, T. & Hayes, P. Analysis of XPS spectra of Fe2+ and Fe3+ ions in oxide materials. *Appl. Surf. Sci.* **254**, 2441–2449 (2008).
93. Grosvenor, A. P., Kobe, B. A., Biesinger, M. C. & McIntyre, N. S. Investigation of multiplet splitting of Fe 2p XPS spectra and bonding in iron compounds. *Surf Interface Anal* 11 (2004).
94. Ismail, M. A., Hedhili, M. N., Anjum, D. H., Singaravelu, V. & Chung, S. H. Synthesis and Characterization of Iron-Doped TiO2 Nanoparticles Using Ferrocene from Flame Spray Pyrolysis. *Catalysts* **11**, 438 (2021).
95. Wetchakun, N., Incessungvorn, B., Wetchakun, K. & Phanichphant, S. Influence of calcination temperature on anatase to rutile phase transformation in TiO2 nanoparticles synthesized by the modified sol–gel method. *Mater. Lett.* **82**, 195–198 (2012).
96. Popa, M. *et al.* Synthesis, structural characterization, and photocatalytic properties of iron-doped TiO2 aerogels. *J. Mater. Sci.* **44**, 358–364 (2009).
97. Meng, X. *et al.* Anatase-assisted growth of nanoscale crystalline brookite film and rutile rods

on SiO2/Si substrate in a single hydrothermal process. *CrystEngComm* **13**, 3983 (2011).
98. Fàbrega, C., Andreu, T., Cabot, A. & Morante, J. R. Location and catalytic role of iron species in TiO2:Fe photocatalysts: An EPR study. *J. Photochem. Photobiol. Chem.* **211**, 170–175 (2010).
99. Mogal, S. I. *et al.* Single-Step Synthesis of Silver-Doped Titanium Dioxide: Influence of Silver on Structural, Textural, and Photocatalytic Properties. *Ind. Eng. Chem. Res.* **53**, 5749–5758 (2014).
100. Christoforidis, K. C. *et al.* Structure and activity of iron-doped TiO $_2$ -anatase nanomaterials for gas-phase toluene photo-oxidation. *Catal Sci Technol* **3**, 626–634 (2013).
101. Ganesh, I. *et al.* Preparation and characterization of Fe-doped TiO2 powders for solar light response and photocatalytic applications. *Process. Appl. Ceram.* **6**, 21–36 (2012).
102. Delekar, S. D., Yadav, H. M., Achary, S. N., Meena, S. S. & Pawar, S. H. Structural refinement and photocatalytic activity of Fe-doped anatase TiO2 nanoparticles. *Appl. Surf. Sci.* **263**, 536–545 (2012).
103. Göpel, W. *et al.* Surface defects of TiO2(110): A combined XPS, XAES AND ELS study. *Surf. Sci.* **139**, 333–346 (1984).
104. Eastman, D. E. Photoelectric Work Functions of Transition, Rare-Earth, and Noble Metals. *Phys. Rev. B* **2**, 1–2 (1970).
105. Mallick, P. & Dash, P. N. Iron Oxide, Nanoparticle, Annealing, Microstructure, Band Gap. *Nanosci. Nanotechnol.* 5 (2013).
106. Muhamad Iqbal, R. *et al.* The Structural and Optical Band Gap Energy Evaluation of TiO 2 -Fe 2 O 3 Composite. *IOP Conf. Ser. Mater. Sci. Eng.* **833**, 012072 (2020).
107. Mei, Q. *et al.* TiO2 /Fe2O3 heterostructures with enhanced photocatalytic reduction of Cr under visible light irradiation. *RSC Adv.* **9**, 22764–22771 (2019).
108. Shockley, W. & Read, W. T. Statistics of the Recombinations of Holes and Electrons. *Phys. Rev.* **87**, 835–842 (1952).
109. Hall, R. N. Electron-Hole Recombination in Germanium. *Phys. Rev.* **87**, 387–387 (1952).